DIAL
Digital access to libraries

"Hierarchical hybrid materials combining wideband electromagnetic absorption and mechanical performance"

Bollen, Pierre

Abstract

Electromagnetic (EM) interferences are ubiquitous in modern technologies and impact on the reliability of electronic devices and on living cells. Shielding by EM absorption, which is preferable over reflection in certain instances, is attained by simultaneously minimizing the reflection and transmission. This requires, in the gigahertz range, to combine a low dielectric constant, ideally equal to 1, with an electrical conductivity around 1 S/m which are antagonist properties in the world of materials. For some transport application, the need of EM shielding goes along with mechanical shielding while bearing in mind to be as lightweight as possible. In this thesis, a multimaterial and multiscale approach is proposed towards a multifunctional sandwich with optimized mechanical and EM absorption performances. The strategy starts at the nanoscale, using a carbon nanotube reinforced polymer. The conductivity of a polymer can be increased to the range of 1 S/m with a low amount of fillers ...

Document type : *Thèse (Dissertation)*

Référence bibliographique

Bollen, Pierre. *Hierarchical hybrid materials combining wideband electromagnetic absorption and mechanical performance.* Prom. : Huynen, Isabelle ; Pardoen, Thomas ; Bailly, Chistrian

Available at:
http://hdl.handle.net/2078.1/157883

[Downloaded 2019/04/19 at 06:25:30]

Université catholique de Louvain
Institute of Mechanics, Materials and Civil Engineering
Institute of Information and Communication Technologies,
Electronics and Applied Mathematics
Institute of Condensed Matter and Nanosciences

Hierarchical hybrid materials combining wideband electromagnetic absorption and mechanical performance

---

Thèse présentée le 09/03/2015
par Pierre Bollen
en vue de l'obtention du grade de
Docteur en Sciences de l'Ingénieur

Composition du jury

Prof. Isabelle Huynen (Promoteur)	Université catholique de Louvain, Belgique
Prof. Thomas Pardoen (Promoteur)	Université catholique de Louvain, Belgique
Prof. Christian Bailly (Promoteur)	Université catholique de Louvain, Belgique
Prof. Yves Bréchet	Université de Grenoble, France
Prof. André de Lustrac	Université Paris Sud, France
Prof. Bruno Dehez	Université catholique de Louvain, Belgique
Prof. Jean-Pierre Raskin (Président)	Université catholique de Louvain, Belgique

Louvain-la-Neuve, March 9, 2015

Abstract

Electromagnetic (EM) interferences are ubiquitous in modern technologies and impact on the reliability of electronic devices and on living cells. Shielding by EM absorption, which is preferable over reflection in certain instances, is attained by simultaneously minimizing the reflection and transmission. This requires combining a low dielectric constant, ideally equal to 1, with an electrical conductivity around $1\,\mathrm{S{\cdot}m^{-1}}$ in the gigahertz range which are antagonist properties in the world of homogeneous materials. For some transport applications, the need of EM shielding goes along with mechanical shielding while bearing in mind to be as lightweight as possible. Traditionally, a functional structure is made of two materials. One assures the mechanical integrity and the other one provides the functionality. One way to improve the global performances and reduces the weight of a structure, is, if the application allows it, to combine several functionalities into a single material.

A sandwich panel based on a multiscale architectured material is developed for structural and EM absorption performances. At the nanoscale level, carbon nanotubes are dispersed in a polymer to obtain a conductive material. This composite is then foamed into a micro porous solid to improve EM absorption and to decrease the density. The foam is inserted in a millimeter scale hexagonal metallic honeycomb lattice. The combination of the metallic honeycomb and the polymeric foam provides improved bending, impact and crushing performances and a moderate thermal conductivity. This hybrid is used as core for sandwich panels, produced by the addition of two EM transparent face sheets made of glass fiber reinforced polymer.

Our results show that a careful design of the face sheets preserves and

even improves the absorption performances of the hybrid in a dedicated frequency range. The sandwich also offers high bending stiffness versus density performance. Compared to a foam core, the hybrid core reduces the transverse shear deflection thanks to the honeycomb. An experimental level of EM absorption around 95% is achieved in the 10-40 GHz frequency band with a 9 mm thick sandwich panel.

Remerciements

Ça y est la partie sérieuse est terminée. Il est temps de remercier toutes les personnes qui ont contribué de près ou de loin à la réalisation de cette thèse. Ce chapitre, bien moins sérieux et rigoureux que le reste de ce manuscrit, n'en reste pas moins sincère.

En premier lieu, je remercie mes promoteurs, les professeurs Isabelle Huynen, Thomas Pardoen et Christian Bailly pour leur soutien et leur confiance. Ils ont toujours été une lumière dans les heures sombres et ont su dissiper les moments de doutes inhérents au doctorat. Pour certains doctorants, la collaboration avec un promoteur est parfois délicate. Dans mon cas, la collaboration avec trois promoteurs a toujours été conviviale et positive. La seule complication a été de réunir les trois signatures sur les documents administratifs. J'adresse un remerciement tout particulier à Isabelle Huynen qui a su, toujours avec beaucoup de patience, m'expliquer et me réexpliquer l' électromagnétisme.

Mes remerciements vont également aux professeurs Yves Bréchet et André de Lustrac pour m'avoir accompagné tout au long de la thèse, aux membres de mon jury les professeurs Bruno Dehez et Jean-Pierre Raskin ainsi que le professeur Christophe Detrembleur et Jean-Michel Thomassin du CERM de l'université de Liège d'avoir partagé leur expertise du moussage CO_2 supercritique.

Merci à Nicolas Quiévy et Stéphanie Eggermont pour m'avoir aidé à me lancer dans cette aventure.

J'ai aussi une pensée pour les équipes techniques du LACAMI, de WELCOME et du BSMA sans qui cette thèse ne serait restée que des idées farfelues. Grâce à leur dévouement et leur expertise, ils ont réussi à

créer et faire ”parler” les échantillons afin de rendre cette thèse encore plus intéressante. Je m'en voudrais de ne pas citer de noms, donc merci, Marc, Jonathan, Alban, David, Pascal et Michel.

Je remercie l'IMAP où bonne humeur et rigueur scientifique sont omniprésentes. On dit que pour être bien au travail, il faut que celui-ci vous donne envie de se lever le matin. Dans mon cas, l'IMAP y est pour beaucoup, notamment avec ses pauses aux discussions sérieuses ou délirantes, le sacré badminton du mardi midi, suivi de la non moins sacrée ”pita medium maison à l'ail avec le pain pas trop cuit”, sans oublier tous les autres moments de détente ”pendant que mon code compile”. Merci à Arnaud et Xavier mes collègues du 18-20h et plus, à Laurence, Maxime et Fred, la ”team” Abaqus, aux deux blondies, Anne-Sophie et Astrid, pour m'avoir diverti et nourri aux pauses, à Michaël et Renaud pour m'avoir présenté une version alternative du doctorant, à Matthieu pour son humeur bien à lui, à Yann-Alex pour les échantillons composites et le reste, à Philippe pour les dégustations de whisky, à Marie-Stéphane et Barbara pour leur grain de folie pendant les heures de bureau. Sans oublier Camille, ma collègue de bureau depuis le début, qui a su s' accommoder de ma conception bien personnelle du rangement et de la décoration.

Lorsque j'avais besoin de souffler, j'ai toujours pu compter sur ma famille et mes amis pour me proposer des soupers, des soirées jeux, cinémas et autres activités récréatives.

Et enfin Marie, qui a su me comprendre, me supporter et surtout m'apporter un soutien sans faille durant toutes les phases du doctorat, de la mise en route au stress final de la rédaction.

Contents

Chapter 1

Scientific, technological motivations and objectives

In a world where wireless technologies generalize in all compartment of daily life, electromagnetic (EM) pollution and electromagnetic interferences have to be reduced at a low level, whether it is to protect living cells or to preserve the operation of sensitive electronic devices and systems. In most applications, the unwanted radiation is either confined at the source or the device itself is shielded against it by a metallic enclosure that reflects the incident radiation.

Such shielding is known for a long time as the Faraday cage effect operating from DC to high frequency and based on the reorganization of electric charges in the shielding conductor in order to cancel the total electric field inside or outside the cage, depending on the position of the source.

Most of the time a Faraday cage is satisfactory. But some specific applications require a shielding with a true absorption of the EM energy which implies no reflection and no transmission of the incoming EM radiation. One of them is radar stealth, which consists in reducing the detectability of a vehicle by cancelling reflection of a radar signal incident to its surface.

So-called Radar Absorbing Materials (RAM) can be processed under different forms: conductive paints or rubbers loaded with ferrite and/or carbon black particles were developed for stealth military planes by various countries (information is most often classified), while conductive foams and/or multilayered topologies are commonly used as liners for all enclosures in which reflection of waves has to be minimized, such as in anechoic chambers used as reference test environment for Electromagnetic Compatibility and ElectroMagnetic Interference (EMI) shielding certification measurements.

The absorption capacity of a RAM layer, A, defined as the ratio of the absorbed power to the input power, depends, in addition to the material thickness and the operating frequency, on the effective dielectric constant ϵ_{eff} and on the effective electrical conductivity σ_{eff} of the material or system.

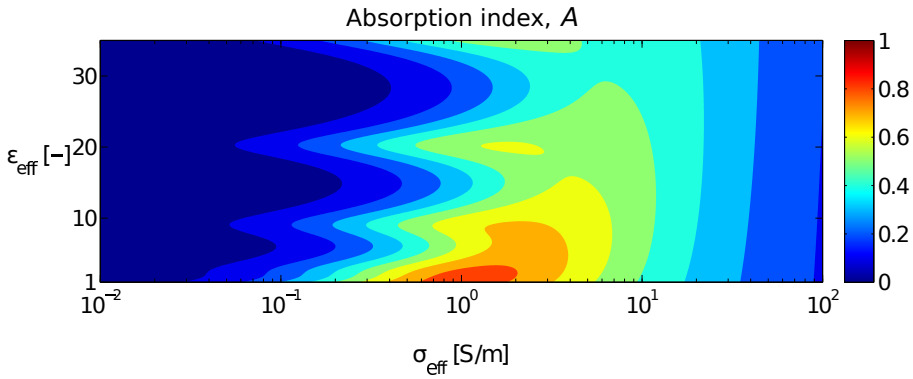

Figure 1.1: *Absorption index A for a layer of 10 mm at a frequency of 10 GHz. In blue no absorption, in red A is equal to 1*

The analysis of the closed-form expression for the absorption A, which will be explained in the core of the thesis, represented in Figure 1.1, shows that the best absorption of a radiated wave at 10 GHz is attained when ϵ_{eff} is as small as possible (hence, ideally equal to 1) and when σ_{eff} is close to $1\,\mathrm{S{\cdot}m^{-1}}$.

A more extensive analysis allows the determination, for a monolayer single material of effective permittivity equal to 1, of the ideal electri-

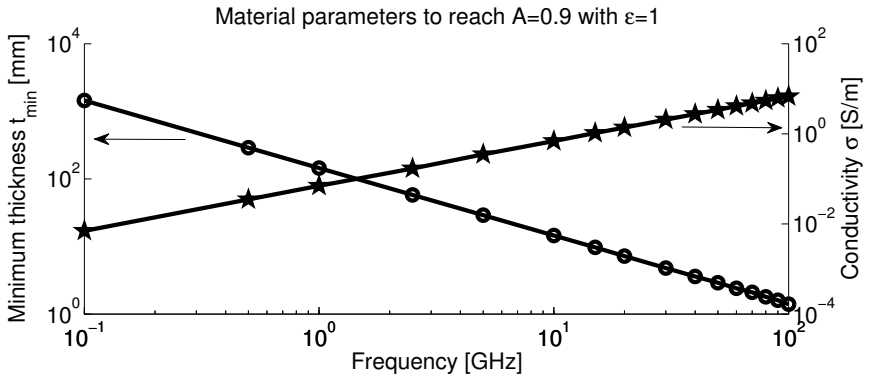

Figure 1.2: *Minimum thickness and effective conductivity to achieve an absorption index of 0.9 at frequencies in the range of 0.1 to 100 GHz with a dielectric constant set to 1 in logarithm scale*

cal conductivity required to reach $A = 0.9$ in the gigahertz range while minimizing the thickness. As shown in 1.2, keeping a high absorption index at lower frequencies requires increasing the thickness and decreasing the conductivity of the material in an exponential way. Thicknesses of 10 and 100 cm are required to absorb 90% of the incoming power at frequencies of 1 and 0.1 GHz, respectively.

It turns out, as shown in the materials chart in Figure 1.3, that no single material possesses the right combination of permittivity and conductivity to reach $A = 0.9$, or simply, to absorb even a minute fraction of the EM radiation with realistic thicknesses. The range of electrical conductivity allowing high absorption is indeed extremely narrow. The need for an architectured/hybrid material solution naturally emerges. The strategy followed, shown in black in Figure 1.3, first relies on a polymer material in order to start with a small dielectric constant, hence a small reflectivity. In order to reach the expected conductivity, around $1\,\mathrm{S{\cdot}m^{-1}}$, the polymer is filled with carbon nanotubes (CNTs) as seen in Figure 1.4.a. A small amount of CNT is indeed known to significantly raise the conductivity at high frequency owing to the existence of electrical capacitances between the closely spaced nanotubes [1]. However, in parallel to the increase in the electrical conductivity, the dielectric constant

also increases due to the presence of the CNT which adversely impacts the reflectivity. In order to further reduce the dielectric constant, open space is introduced in the nanocomposite by foaming while keeping the high conductivity brought in by the nanofiller, hence providing high absorption levels, Figure 1.4.b. This material naturally possesses the main advantages of foams, i.e. low density and good thermal insulation which is not always desired.

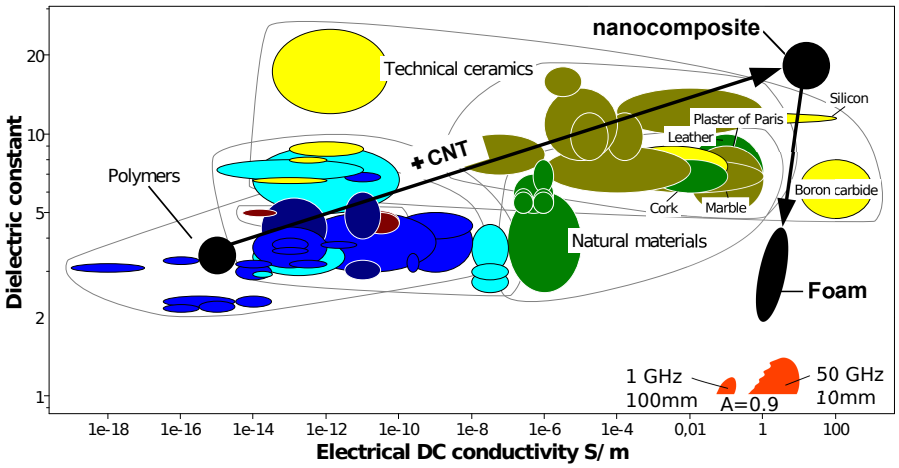

Figure 1.3: *Dielectric constant versus electrical conductivity material chart. The red zone corresponds to combination of ϵ and σ allowing an absorption of 90% for a monolayer of material with thickness of 100 mm at 1 GHz and 10 mm at 50 GHz. In black, the strategy to build a material with optimum properties is illustrated.*

But this foam is unable to carry large mechanical load and therefore cannot be used as a structural component as such. In order to obtain a EM absorbing structure, an other material is needed to carry the load and protect the foam. In order to improve the global performances and to reduce the weight of this structure, a multifunctional material can be used. Combination of the EM absorption and the structural function can be achieved by reinforcing the nanocomposite foam.

The reinforcement is done at two scale levels. At the millimetre scale, a metallic honeycomb (HC) is inserted in the foam as illustrated in Figure

1.4.c. The combination of the metallic honeycomb and of the polymeric foam provides high crushing performance. Indeed, as we will explain in more detail in the thesis, the presence of the foam positively impacts the buckling of Al honeycomb faces by forcing small wavelengths [2]. In terms of EM behaviour, the metallic HC introduces a cutoff frequency below which no propagation inside the cell is allowed. Above this frequency, the effective permittivity of the hybrid foam/HC is lower than the permittivity of the nanocomposite foam, allowing further reduction of the reflectivity.

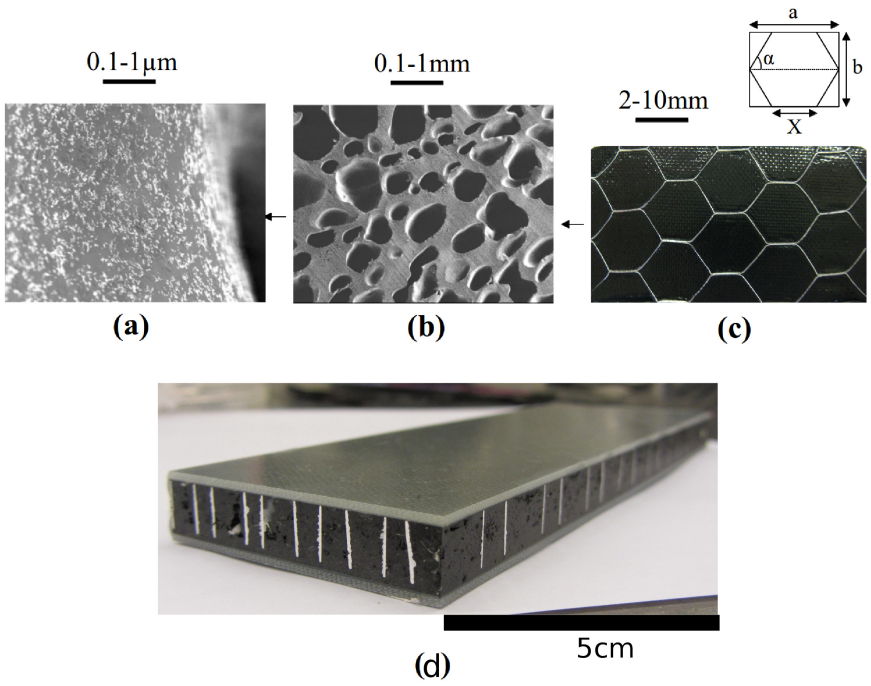

Figure 1.4: *Multimaterial and multiscale strategy developed to reach high EM absorption levels in the GHz range for sandwich panel. The core is made of (a) CNT dispersed in a polymer matrix (CNT appear as bright dots) which is (b) foamed and (c) inserted in a metallic honeycomb. Transparent EM faces(Glass Fiber Reinforced Polymer) is bond to the hybrid core (d).*

At the centimeter scale, the hybrid is used as the core of a sandwich panel obtained by the addition of one or two EM transparent face sheets made of glass fibers reinforced polymer, as shown in Figure 1.4.d. A careful design of face sheets will be needed to preserve and even improves the EM absorption performances of the hybrid in a specific frequency range.

The starting point of this thesis was the research project MULTIMASEC funded by the Walloon region. It was a collaboration between three research institutes from the Université catholique de Louvain, i.e. the institute of Information and Communications Technologies, Electronics and Applied Mathematics (ICTEAM), the Institute of Mechanics, Materials and Civil Engineering (IMMC) and the Institute of Condensed Matter and Nanosciences (IMCN), together with the Center for Education and Research on Macromolecules (CERM) at the Université de Liège.

Electromagnetic absorbers with good mechanical performance have not been much studied in the literature. The objectives of this thesis is to go beyond the state of the art on electromagnetic absorbers by proposing a multifunctional material with high mechanical performance and high EM absorption capacity suitable to large scale production. A side objective is to develop an analytical model for the EM absorption which will allow the determination of the optimal design at low computational cost.

Many aspects of materials engineering will be covered in the course of this thesis. Chapter 2 will present some general advantages and drawbacks of architectured and hybrid materials as well as the different solutions available today to absorb EM radiation. Once the design of the architectured material is done, the question of the best processing routes as a function of the application remains open and might be the limiting factor in the practical optimization. As often, development of complex hybrids is limited by processing issues. Chapter 3 will present and discuss the different processing strategies that have been addressed in order to provide constraints for the optimization as well as guidelines for the possible upscaling. The EM characterization and the absorption modelling of the hybrid and the sandwich panel are presented in Chapter 4. To allow the absorption below the cutoff frequency of the

foam filled honeycomb, split ring resonators (SRR) are inserted inside the HC cell. The SRRs give to the hybrid metamaterial characteristics. This approach and the results are presented in Chapter 5. Chapter 6 presents the mechanical properties of the hybrid and of the sandwich panel. It will focus on the bending stiffness and on the impact resistance of the panel. A procedure is proposed in Chapter 7 for the design of a sandwich panel that combines high bending stiffness and EM absorption while keeping a low weight and a small thickness. Finally, Chapter 8 presents some suitable applications requiring such multifunctional material. The logic and connections among Chapter 3 to 8 are represented in Figure 1.5.

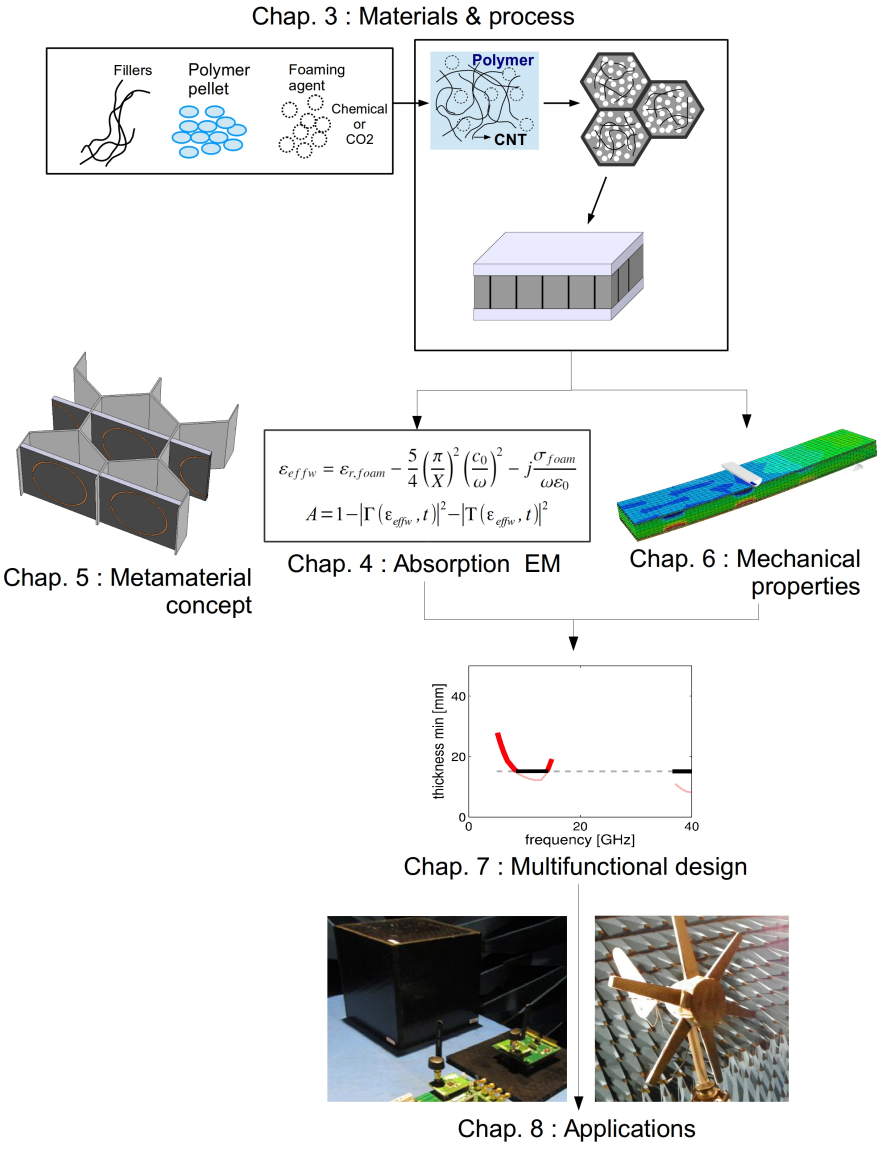

Figure 1.5: *Graphical outline of the thesis organization*

Chapter 2

State of the art

2.1 Hybrid and architectured materials

This section is inspired by chapter 11 of *Materials Selection in Mechanical Design* written by M.Ashby [3]. Hybrid materials consist of a combination of two or more materials that result in a set of properties that does not exist in monolithic material. Numerous ways of mixing/combining materials might be used. Each of them has its own advantages and drawbacks. The hybrid families are defined as the composites, sandwich structures, cellular structures and segmented structures. Basic informations and material properties models for each of these families of hybrids are provided in this section as each of them will be addressed in the context of this thesis.

2.1.1 Filling holes in the material-property space

All material property charts include empty space that might be of interest, like the chart in Figure 1.3. One approach to fill the holes is to develop new metallic alloys, new polymer chemistries or new ceramic and glass materials. Doing so is costly in time and resources while the results remain uncertain and often incremental. The other approach is

to combine two or more materials in a particular arrangement to combine their properties. Depending on the configuration, on the volume fraction and on the properties, several scenarios may occur as illustrated in Figure 2.1 where two materials M_1 and M_2 are plotted on a chart with properties P_1 and P_2 that must be maximized.

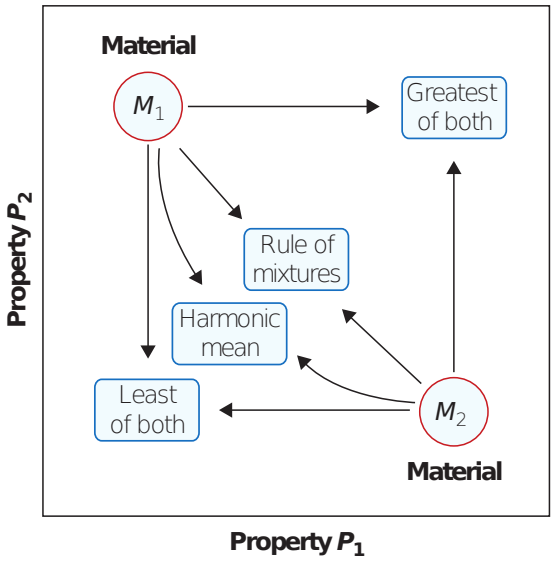

Figure 2.1: *From [3], the possibilities of hybridization. The properties of the hybrid reflect those of its component materials, combined in one of several possible ways.*

A hybrid made of these two materials can show properties P_1 and P_2 that are:

The best of both. This is the ideal case. Most common example is when a bulk properties of one material is combine with the surface properties of an other. Zinc-coated steel has the strength and stiffness of steel and corrosion resistance of zinc.

The rule of mixtures. Final properties are an arithmetic average of the properties of each material weighted by their volume fraction. This often happens when P_1 and P_2 are bulk properties. Unidi-

rectional fiber composites have an axial modulus (parallel to the fibers) close to the rule of mixture.

The harmonic mean. Sometimes, the weak properties dominate and the hybrid properties fall below the arithmetic mean, closer to the harmonic mean. Stiffness of particulate reinforced composites exhibits such a behaviour.

The least of both. In this scenario, the weakest properties of both materials dictate the hybrid final properties. It occurs for the electrical conductivity for composite made of an insulator and a conductor if no electrical path exists in the material, for instance for low volume fraction of metallic powder in a polymer matrix.

2.1.2 Composites

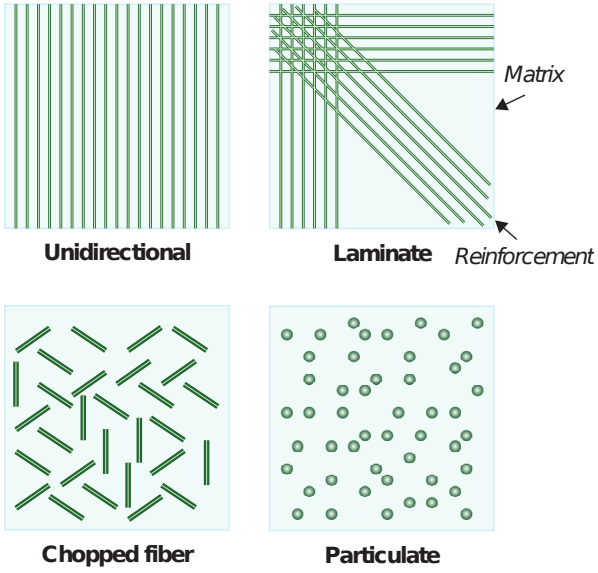

Figure 2.2: *From [3], Schematic of hybrids of the composite type: unidirectional fibrous, laminated fiber, chopped fiber, and particulate composites.*

Composites are a mix of two materials. Mixing can be performed with many geometries (Figure 2.2). Composites in terms of hybrid materials are usually fully dense and strongly bonded, there is no tendency to decohesion when loaded, and the length-scale of the reinforcement is much larger than the atomic or molecular scale. With this condition, at a macroscopic scale (much larger than the reinforcement), a composite behaves as a homogeneous material with its own set of effective materials properties. Calculation of these properties can be performed precisely but requires a precise description of the geometry and is time-consuming. Most of the time, upper and lower bounds for the properties are sufficient and can easily be calculated without taking care of the geometries presented in Figure 2.2.

Effective materials properties

Density. The apparent density, $\tilde{\rho}$, of a composite material can be precisely calculated thanks to the rule of mixture. Considering a volume fraction f of reinforcement of density ρ_r in a matrix of density ρ_m, $\tilde{\rho}$ writes as

$$\tilde{\rho} = f\rho_r + (1-f)\rho_m \quad . \tag{2.1}$$

Mechanical properties. The effective Young's modulus $\tilde{E}$ of the composite is bracketed by the Voigt and Reuss bounds. If in a loaded composite, the same strain is supported by both components, the apparent modulus is the upper bound $\tilde{E}_{up}$, given by the rule of mixture

$$\tilde{E}_{up} = fE_r + (1-f)E_m \tag{2.2}$$

with E_r the modulus of the reinforcement and E_m the modulus of the matrix.

If on the contrary, the same stress is applied to both components, the lower bound, $\tilde{E}_{low}$, applies as given by

$$\tilde{E}_{low} = \frac{E_r E_m}{fE_r + (1-f)E_m} \quad . \tag{2.3}$$

Determining lower and upper bounds for the failure stress or strength of a composite is not an easy task because of the non linearity of the problem and the multitude of possible modes of failure. A simplified model for unidirectional fiber or particulate reinforcement can still be established.

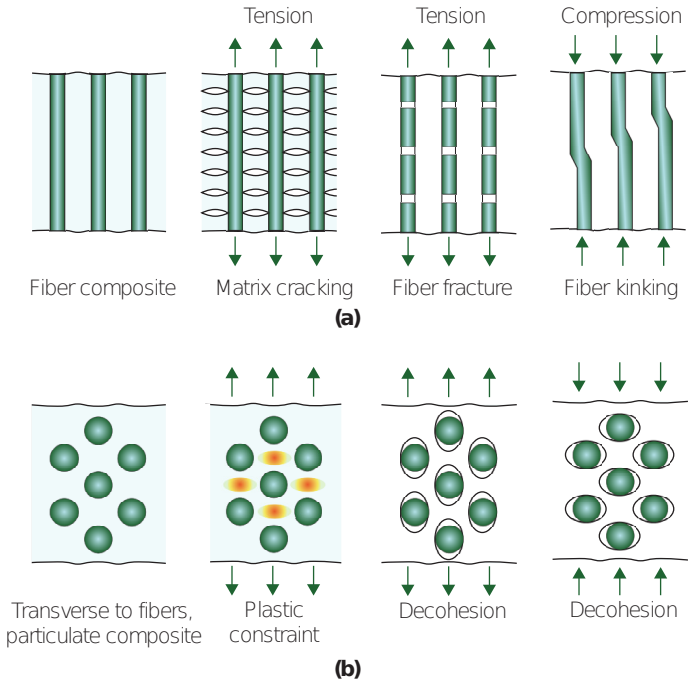

Figure 2.3: *From [3], failure modes in composites; (a) axial loading of unidirectional fiber composite, (b) loading of particulate composite or transversal loading of fiber composite.*

A fibrous composite loaded in the direction of the fibers will deform until one of the components totally fails, as illustrated in Figure 2.3(a). At this point, the load is redistributed inside the intact component. The fracture strength in the axial direction, $\tilde{\sigma}_{f,a}$, will be :

$$(\tilde{\sigma}_f)_{L,a} = \text{greater of } \left[f\,(\sigma_f)_r\,, (1-f)\,(\sigma_f)_m\right] \tag{2.4}$$

where $(\sigma_f)_r$ and $(\sigma_f)_m$ are the fracture stresses of the reinforcement and matrix respectively. If both the reinforcement and matrix fail at

the same applied load, the composite will be the strongest. In this case the upper bound, $(\tilde{\sigma}_f)_{u,a}$, is given by the rule of mixture

$$(\tilde{\sigma}_f)_{L,a} = f\,(\sigma_f)_r + (1-f)\,(\sigma_f)_m \quad . \tag{2.5}$$

Figure 2.3(b) shows the case of a reinforcement by particles or when the fiber composite is loaded in the transverse direction. The transverse strength is then more difficult to estimate. In this case, the upper bound (the matrix flow is constrained) is given by :

$$\text{lesser of } \begin{cases} (\tilde{\sigma}_f)_{u,t} \approx (\sigma_f)_m \left(\dfrac{1}{1-f^{1/2}}\right) \\ (\tilde{\sigma}_f)_{u,t} \approx (\sigma_f)_r \end{cases} \tag{2.6}$$

and the lower bound (debonding and stress concentration):

$$(\tilde{\sigma}_f)_{L,t} \approx (\sigma_f)_m \left(1-f^{1/2}\right) \tag{2.7}$$

Figure 2.4 shows the upper and lower bound for a epoxy-glass fiber composite axially loaded (a) or transversally loaded (b).

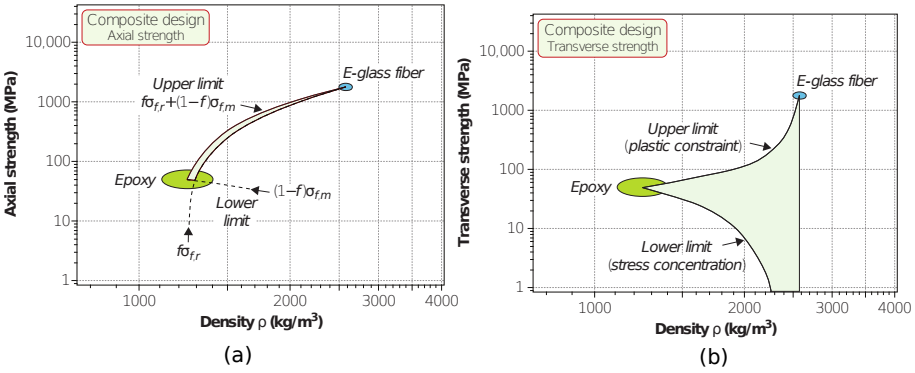

Figure 2.4: *From [3], the limits for axial (a) and transverse (b) strength of a composite ply.*

Electrical properties. The dielectric constant of a composite, $\tilde{\varepsilon}$ can be given by the rule of mixture:

$$\tilde{\varepsilon} = f\varepsilon_r + (1-f)\,\varepsilon_m. \tag{2.8}$$

If the electrical conductivities of both components of the composite have the same order of magnitude, the electrical conductivity of the composite follows the rule of mixture :

$$\tilde{\sigma} = f\sigma_r + (1-f)\,\sigma_m. \tag{2.9}$$

When the electrical conductivities of the components differ by many orders of magnitude, $\tilde{\sigma}$ is dependent on the presence of a percolating network as well as on the quality of the dispersion, on the orientation and on the aspect ratio of the reinforcement. More details about the EM effective properties of composite are given later in the thesis as this is a central part of the analysis.

2.1.3 Cellular structures

Cellular structures are hybrids made of solid and gas. They are divided in two main types : foams and lattices. Foams are bending dominated structures, see Figure 2.5, while lattices are stretching dominated, see Figure 2.6. Honeycombs enter both categories, their in plane properties are bending dominated but their out of plane are stretching dominated [4]. Usually cellular solids are characterized by their relative density $\left(\frac{\tilde{\rho}}{\rho_s}\right)$.

The compressive stress-strain curve of bending dominated cellular materials is represented on Figure 2.7. Such materials exhibit a linear elastic behaviour with modulus $\tilde{E}$. When the elastic limit is reach, the cell edges yield, buckle or break. The collapse of the foam continues at a nearly constant stress $\tilde{\sigma}_{pl}$ until opposite sides of the cell are in contact. At this point there is a densification of the material and the stress rises rapidly.

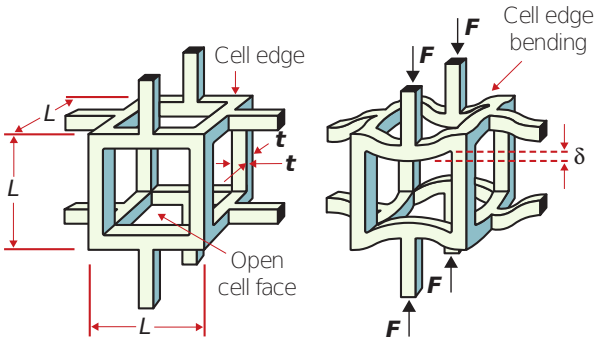

Figure 2.5: *From [3], cell of a low density foam. When loaded, the cell edges bend, giving a low modulus structure.*

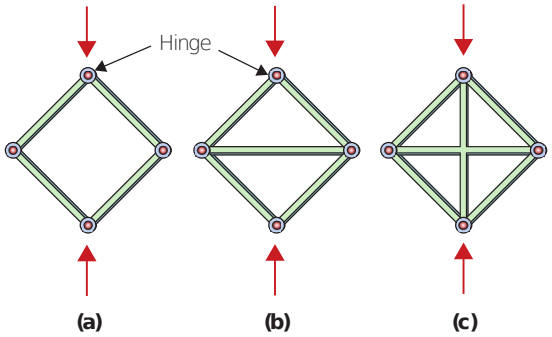

Figure 2.6: *From [3], the pin-jointed frame at (a) is a mechanism. If its joints are welded together, the cell edges bend. The pin-jointed, triangulated frame at (b) is stiff when loaded because the transverse bar carries tension, preventing collapse. When the frame's joints are welded, its stiffness and strength hardly change. The frame at (c) is over-constrained. If the horizontal bar is tightened, the vertical bar is put in tension even when there are no external loads.*

Equivalent materials properties

Mechanical properties. The equivalent elastic modulus, $\tilde{E}$, of an open cellular structure can be obtained by scaling the bending deformation of the edges under external load :

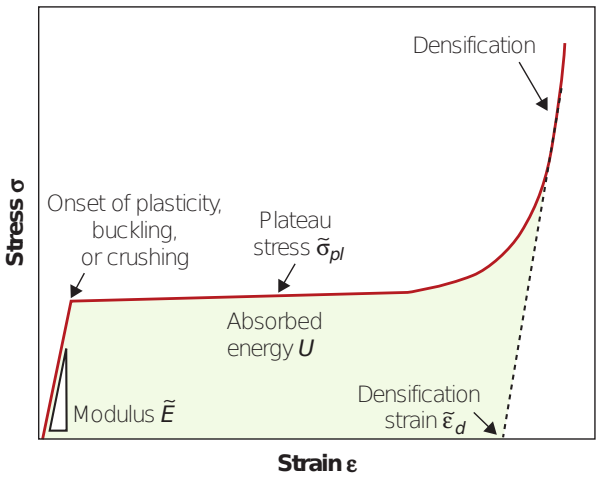

Figure 2.7: *From [3], the plateau stress is determined by buckling, plastic bending, or fracturing of the cell walls.*

$$\frac{\tilde{E}}{E_s} \approx \left(\frac{\tilde{\rho}}{\rho_s}\right)^2 \quad . \tag{2.10}$$

The same scaling approach can be used to approximate the plateau stress, $\tilde{\sigma}_{pl}$, of a foam which collapses by yielding or crushing

$$\frac{\tilde{\sigma}_{pl}}{\sigma_{f,s}} \approx 0.3 \left(\frac{\tilde{\rho}}{\rho_s}\right)^{3/2} \tag{2.11}$$

with $\sigma_{f,s}$ the yield or fracture stress of the solid. In the case of an elastomeric foam, the cells collapse by the buckling of the edges which gives for the plateau stress

$$\frac{\tilde{\sigma}_{pl}}{E_s} \approx 0.05 \left(\frac{\tilde{\rho}}{\rho_s}\right)^2 \quad . \tag{2.12}$$

The elastic properties of an hexagonal honeycomb, from which one cell is represented on Figure 2.8, can also be approximated from the bending deformation of the cell walls [4] [5]. This approach is valid if the wall thickness, t, is small compared with the wall length, l.

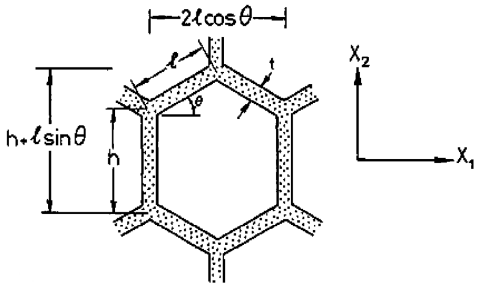

Figure 2.8: *From [4], hexagonal cell*

For a given geometry of the cell, Figure 2.8, the equivalent density, $\tilde{\rho}$ is

$$\frac{\tilde{\rho}}{\rho_s} = \left(\frac{t}{l}\right) \frac{h/l + 2}{2\ cos\ \theta(h/l + sin\ \theta)} \quad . \tag{2.13}$$

Table 2.1 gives the in-plane and out-of-plane elastic properties of hexagonal honeycomb [5]. Further reading about bending of honeycomb can be found in [6].

In-plane properties	Out-of-plane properties
$\frac{\tilde{E}_1}{E_s} = \left(\frac{t}{l}\right)^3 \frac{cos\ \theta}{(h + l\ sin\ \theta)sin^2\theta}$	$\frac{\tilde{E}_3}{E_s} = \frac{\tilde{\rho}}{\rho_s}$
$\frac{\tilde{E}_2}{E_s} = \left(\frac{t}{l}\right)^3 \frac{h/l + sin\ \theta}{cos^3\theta}$	
$\tilde{\nu}_{12} = -\frac{\varepsilon_2}{\varepsilon_1} = \frac{cos^2\ \theta}{(h/l + sin\ \theta)\ sin\ \theta}$	$\tilde{\nu}_{31} = \tilde{\nu}_{32} = \nu_s$
$\tilde{\nu}_{21} = -\frac{\varepsilon_1}{\varepsilon_2} = \frac{(h/l + sin\ \theta)sin\ \theta}{cos^2\ \theta}$	$\tilde{\nu}_{13} \approx \tilde{\nu}_{23} \approx 0$
$\frac{\tilde{G}_{21}}{E_s} = \left(\frac{t}{l}\right)^3 \frac{h/l + sin\ \theta}{(h/l)^2\ (1 + 2h/l)\ cos\ \theta}$	$\frac{\tilde{G}_{13}}{E_s} = \frac{\tilde{G}_{23}}{E_s} = 0.577\left(\frac{t}{l}\right)$, for regular hexagons

Table 2.1: *From [4], elastic properties of hexagonal honeycomb.*

Electrical properties. The equivalent electrical properties of cellular materials can be approximated in the same way as for composite materials with one of the phases being the gas filling the cell (most of the time air or blowing agent for closed cell polymeric foams).

2.1.4 Sandwich structures

A sandwich panel, Figure 2.9, is a laminar structure where two sheets of a material with good mechanical performances are bonded to each side of a thick low density material. Such material arrangement shows high bending stiffness and strength for a low overall weight. Indeed, the moment of inertia of the section, I and the section modulus Z are increased thanks to the separation of the faces by the core.

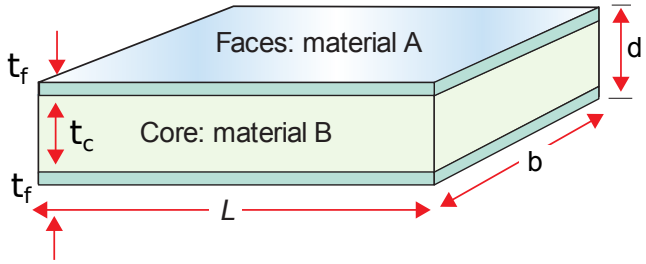

Figure 2.9: *From [3], the sandwich. The face thickness is t_f, the core thickness is t_c, and the panel thickness is d.*

In a sandwich panel in bending, most of the load is carried by the faces that need to be stiff and strong. The core, which occupies most of the volume, carries the shear stress in order to ensure the load transfer from one face to the other. This requires a light and stiff core. With this requirement, the faces are typically made of a composite material or a metal and the core is made of a cellular material.

Equivalent materials properties

Density. The equivalent density of the panel is

$$\tilde{\rho} = f\rho_f + (1-f)\rho_c \tag{2.14}$$

with ρ_c the core density, ρ_f the density of the faces, f the volume fraction occupied by the faces which is equal to $2t_f/d$.

Mechanical properties. The rule of mixture gives a good approximation for the in-plane modulus $\tilde{E}_{in-plane}$ and strength $\tilde{\sigma}_{in-plane}$ of a sandwich panel.

The purpose of a sandwich panel is to be stiff and strong during bending. In bending, the deformation of the panel has two contributions: one comes from the bending of the faces and the core as a whole, the other comes from the shear of the core as illustrated in Figure 2.10.

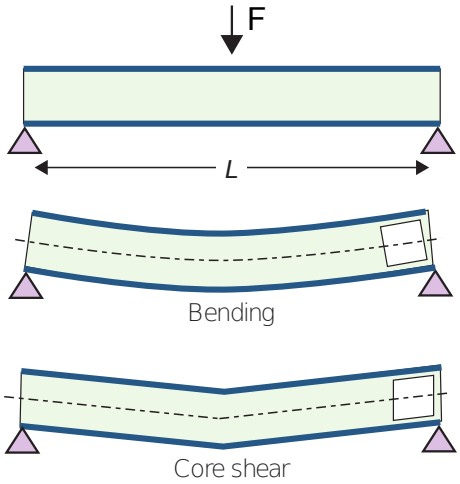

Figure 2.10: *From [3], sandwich panel flexural stiffness. There are contributions from bending and core shear.*

The bending stiffness per unit width, D, of the panel is the sum of the stiffness of the faces about their individual neutral axis, D_f, the stiffness of the faces about the middle axis, D_0, and the bending stiffness of the core, D_c [7]:

$$D = 2D_f + D_0 + D_c = \frac{E_f t_f^3}{6} + \frac{E_f(d^3 - t_c^3)}{12} + \frac{E_c t_c^3}{12} \tag{2.15}$$

with E_f the modulus of the faces and E_c the modulus of the core. D_f

can be neglected for thin faces, $d > 5.77t_f$, and D_c can be neglected if the modulus of the core is small compared to the face modulus, $E_c \ll E_f$.

Using the approximation for a sandwich with thin faces and weak core the shear stiffness of the panel, S, is

$$S = \frac{d^2 G_c}{t_c} \tag{2.16}$$

with G_c the shear modulus of the core.

The deflection per unit width, δ, of a panel with thin faces and a span length L is the sum of the deflection due to bending, δ_b and due to shear δ_s,

$$\delta = \delta_b + \delta_s = \frac{12FL^3}{B_1\left[(d^3 - t_c^3)E_f + t_c^3 E_c\right]} + \frac{FLt_c}{B_2 d^2 G_c} \quad . \tag{2.17}$$

The constant B_1 and B_2 depend of the load configuration and are determined in Table 2.2. The deflection of a panel made with an equivalent material of modulus $\tilde{E}$ gives,

$$\delta = \frac{12FL^3}{\tilde{E}d^3}. \tag{2.18}$$

The comparison gives

$$\frac{1}{\tilde{E}} = \frac{1}{E_f\left[\left(1-(1-f)^3\right) + \dfrac{E_c}{E_f}(1-f)^3\right]} + \frac{B_1}{B_2}\left(\frac{d}{L}\right)^2 \frac{(1-f)}{G_c}. \tag{2.19}$$

The first term of equation (2.19) corresponds to the flexural contribution while the second term is the transverse-shear contribution. Because the latter depends of the the loading configuration with the ratio B_1/B_2, the equivalent bending modulus of a sandwich panel is not an intrinsic property but a performance metric.

Figure 2.3 shows how the shear deformation of the core knocks down the equivalent bending modulus of sandwich [8], especially for thick faces and high modulus contrast between the core and the faces. For a given

Mode of Loading	Description	B_1	B_2
1 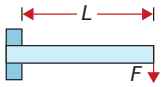	Cantilever, end load	3	1
2 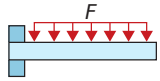	Cantilever, uniformly distributed load	8	2
3 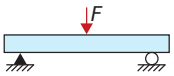	Three-point bend, central load	48	4
4 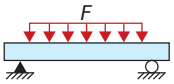	Three-point bend, uniformly distributed load	384/5	8
5 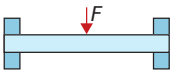	Ends built in, central load	192	4
6 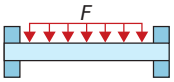	Ends built in, uniformly distributed load	384	8

Table 2.2: *From [3], constants entering the bending stiffness equation for different loading modes of beams.*

type of loading, the shear contribution, ϵ, depends on the relative thickness h/L and is equal to

$$E_f \left[\left(1-(1-f)^3\right) + \frac{E_c}{E_f}(1-f)^3 \right] \left(\frac{d}{L}\right)^2 \frac{(1-f)}{G_c} = \epsilon \quad . \tag{2.20}$$

Four domains, named A B C and D, emerge from Figure 2.3. In domain A, ϵ is smaller than 0.01 meaning that the transverse shear contribution is negligible and the classical beam theory is valid. In domain B, $\epsilon < 0.1$, the the shear contribution becomes relevant, the classical beam theory is mainly valid except for concentrated load. In domain C, $\epsilon < 10$ meaning that the transverse-shear is dominant and must be taken into consideration. In domain D, $\epsilon > 10$, the beam model is no longer valid.

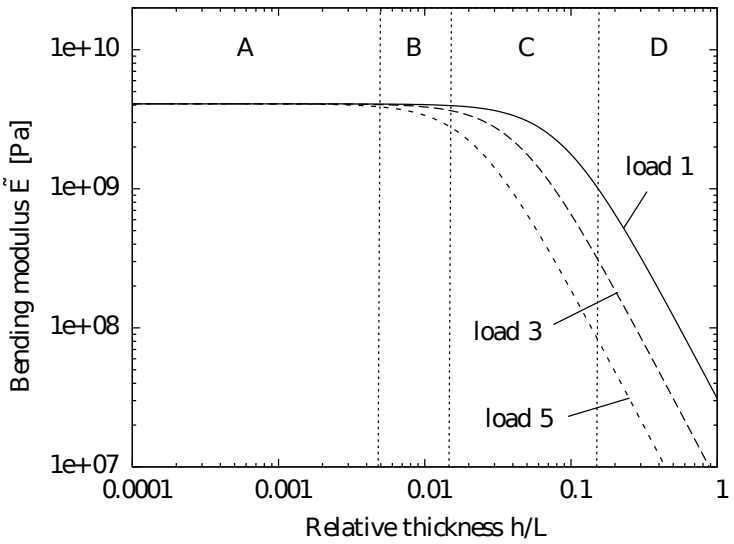

Table 2.3: *From [8], evolution of the bending modulus versus the slenderness for three types of loading (the load numbered 1, 3 and 5 from Table 2.2). Four domains, from A to D, are identifiable respectively to the intensity of the shear contribution. The boundaries of these domains (the vertical dashed lines) are given by the equation (2.20) for* $\epsilon = 0.01, 0.1$ *and* 10.

Thermal properties. The out of plane thermal conductivity, $\tilde{\lambda}_\perp$, of a sandwich panel is the harmonic mean

$$\tilde{\lambda}_\perp = \left(\frac{f}{\lambda_f} + \frac{(1-f)}{\lambda_c} \right)^{-1}. \tag{2.21}$$

2.1.5 Segmented structures

Segmented structures are mainly used for two objectives, for reducing the bending stiffness while keeping a high tensile strength or for damage tolerance. Flexible cables, leaf spring and other structures can easily flex compared to a monolithic solid of same surface section. Indeed, a n leafs panel has a bending stiffness lowered by a factor $1/n^2$.

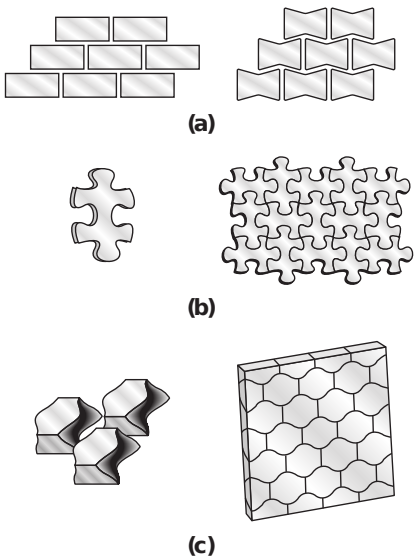

Figure 2.11: *From [3], examples of topological interlocking: discrete, unbonded structures that carry load. (a) Bricklike assemblies of rectangular blocks carry axial compression, but not tension or shear. (b) The 2-dimensional interlocking of a jigsaw puzzle carries in-plane loads. (c) Units that, when assembled into a continuous layer and clamped within a rigid boundary around the edges of the layer, can carry out-of-plane loads and bending moments.*

Segmented panels, illustrated in Figure 2.11, show an improved damage tolerance compared to a monolithic brittle panel. When such panels are hit by a projectile, some bricks may be lost locally but the panel will not totally shatter. By subdividing the material, a crack cannot propagate from one block to an other, limiting the damage to a local failure without global failure.

Mixing segments of different materials give interesting sets of properties. As an example, suspended power cables must have an electrical resistivity as low as possible and at the same time a high tensile strength to allow greatest span. As illustrated in Figure 2.12, no material lies in the region of interest. Now consider a cable with half the strands made of copper and the other half of steel. In the more pessimistic scenario,

where copper does not carry any load and steel no current, the resistivity of the cable is the one of copper multiplied by a factor 2 and the yield strength is the one of steel divided by a factor 2. As it can be seen, the effective properties still fill the hole in the chart.

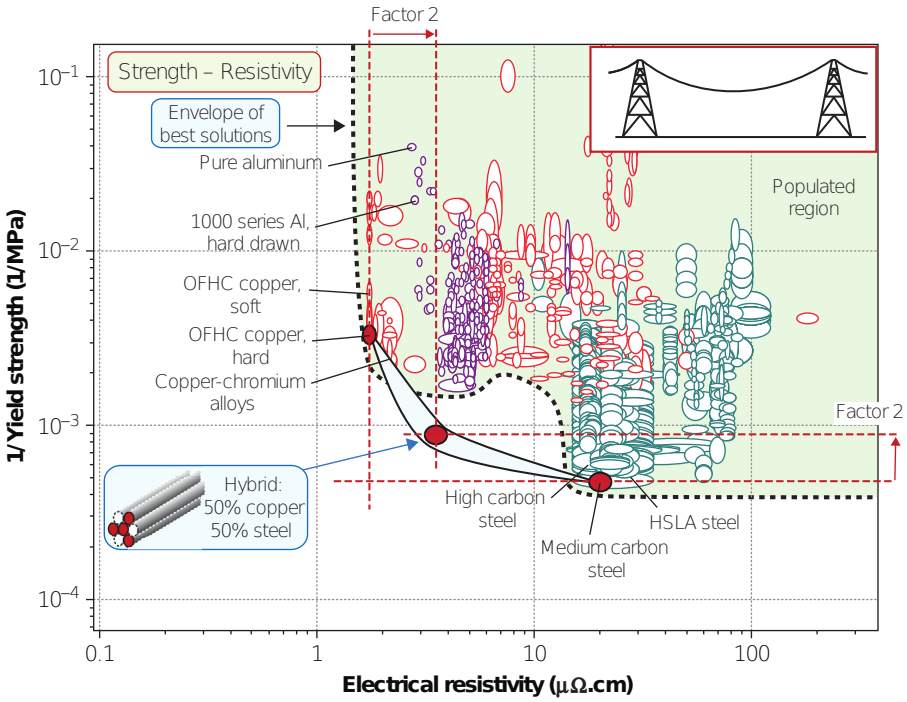

Figure 2.12: *From [3], designing a hybrid-here one with high strength and high electrical conductivity. The figure shows the resistivity and reciprocal of tensile strength for 1,700 metals and alloys. The construction is for a hybrid of hard-drawn OFHC copper and drawn medium carbon steel, but the figure itself allows many hybrids to be investigated.*

2.2 Electromagnetic absorption

In this section, the interaction between an EM wave and material will be first described. Next the different strategies to produce an absorbing layer will be presented.

To achieve a true electromagnetic absorption, the reflection needs to be as close as possible to zero while keeping no transmittance trough the material.

Two methods have been developed to create Radar absorbing material. The first one is graded interfaces and impedance matching which aims to reduce the mismatch between the incident medium and the absorbing medium. The second method is based on a resonant layer which uses resonance to obtain an effective impedance equal to that of the incident medium.

2.2.1 Electromagnetic material properties

The interaction between an EM wave and a material must be addressed in order to determine which are the parameters dictating the EM absorption. The following introduction is taken from [9] and [10].

Electromagnetic waves are propagating electric and magnetic fields. In vacuum, the relations between the electric and magnetic flux densities, D and B respectively, and the electric and magnetic fields, E and H are:

$$\begin{aligned} \bar{D} &= \varepsilon_0 \bar{E} \\ \bar{B} &= \mu_0 \bar{H} \end{aligned} \tag{2.22}$$

where ε_0, μ_0 are the permittivity and permeability of vacuum, with numerical values of $8.854 \times 10^{-12}\,\mathrm{F{\cdot}m^{-1}}$ and $4\pi \times 10^{-7}\,\mathrm{H{\cdot}m^{-1}}$.

In a dielectric material, atoms or molecules are polarized by the applied electric field $\bar{E}$. This create electric dipole moments that augment the total displacement flux, $\bar{D}$. In a magnetic material, the same phenomenon occurs to the magnetic flux $\bar{B}$: magnetic dipole moments are

aligned by the applied magnetic field $\bar{H}$ which results in magnetic polarization of the material. The electric and magnetic flux densities then take the form,

$$\begin{aligned} \bar{D} &= \varepsilon \bar{E} = \varepsilon_0 \varepsilon_r \bar{E} \\ \bar{B} &= \mu \bar{H} = \mu_0 \mu_r \bar{H} \end{aligned} \tag{2.23}$$

with ε and μ the permittivity and the permeability of the material and may depend of the frequency of the wave. These two quantities are more often compared to their vacuum values and the resulting quantities are known as the relative permittivity ε_r and relative permeability μ_r. In a linear and isotropic material, ε_r and μ_r do not depend of the magnitude and orientation of the field. In this case, they simplify into a complex number.

The real part of the relative permittivity, is the dielectric constant of the medium, ε_r'. The imaginary part is related to the loss in the medium. It is a combination of dielectric damping, ε_r'' and loss due to electrical conductivity σ. For the relative permeability, the real part is the relative permeability μ_r'. Again, the imaginary part, μ_r'' is related to loss due to damping forces; there is no magnetic conductivity because there is no real magnetic current. Both the relative permittivity and permeability express then as

$$\begin{aligned} \varepsilon_r &= \varepsilon_r' - j\varepsilon_r'' - \frac{j\sigma}{\varepsilon_0 \omega} \\ \mu_r &= \mu_r' - j\mu_r'' \end{aligned} \tag{2.24}$$

with ω the angular frequency equal to $\omega = 2\pi f$, f is the frequency.

ε_r and μ_r can be used to determine the propagation speed, c, of the EM wave in the medium as well as the impedance of the medium, η:

$$\begin{aligned} c &= \frac{1}{\sqrt{\mu_0 \varepsilon_0}\sqrt{\mu_r \varepsilon_r}} = \frac{c_0}{\sqrt{\mu_r \varepsilon_r}} \\ \eta &= \sqrt{\frac{\mu_0}{\varepsilon_0}\frac{\mu_r}{\varepsilon_r}} = \eta_0 \sqrt{\frac{\mu_r}{\varepsilon_r}} \end{aligned} \tag{2.25}$$

with c_0 the speed in vacuum, equal to $3 \times 10^8\,\mathrm{m{\cdot}s^{-1}}$, and η_0 the impedance of vacuum equal to $377\,\Omega$.

2.2.2 Effective EM properties of composite materials

The modelling approach is based on the effective medium theory (EMT). The macroscopic effective permittivity, ε_{eff}, of the real heterogeneous medium, or equivalently its dielectric constant, ε'_{eff}, and conductivity, σ_{eff}, can be predicted using EM field averaging techniques over the entire frequency range as a function of the concentration of inclusions, orientation (randomly dispersed or aligned along a particular direction) and shape aspect ratio (sphere, wire or platelet) as long as the length scale of the microstructure is small compared to the wavelength. A review of EMTs is provided in the book of Ari Sihvola [11], including the popular Bruggeman EMT and the Maxwell-Garnet approximations. The latter considers that the effective permittivity for a mixture of spherical inclusions (ε_i) in a host external medium (ε_e) having volumetric fraction f of inclusions (Fig. 2.13a and b) can be derived from a "volumetric" averaging or homogeneisation procedure.

(a) (b)

Figure 2.13: *Schematic view of the microstructure as considered effective medium theory, (a)isolated spherical particle in hosting medium, (b) random distribution of spherical particles in hosting medium*

Starting from a single inclusion, assumed spherical for simplicity, the dipole moment $\bar{P}$ of this particle is in linear relation with the surrounding electrical field $\bar{E}_e$. The coefficient of this relation, α, is called polarisability:

$$\bar{P} = \alpha \bar{E}_e. \tag{2.26}$$

The dipole moment of a homogeneous sphere is also proportional to the internal field within the inclusion $\bar{E_i}$, its volume V and the dielectric contrast between the inclusion and the medium :

$$\bar{P} = \int (\varepsilon_i - \varepsilon_e)\bar{E_i} dV. \tag{2.27}$$

The internal field for an spherical inclusion in a uniform and static field external field is also uniform, static, parallel and proportional to the external field :

$$\bar{E_i} = \frac{3\varepsilon_e}{\varepsilon_i + 2\varepsilon_e}\bar{E_e}. \tag{2.28}$$

Using equations (2.26), (2.27) and (2.28), the polarisability of a sphere subject to an external field is given by

$$\alpha = V(\varepsilon_i - \varepsilon_e)\frac{3\varepsilon_e}{\varepsilon_i + 2\varepsilon_e}. \tag{2.29}$$

The derivation of effective permittivity for a mixture of spherical inclusions (ε_i) in host external medium (ε_e) having volumetric fraction f of inclusions use a "volumetric" averaging or homogeneisation procedure. Average electric field $\bar{E}$ and displacement field $\bar{D}$ are obtained from volumetric proportions of respective fields in each medium as:

$$\bar{E} = f\bar{E_i} + (1-f)\bar{E_e}, \tag{2.30}$$

$$\bar{D} = f\bar{D_i} + (1-f)\bar{D_e}, \tag{2.31}$$

while the effective permittivity is defined from the relationship,

$$\bar{D} = \varepsilon_{eff}\bar{E}. \tag{2.32}$$

Recombination of equations (2.31) and (2.30) with (2.32) yields to

$$f\bar{D_i} + (1-f)\bar{D_e} = f\varepsilon_i\bar{E_i} + (1-f)\varepsilon_e\bar{E_e} = f\varepsilon_{eff}\bar{E_i} + (1-f)\varepsilon_{eff}\bar{E_e} \tag{2.33}$$

and, after rearranging and using equation 2.28, finally gives

$$\varepsilon_{eff} = \varepsilon_e + 3f\varepsilon_e\frac{\varepsilon_i - \varepsilon_e}{\varepsilon_i + 2\varepsilon_e - f(\varepsilon_i - \varepsilon_e)} \quad . \tag{2.34}$$

Three limiting cases are applicable:

- If $f \to 0 : \varepsilon_{eff} \to \varepsilon_e$,
- If $f \to 1 : \varepsilon_{eff} \to \varepsilon_i$,
- For dilute mixture ($f \ll 1$): $\varepsilon_{eff} \approx \varepsilon_e + 3f\varepsilon_e \dfrac{\varepsilon_i - \varepsilon_e}{\varepsilon_i + 2\varepsilon_e}$.

The Maxwell-Garnet formulation can be extended to:

- effective permeability associated to magnetic materials,
- lossy inclusions and host material, i.e.having complex permittivity (or permeability) and a function of their dielectric constant ε' and conductivity σ: $\varepsilon_i = \varepsilon_i' - j\varepsilon_i''$ with $\varepsilon_i'' = \sigma_i/\omega$ and $\varepsilon_e = \varepsilon_e' - j\varepsilon_e''$ with $\varepsilon_e'' = \sigma_e/\omega$,
- inclusions with anisotropy of constitutive parameters: permittivity and or permeability are gyrotropic or bianisotropic tensors,
- inclusions with shape anisotropy, that are modelled as ellipsoids, oriented or randomly dispersed in host (Fig. 2.14),

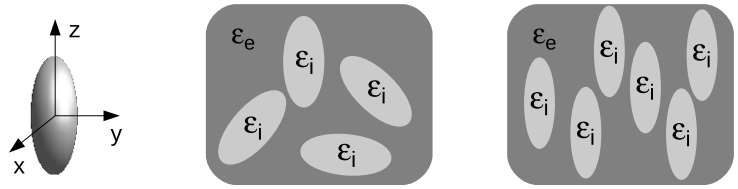

(a) (b) (c)

Figure 2.14: *(a) Generalised ellipsoid representation of nano-inclusions, having (b) random, or (c) aligned, orientation*

In particular, inclusions with shape anisotropy are modelled as ellipsoids along axes x, y and z, having associated depolarization factors N_k along each axis, affecting the ratio of internal to external electric field:

$$E_{ik} = \frac{\varepsilon_e}{\varepsilon_e + N_k(\varepsilon_i - \varepsilon_e)} E_{ek} \qquad \text{with} \quad k = x, y, z. \tag{2.35}$$

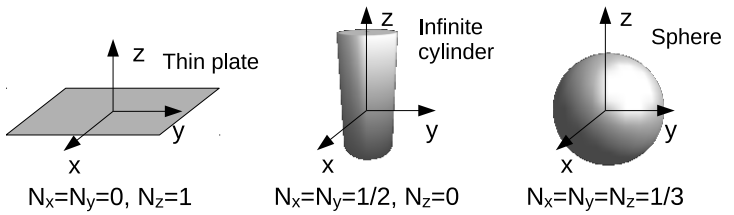

Figure 2.15: *Depolarisation factor for three particular cases of ellipsoidal inclusions*

This general expression can be particularized to three case: thin plate, sphere, and infinite cylinder (Fig. 2.15). For ellipsoids having one of their main axes aligned in the same direction (for example z-axis), the effective permittivity becomes anisotropic, i.e. values along the three k-directions of space are different:

$$\varepsilon_{eff} = \varepsilon_e + f\varepsilon_e \frac{\varepsilon_i - \varepsilon_e}{\varepsilon_e + (1-f)N_k(\varepsilon_i - \varepsilon_e)} \qquad \text{with} \quad k = x, y, z. \quad (2.36)$$

Depending on the aspect ratio of the inclusions, the resulting effective conductivity of the composite, computed from the imaginary part of the effective permittivity as $\sigma_{eff\ k} = \omega\varepsilon''_{eff\ k}$ $(k = x, y, z)$ is anisotropic or not. Figure 2.16 illustrates this fact: for spherical inclusions having an isotropic shape aspect ratio (Fig. 2.16(a)), the three components of the effective conductivity along the three spatial directions x, y, z are identical. For conductive nanotubes or nanowires (Fig.2.16(b)) all oriented along z-axis, the resulting effective conductivity is zero in the x and y directions perpendicular to the nanotube z-axis, since no conducting path can exist in these directions due to the imposed preferred orientation of the tubes.

For randomly oriented shape-anisotropic inclusions, the effective permittivity is isotropic (meaning identical expression and value along the x, y, and z direction), and given by expression (2.37), where the factor 1/3

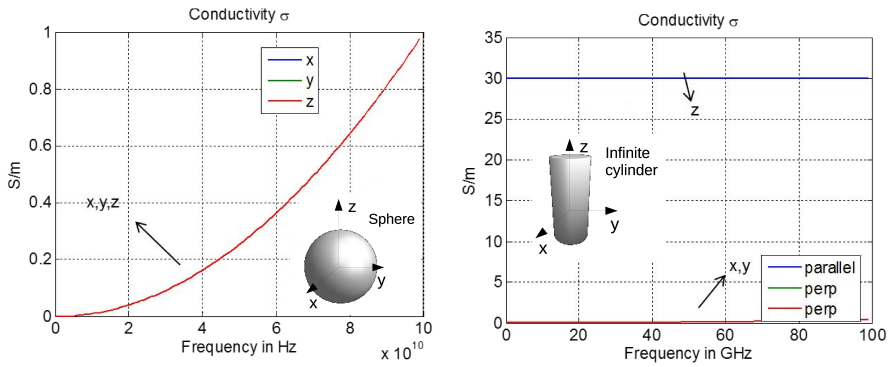

(a) (b)

Figure 2.16: *Spatial components of effective conductivity for conductive inclusions embedded in polymer insulating matrix (a) carbon black isotropic spherical inclusions (b) carbon nanotubes inclusions aligned along their z-axis*

accounts for randomization along the three directions of space:

$$\varepsilon_{eff} = \varepsilon_e + \varepsilon_e \frac{\frac{f}{3}\sum_{j=x,y,z} \frac{\varepsilon_i - \varepsilon_e}{\varepsilon_e + N_j(\varepsilon_i - \varepsilon_e)}}{1 - \frac{f}{3}\sum_{j=x,y,z} \frac{\varepsilon_i - \varepsilon_e}{\varepsilon_e + N_j(\varepsilon_i - \varepsilon_e)}}. \tag{2.37}$$

In that case, the resulting effective conductivity $\sigma_{eff} = \omega\varepsilon''_{eff}$ is also isotropic, being able to capture the influence of the aspect ratio on the percolation, as illustrated in Figure 2.17. For a given volumetric content of carbonated inclusions, percolation is already reached at low frequencies for graphene and carbon nanotubes due to their elongated shape favoring contacts between particles, while capacitive coupling is necessary to achieve efficient percolation, and becomes significant only at high frequencies.

In MG theory, the medium e is completely surrounding inclusions i. Bruggeman proposed a model to take into account the case where there is contact between inclusions and also between areas separating inclusions.

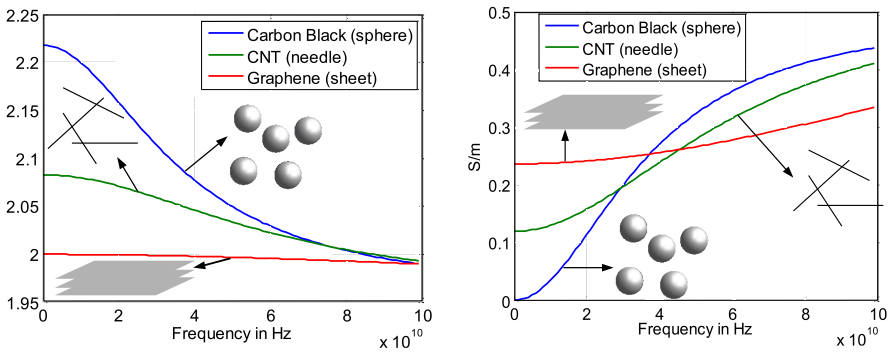

(a) Dielectric constant ε'_{eff} (b) Conductivity σ_{eff}

Figure 2.17: *Frequency response of effective dielectric constant ε'_{eff} and conductivity $\sigma_{eff} = \omega\varepsilon''_{eff}$ (right) for various carbonated inclusions in insulating polymer host matrix: graphene platelets, carbon nanotubes (CNT), and carbon black.*

This is the Bruggeman effective medium theory (B-EMT) given by the equation

$$(1-f)\frac{\varepsilon_e - \varepsilon_{eff}}{\varepsilon_e + 2\varepsilon_{eff}} = f\frac{\varepsilon_i - \varepsilon_{eff}}{\varepsilon_i + 2\varepsilon_{eff}} \quad . \tag{2.38}$$

Indeed the Maxwell-Garnet formulation (2.34) can be rearranged into

$$\frac{\varepsilon_{eff} - \varepsilon_e}{\varepsilon_{eff} + 2\varepsilon_e} = \frac{\varepsilon_i - \varepsilon_e}{\varepsilon_i + 2\varepsilon_e} \tag{2.39}$$

meaning that the polarisability of the effective medium is calculated as a volumetric fraction of polarisability of a single inclusion by virtue of equation (2.29). The Brugemman formulation (2.38) expresses that the effective medium is considered as a backgroundhost medium and that each constituent (inclusion and surrounding medium) contributes equally to the polarisability.

2.2.3 Electromagnetic absorber

Electromagnetic absorbers can be classified in two main groups [12] [13]. The first one, *graded interface and impedance matching*, achieve no reflection of the incident radiation by matching the surface impedance to the one of air while the radiation is dissipated inside the material. The second group, *resonant materials*, cancel the reflected radiation with destructive interferences. A fraction of the radiation is reflected at the interface while the transmitted fraction make a round trip in the material thanks to a metal backing plate. The thickness is taken so that the phase is shifted by π between the reflected wave and the transmitted wave. At the interface, both fractions recombine with a destructive interference and cancel out if the amplitude is equal.

Graded interface and impedance matching

When a EM radiation goes from one medium to another, a fraction is reflected at the interface, the other fraction is transmitted. The reflection coefficient, ρ , is proportional to the impedance mismatch between the two media. When the incident medium is vacuum, ρ is equal to

$$\rho = \frac{\eta - \eta_0}{\eta + \eta_0}. \tag{2.40}$$

No reflection, $\rho = 0$ occurs in two cases. When the impedance of the medium is equal to the impedance of vacuum, $\eta = \eta_0$, or when the relative permittivity and relative permeability of the medium are equal. Indeed in this case, ρ can be rewritten using equation 2.25 as

$$\rho = \frac{\frac{\eta}{\eta_0} - 1}{\frac{\eta}{\eta_0} + 1} = \frac{\sqrt{\frac{\mu_r}{\varepsilon_r}} - 1}{\sqrt{\frac{\mu_r}{\varepsilon_r}} + 1}. \tag{2.41}$$

Once the radiation has penetrated the medium, the magnitude of the EM field at a distance z from the interface is given by

$$E(z) = E_0 \, e^{-\gamma z} \tag{2.42}$$

where γ is the propagation constant taking the form

$$\gamma = \alpha + j\beta = j\omega\sqrt{\mu\epsilon} \tag{2.43}$$

where α is the attenuation constant and β the phase constant. With some manipulations of equation 2.43 [14], α can be expressed in terms of permittivity and permeability :

$$\alpha = \frac{\pi\sqrt{2\delta'_r}}{\lambda_0}\sqrt{\sqrt{1+tan^2\delta}-1}, \tag{2.44}$$

where

$$tan\delta = \frac{\delta''_r}{\delta'_r}, \tag{2.45}$$

$$\delta'_r = \mu'_r\epsilon'_r - \mu''_r\left(\epsilon''_r + \frac{\sigma}{\varepsilon_0\omega}\right), \tag{2.46}$$

$$\delta''_r = \mu'_r\left(\epsilon''_r + \frac{\sigma}{\varepsilon_0\omega}\right) + \mu''_r\epsilon'_r. \tag{2.47}$$

In order to dissipate a large amount of the EM radiation with a small thickness, α need to be maximized. This implies that μ'_r, μ''_r,ϵ'_r ,ϵ''_r and σ have to be large. In general, maximizing alpha is in conflict with minimizing the reflection.

The structured materials in Figure 2.18 have been developed to have a low input impedance while keeping a large absorption level.

Pyramidal Absorbers. Pyramidal absorbers are typically thick materials with pyramidal or cone structures extending perpendicular to the surface with a regularly spaced pattern. Pyramidal absorbers were developed so that the interface presents a gradual transition in impedance from air to that of the absorber. They are usually made of open-celled foam with a lossy coating.

Pyramidal absorbers provide high attenuation over wide frequency and angle ranges. Indeed, as highlighted in Figure 2.19, the geometry of the absorber makes that any reflection is trapped inside the structure until an almost complete absorption due to multi-reflection. These absorbers provide the best performances. The disadvantage of pyramidal absorbers is their large thickness and tendency to be fragile.

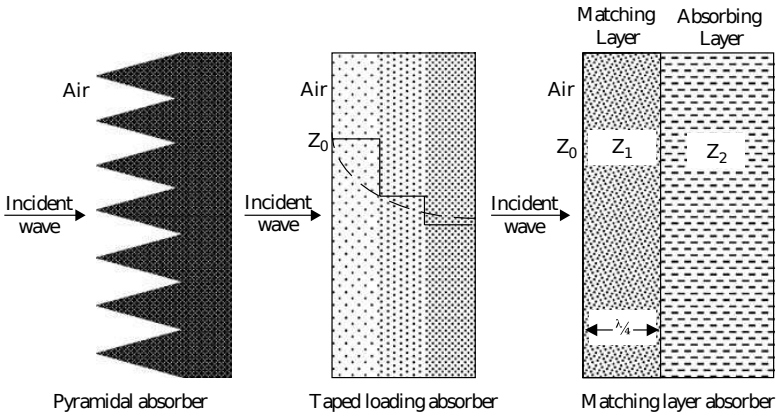

Figure 2.18: *From [12], Impedance matching absorber*

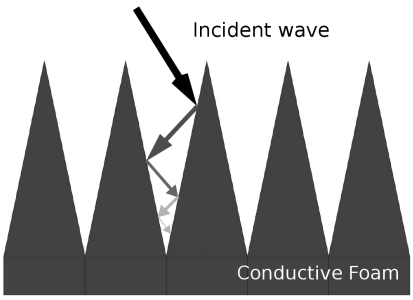

Figure 2.19: *Trapped reflections in pyramidal absorbers*

Tapered Loading Absorbers. Tapered absorbers are usually slabs of a material presenting, like the pyramidal absorber, a gradual modification of the impedance trough the thickness, see Figure 2.18. They can be manufactured by two approaches. In the first approach, a lossless open-celled foam is coated with a lossy coating which is gradually less concentrated or thinner close to the interface with the incident medium. The second approach is based on a multilayered material where each layer has an homogeneous impedance. The impedance increases if the layer is situated far from the incident surface.

The advantage of these materials is that they are thinner than the pyramidal absorbers. The disadvantage is that they have poorer performances and the gradient need to be optimized to the target wavelength.

Matching Layer Absorbers. A matching layer absorber allows to reduce the thickness required for the gradual transition materials. This absorber uses a transition layer between the incident and absorbing media. The transition layer has a thickness and an impedance values that are in-between the two impedances that has to be matched (i.e. the absorber and incident media). The idea is to have the effective impedance from the first and second layers equal to the impedance of the incident medium. This matching occurs when the thickness of the matching layer is one quarter of a wavelength of the radiation in the layer and $Z_1 = \sqrt{Z_0 Z_2}$.

The impedance matching occurs then only at the frequency that equals the electrical thickness. This makes the matching layer materials narrowband absorbers.

Resonant materials

In this class of absorbers the impedance is not matched between incident and absorbing media and the material is thin so that not all the power is dissipated inside the layer. Also resonant absorbers require to be placed on a ground plane or an electrically conductive plane. This arrangement results in reflection and transmission at the first interface. The transmitted wave travel trough the absorbing layer and is reflected thanks to a metallic backing plate. When it reaches the interface both waves recombine. If the electrical thickness of the absorbing layer is equal to $\lambda/4$ a destructive interference occurs and cancels if the amplitudes are equal. Due to their construction, resonant absorbers are extremely narrow band. Usually resonant absorbers are constructed from one of the three following structures: Dallenbach layer, Salisbury screen and Jaumann layer. All of them are shown in Figure 2.20. Circuit analog absorbers are a special case of the Salisbury screen and Jaumann layer.

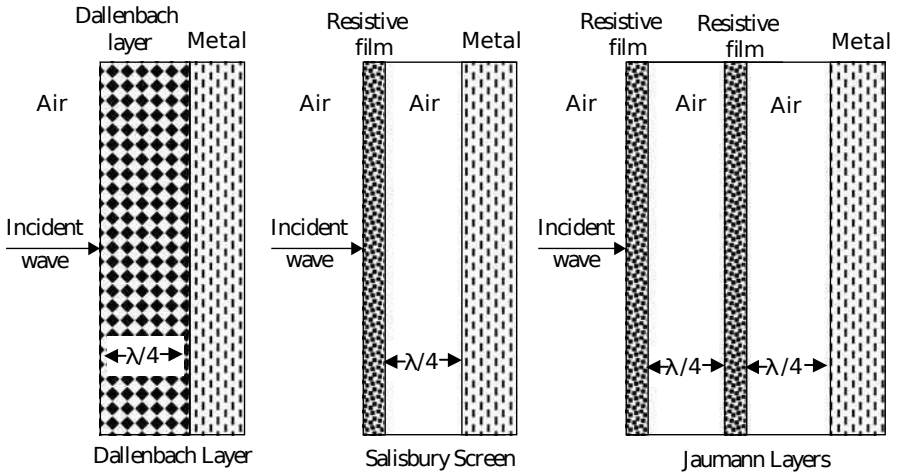

Figure 2.20: *From [12], resonant absorbers*

Dallenbach Layer Absorber. A Dallenbach layer is an homogeneous absorber layer of impedance Z_1 and thickness d_1 placed on a metallic plate. It relies on destructive interference of wave reflected from the first and second interface which totally cancel if the effective impedance of the layer, Z_L is equal to the impedance of the incident media Z_0. Z_L can be written as

$$Z_L = Z_1 \; tanh\gamma_1 \; d_1 = Z_0 \tag{2.48}$$

ε', ε'', μ', μ'' and d can be adjusted to achieve no reflection at a given frequency. Stacking several absorbing layers result in an increase of the operating frequency band.

Salisbury Screen and Jaumann Layers. A typical Salisbury screen is composed of a resistive sheet in front of a metallic plate separated by an air gap. The spacing will depend on the resonance frequency required. The resistive sheet needs to be as thin as possible with a resistance of $377\,\Omega$ matching that of free space. The Jaumann structure is a multi-layered Salisbury screen. Adding one or more layer increases the operating bandwidth but at the expense of the overall thickness.

The resistivity of the layer is high close to the incident medium and low near the ground plane.

Circuit analog absorber. Salisbury Screen and Jaumann Layers can be improved in terms of bandwidth and absorption effectivenesses by employing a sheet which is not purely resistive. Adding inductive or capacitive behaviour expands the design space. Such behaviour can be obtained by patterning the resistive sheet of the Salisbury screen as illustrated in Figure 2.21. A passband or band-stop layer can be obtained either with a resistive sheet periodically perforated with apertures, or an array of periodic resistive patches. Transmission coefficients of these structures are shown in Figure 2.22. Circuit analog absorbers with no intrinsic losses are called Frequency Selective Surfaces (FSS). Circuit analog absorbers are suitable to stealth curve surface like the leading edge of a wing [15].

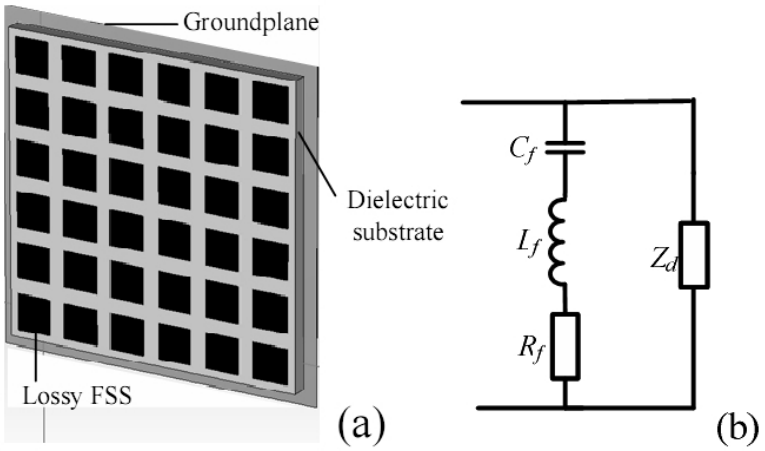

Figure 2.21: *From [16], three-dimensional sketch (a) and equivalent circuit (b) of the conventional circuit analog absorber.*

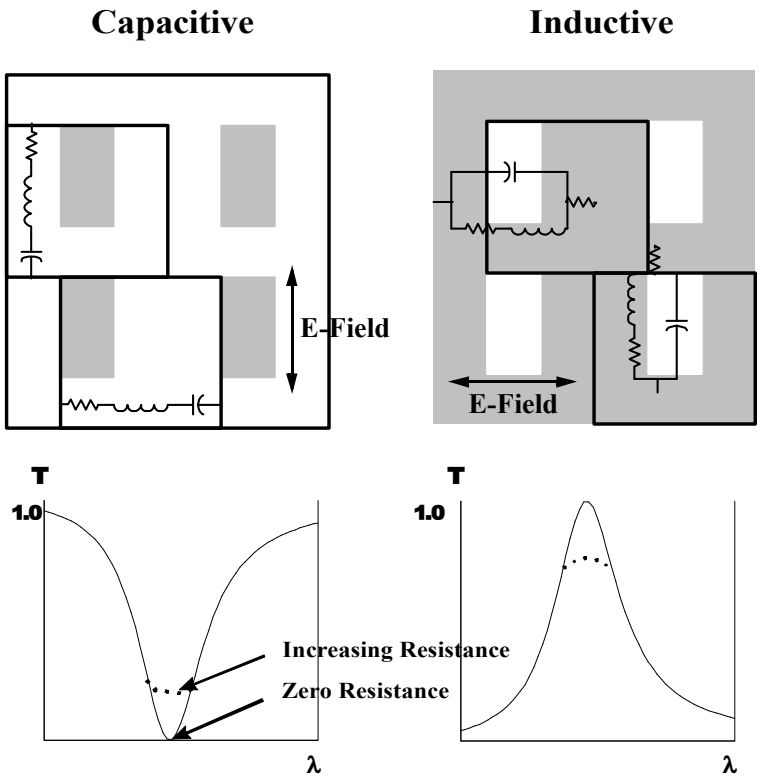

Figure 2.22: *From [17], capacitive and inductive FSSs with corresponding equivalent circuits and their transmission profiles. Metallic parts are in gray.*

2.2.4 Thin and flexible multilayer composite for EM absorption

Danlée *et al.* [18] have developed a multilayer arrangement of polymer based nanocomposites able to absorb microwave radiation over a broad frequency range while keeping the thickness of the structure around a few millimetres. Well designed stackings achieve frequency selective filtering.

The structure is built upon alternating films of dielectric polymer and conductive layers. In order to improve the absorption, the conductive layer are stacked in a precise gradient of conductivity. Conductive layer are either made of polycarbonate film melt-blended with carbon nanotubes (CNT) or by the deposition of a thin CNT coating on a polycarbonate film. The deposition is performed by the projection of a CNT waterborne ink on the polycarbonate surface previously plasma treated to ensure a good wetting of the ink and therefore a high resulting conductivity of the dry coating. Such structures are easy to make, modular, and open to new possibilities in the area of microwave management (broadband shielding by absorption or frequency-selective filtering, also called bandgap control)

Figure 2.23 compares the absorption of a multilayer CNT-PC melt-blended composite and a CNT coated multilayer.

In Figure 2.23a, the structure consists of 13 conductive layers whose conductivity increases gradually from 6 to 290 $\mathrm{S{\cdot}m^{-1}}$, each with a thickness of about 175 µm. The range of conductivity is achieved by varying the CNT content from 0.25wt% to 5wt%. The 14 dielectric PC layers are 110 µm thick each. Because of the conductivity gradient, the absorption index in Figure 2.23a depends on the direction of the measurement. The absorption is maximum, thanks to a low reflection coefficient, if the wave propagates from low CNT content to high CNT content (corresponding to a propagation from port 1 to port 2). The level of absorption is higher than 80% over the frequency spectrum for a total thickness of the sample equal to 4.90 mm.

The multilayer based on CNT-ink coated layers shows a similar absorption index despite being twice thinner (see Figure 2.23b). The transmis-

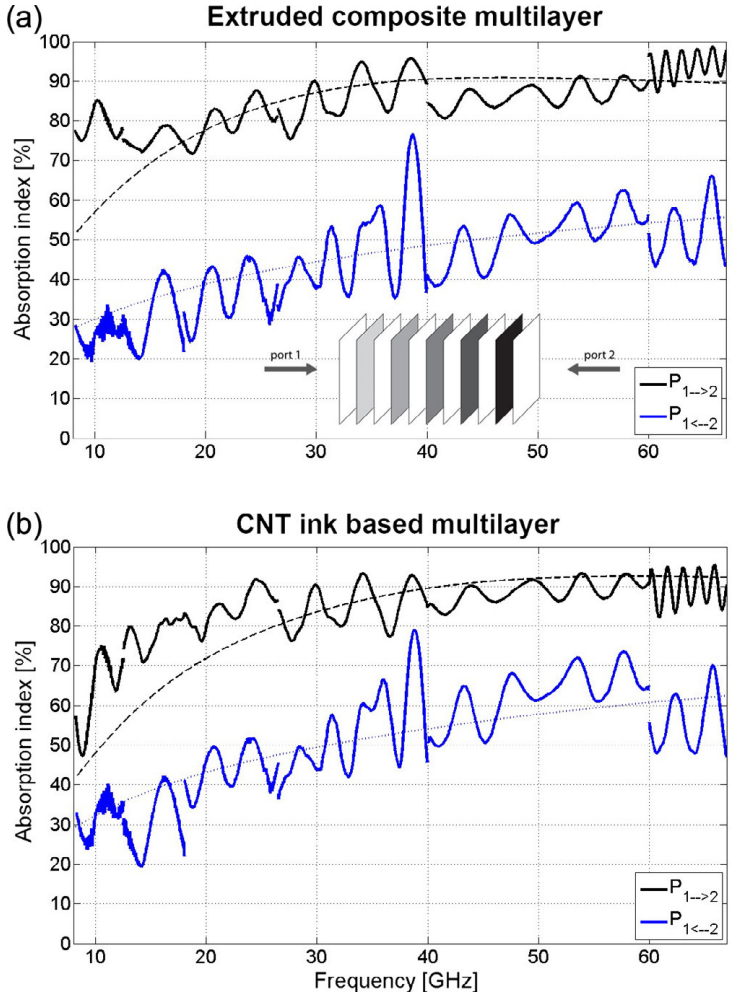

Figure 2.23: *From [18], (a) Absorption index of a multilayer with 13 CNT-PC composite layers and 14 dielectric layers vs frequency. (b) Absorption index of the multilayer at 9 AquaCyl^{TM}coats sandwiched between 10 dielectric layers. Measurements (full lines) are fitted with simulations (dotted lines).*

sion is higher for this configuration but this is compensated by a lower reflection because the CNT coating is significantly thinner, as compared to a blended composite. A full analysis of this compensation effect requires the use of S-parameters (not shown for the sake of brevity). The ink based gradient nevertheless keeps the advantage over blended composites, since its overall thickness is only 2.56 mm.

2.2.5 Hybrid lattice-foam EM absorber in literature

Multifunctional EM absorbers based on foam filled honeycomb have been, to my knowledge, mentioned only by one research group in the literature. Fan *et al.* [19] have studied a panel, represented in Figure 2.24, consisting of an interlocking kagome lattice made of glass or carbon fiber reinforced polymer filled with a polymer foam loaded with a concentration gradient of carbon black. The lattice is built up from composite struts with notches forming a kagome lattice structure. Foam is then cut to dimension and manually inserted in the lattice cell.

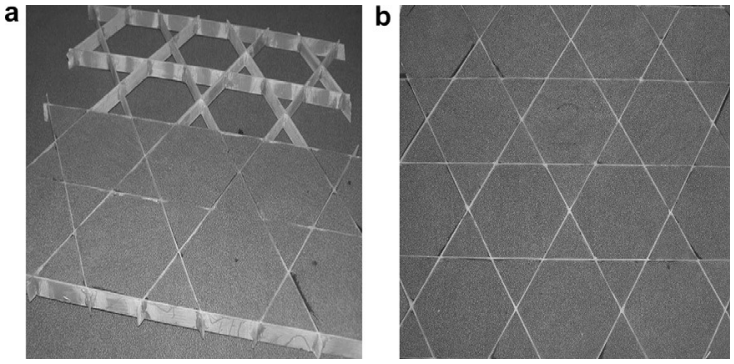

Figure 2.24: *From [19], samples of absorbent grids: (a) manufacturing; and (b) GFRC grids.*

Despite a high level of absorption for panel of 18 and 20 mm thick panel, Figure 2.25 their approach suffers from several drawbacks. There is no analytical model to predict the absorption level of such a panel as a function of thickness, lattice size and EM properties of the foam. The

manufacturing process involves numerous steps and is therefore not suitable for large scale production.

Panels	Materials	Thickness (mm)	$D_1/2$(mm)	Dimension of panels (mm)
B	Foams	20	No grids	180 · 180
E	GFRC + foams	20	20	300 · 300
F	GFRC + foams	20	40	300 · 300
G	CFRC + foams	18	20	180 · 180

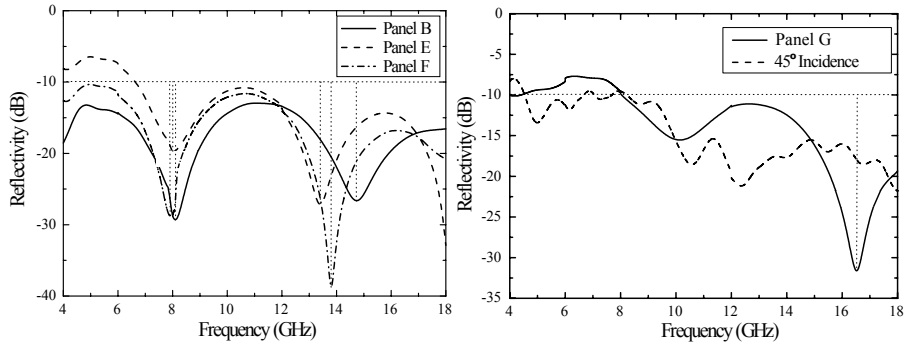

Figure 2.25: *From [19], reflectivity curves of panels.*

The objectives of this thesis is to go beyond the state of the art on absorbers by proposing a multifunctional material with high EM absorption capacity suitable to large scale production, and to develop an analytical model for the EM absorption which will allow the determination of the optimal design at low computational cost.

Chapter 3

Materials and process

This class of hybrids involves a wide range of parameters. Even though models and optimization procedures have been set up to design the best solution with respect to a list of requirements selecting the best processing routes as a function of the application and of the expected characteristics of the hybrids remains an open question and could be the limiting factor in the development of this class of hybrids, as for many other hybrid systems [20] [21].

The goal of this Chapter is to present and critically discuss the different processing strategies that have been attempted and assessed for the fabrication of the hybrids in order to provide constraints for the optimization as well as guidelines for the possible upscaling. The Chapter is divided in two parts. In the first part, the reinforcement, the polymer matrix and the foaming method are selected and the compounding method and honeycomb filling process are set-up based on the materials selected. In the second part, the filler dispersion and the foam microstructure are analysed. The overall quality of the fabricated samples is verified. Finally, the EM absorption performance is studied as a function of the different processing routes.

3.1 Selection of the materials and processing methods

Figure 3.1 shows the different steps of the process which are described in this section.

1. The fillers, polymer matrix, foaming agent, honeycomb and face sheets are selected based on the expected set of elementary properties (electrical conductivity, permittivity, porosity, strength). The choice is guided using different electromagnetic and mechanical models presented in several references [22] [23] [24].

2. Compounding is performed in melt phase.

3. Foaming is performed either *ex-situ* followed by insertion within the honeycomb or *in-situ* in the honeycomb (HC).

4. The face sheet are finally bonded to the core hybrid material.

3.1.1 Selection of polymer matrix and fillers

Different kinds of fillers commercially available can be used to increase the electrical conductivity of polymers at microwave frequency. They can be categorized based on their aspect ratio as spherical particles involving carbon black or metallic powder, layered platelets involving graphene and nanoclays, and elongated fibers involving carbon nanotubes (CNT) or metallic nanowires. This last category exhibits the highest aspect ratio, enabling the establishment of a percolating network at a low amount of fillers [25] [22]. Saib *et al.* [1] have indeed shown that the use of CNT compared to carbon black decreases from 20 down to 0.35 wt% the amount of filler needed to obtain a conductivity of 1 S/m at around 20 GHz. The decreasing price of the CNT combined to the low amount that is needed makes this choice competitive. More precisely, multiwalled carbon nanotubes NC 7000, 90% from Nanocyl have been selected for all our investigations.

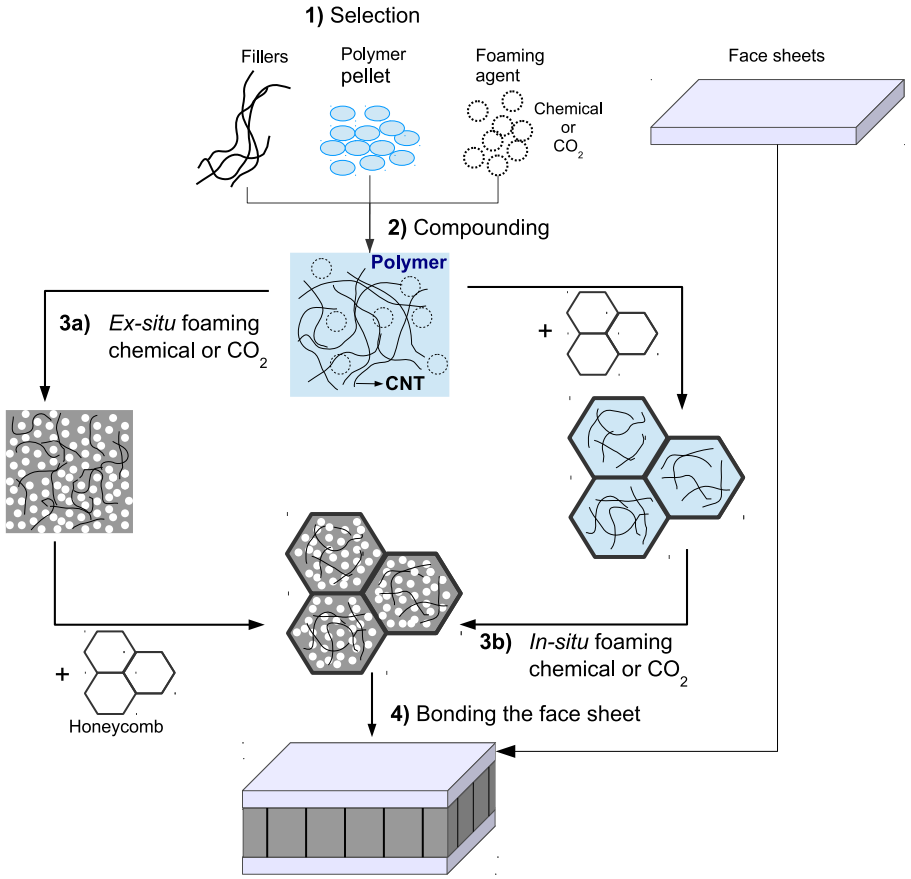

Figure 3.1: *Schematic view of the key steps of the two main processing routes : ex situ process (i.e. mechanical insertion of foamed compound into honeycomb), or in situ process (i.e. foaming of the compound inside the honeycomb cells)*

Among the wide variety of available matrices, the choice of the polymer was driven by the potential for integration into large-scale industrial processes, by the thermo-mechanical performances, by the known easiness and effectiveness of the nanofillers dispersion, and by the foaming ability. Taking into account all the previous constraints, polyurethane (PU) and polycarbonate (PC) have been selected. Both are widely used in

the industry. PU is mostly selected for his superior abrasion resistance, flexibility, and shear resistance. PC has high shock and temperature resistance as well as a relatively high mechanical stiffness compared to other polymers. CNT are easily dispersed by melt mixing in these two matrices [26] [27] [28] [29]. Each matrix is available as a nanocomposite masterbatch, facilitating its integration in an existing process installation. The specific grades of polymer used here are thermoplastic PU *Desmopan 2590 A* and PC *Makrolon 2805*, both produced by Bayer.

3.1.2 Selection of the foaming method

Several methods exist in the literature to foam a CNT filled polymer composite. The first method is called "casting and leaching" [30] (involving therefore solvent casting and particle leaching) which starts by mixing the polymer, organic solvent, CNT and soluble solid particles. In the next step, the organic solvent is evaporated. And finally, the particles are leached. Foams can also be produced by "freeze-drying" [31], also known as lyophilisation or cryodessication. In this process a solution is prepared by dissolving the nanocomposite in a solvent. This solution is then freezed and subject to vacuum conditions so that the solvent can sublimate to leave pores in the polymer. The HIPEs polymer [32] (High internal phase emulsions) is generated by the polymerization of the monomer in the external continuous phase of an emulsion followed by the removal of the internal phase which possesses a high volume ratio (74%). This strategy yields macroporous polymer with open-cell structure. In the particular case of a PU matrix, nanocomposite foams can be processed through polymerization in the presence of water which reacts with the isocyanate groups to release CO_2 molecules. This induces the expansion of the material [33].

In the considered case, one of the easiest method to foam nanocomposite is through the use of a blowing agent. Blowing agents can be classified into two main groups:(1) physical foaming agents or (2) chemical foaming agents (CFA). Physical blowing agents are often soluble additives which can trigger the formation of foams by decompression or action of heat. In comparison to other physical blowing agents, CO_2 is non-toxic,

non-flammable, inexpensive, inert to polymers, with an acceptable solubility. The supercritical carbon dioxide ($scCO_2$) is a state where both temperature and pressure are above their critical values (Pc=73.8 bar and Tc=31.1 °C). Chemical blowing agents are substances which generate gases by chemical reaction or decomposition at processing temperatures and then trigger the foaming process. A review of the most typical chemical foaming agents is provided in [34]. CFA can be either endothermic or exothermic. Endothermic foaming agents have several advantages over exothermic agents. They stabilize the temperature during the process, help to avoid local over-heating and shorten cooling cycle times. Gas is released at low pressure which results in a finer microstructure, and is mostly composed of CO_2. But the use of a blowing agent limits the amount of CNT that can be practically used. Indeed, if the amount of fillers increases, the viscosity increases accordingly. With a too high viscosity, the gas pressure released by the blowing agent is not sufficient to allow the expansion of the foam cell.

One chemical foaming agent and one physical foaming agent have been compared in this research. The selected chemical foaming agent is the Hydrocerol HK40B from Clariant. Supercritical CO_2 was selected, motivated by the multiple advantages over other physical foaming agents.

3.1.3 Compounding

A good dispersion without breakage of the filler in the matrix is mandatory to produce the percolating network needed to obtain a conductivity around 1 S/m. Thomassin *et al.* [22] report several dispersion methods from the literature. The most effective methods are solvent casting, polymer emulsions, *in-situ* polymerization and polymerization-precipitation. But all these methods involve the presence of a solvent in order to disperse the CNT and this solvent must be removed by drying in order to recover the nanocomposite material. This step is very expensive and prevents the upscaling into an industrial unit. Melt mixing is another dispersion method where the CNT are disentangled thanks to high shear forces. Unfortunately, the high shear force also breaks the nanotubes, reducing somewhat their aspect ratio and the effectiveness

of the conductive network. But owing to a lower cost and industrial upscaling potential, this second dispersion method was selected in the present work.

Compounding method 1: for chemical foaming

Multiwalled carbon nanotubes (CNT) (NC 7000, 90%, Nanocyl) and chemical foaming agent (CFA) (Hydrocerol HK40B, Clariant) were dispersed in the PU (PU Desmopan 2590 A, Bayer) or PC matrix (PC Makrolon 2805, Bayer) using a co-rotating twin-screw minicompounder (DSM Xplore Microcompounder $15cm^3$) with a bypass allowing continuous recycling of the material at the head of the mixing chamber. The processing conditions were the following: the temperature was set to 180 °C for PU and 270 °C for PC. The compounds were mixed for 3 min at 100 rpm.

Compounding method 2: for supercritical CO_2 foaming

Either the polycarbonate or the polyurethane were melt blended with the desired amount of CNT in a counter-rotating twin-screw static mixer (Brabender) at 180 °C for the PU or at 250 °C for the PC matrix for 5 min at 60 rpm. The nanocomposite was pressed for 5 min at the processing temperature in order to produce ready-to-foam sheets.

3.1.4 Foaming and honeycomb filling

Selection of the honeycomb

Honeycomb are usually made of aramid or glass fiber reinforced polymer or aluminium. In order to generate a waveguide effect, the surfaces of the cells must be metallic. Depending on the required thermal conductivity of the core, aluminium will be selected for its high thermal conductivity. Other options involves metallized aramid or glass fiber reinforced epoxy for their low thermal conductivity. Cell sizes ranging from 2 to 11 mm have been used in this research. Once filled

with the nanocomposite, their cutoff frequency is around 40 GHz and 5 GHz, respectively. The honeycombs used in this research, (see Figure 3.10), are made of aluminium 5052 referenced as CRIII-1/8-5052-.002-8.1, CRIII-3/8-5052-.004-5.4, CRIII-1/2-5052-.004-3.9, CRIII-3/4-5052-.0025-1.8 from Hexcel or aluminium 3003 referenced as ECM 6.4-82 from EURO-COMPOSITE.

Literature examples of foam filled HC

A few processes have been described in the literature to fill a honeycomb with a polymeric foam. If the cell size is large enough, pieces of foam can be cut at the dimension of the cell and then inserted inside [35]. Syntactic foam may also be used to fill a honeycomb [36]. Another method, is to mechanically press the sheet foam inside the honeycomb. This method has the disadvantage to be restricted to a limited range of density and matrices and to produce lots of dust that may interfere with the bonding of the face. The other route is to pour a liquid or solid state unfoamed material and then trigger the foaming. But, using this last filling process may result in uneven density distribution from cell to cell [37]. PU has been widely used in a liquid state to fill honeycombs [36] [38] [2].

Two processing routes have been studied. The first one is the *ex-situ* method which is inspired from the mechanical insertion method. The second processing route, called *in-situ*, consists in foaming the compound directly inside the honeycomb.

Ex-situ foaming and mechanical insertion

The *ex-situ* process is composed of two steps: first a polymer plate is foamed, then, in a second step, it is mechanically inserted in the honeycomb. To increase the range of foam conditions (density, mechanical properties) that can be successfully inserted without fragmentation or damage of the constituent, the honeycomb is heated near the processing temperature of the polymer. This will melt the polymer locally and allow the honeycomb to smoothly penetrate the foam.

Chemical foaming method is realized by adding 7.5 wt% of chemical foaming agent (CFA) (Hydrocerol HK40B, Clariant) during melt mixing. The nanocomposite powder was poured in a mould and compressed using a 15 tons Fontijne press. The amount of powder poured into the mould was calculated to reach a foam density of $0.55 g/cm^3$. Foaming lasted for 2 min at a temperature set at 280 °C which is well above the decomposition temperature of the foaming agent (230 °C). Foam thicknesses around 10 mm have been obtained without degradation of the polymer or collapse of the foam.

The foaming with supercritical CO_2 is a two step process. In the first step, the composite sheets were introduced in a vessel and pressurized with CO_2 (99.5%, Air Liquide, Belgium). In the second step, the saturated sheets were quickly transferred in a hot press at 120 °C for PU and at 190 °C for PC during 190 s to induce foaming. The foams were finally quenched in an ice/water bath to stabilize (freeze) the structure. Foaming PC by means of $ScCO_2$ is not straightforward. The operating conditions to successfully foam the PC/CNT composite are reported in reference [39]. The operating conditions for impregnation of CO_2 in the two polymer matrices are the following: for the PU matrix, the vessel was at 40 °C at 250 bar (ISCO pump) for 24 h. For PC matrix, the conditions were 100 °C and 75 bar during 7 h.

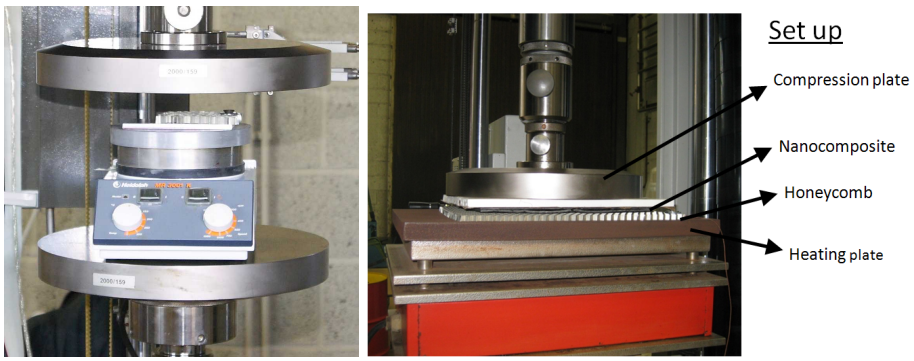

Figure 3.2: *Insertion set up*

The set up for the insertion of the foam in the honeycomb is shown in Figure 3.2 and consists of a mechanical testing machine (Zwick 50kN)

set up in a compression mode. A regulated heating plate is introduced between the compression plates to heat the honeycomb to the desired temperature, 140 °C up to 160 °C for PU and 180 °C up to 240 °C for PC. The foam sheet is then sticked with double-sided adhesive tape on the upper plate and inserted in the honeycomb. The insertion speed of the foam was set between 1 and 10 mm·min^{-1}.

In situ foaming

Several honeycomb sizes and thicknesses have been tested with the *in-situ* process. They are all shown later in Figure 3.10.

The foaming of the nanocomposite inside the honeycomb follows exactly the same process as for the foam sheet. The only difference is that a honeycomb is introduced in the mould before pouring the nanocomposite powder. The key is to pour the compound evenly in the honeycomb cells. The processing conditions are 2 min at a temperature set point of 280 °C, which is identical to the *ex situ* foaming.

The *in situ* foaming with $scCO_2$ required first to insert the sheet of composite in the honeycomb. This operation is made in an oven at 220 °C or 240 °C for PU and PC respectively. The insertion is made under a dead-weight put on top of the HC.

3.1.5 Sandwich production

In order to increase the stiffness and impact resistance of the panel, the hybrid is used as the core of a sandwich panel. To allow the sandwich panel to absorb the incoming EM radiation, the face sheets added on the two sides of the hybrid need to be transparent to EM radiations. This translates in terms of material properties into a dielectric constant close to unity and an electrical conductivity near zero [23]. Combining this requirement with a high stiffness over density ratio led to the selection of faces sheet made of glass fiber reinforced polymers. In some cases where the wave must to or can be reflected on one side of the material, the backing face sheet can be made of an electrically conductive material,

like a metal or a carbon fiber reinforced polymer. We selected fiber reinforced E-glass/Epoxy composite panel (SI403240, Goodfellow) for both side of the sandwich panel.

The face sheets can be bonded either by co-curing prepreg of fiber reinforced polymer on the core or through the use of an adhesive [7]. Compared to bonding open HC as in many applications of sandwich components where adequate bonding conditions are not straightforward to attain due to the small effective bonding area, the bonding is here much simplified because it is performed on a continuous surface. The bonding was made by a bi-components epoxy adhesive (3M^{TM}DP 460).

3.1.6 Summary

All the combinations in terms of polymer matrix, foaming method, insertion in the honeycomb (*ex situ* or *in situ*) and resulting hybrid configuration (with or without face sheets) are summarized in Table 3.1. Not all the combinations involved in Table 3.1 have been tested in this research. Only the overlined conditions have been addressed which allows looking at least at all key options two by two.

	in-situ foaming		*ex-situ* foaming	
Supercritical CO_2	PC	PU	PC	PU
	Sandwich	Sandwich	Sandwich	Sandwich
Chemical foaming agent	PC	PU	PC	PU
	Sandwich	Sandwich	Sandwich	Sandwich

Table 3.1: *Overview of the experimental set of conditions, with overlining on the one effectively tested.*

3.2 Results and discussion

3.2.1 Quality of composite and foam microstructures

The quality of CNT dispersion in both polymer matrices before foaming is illustrated in Figure 3.3. The CNT are properly dispersed with no

remaining aggregation effects. The foaming does not degrade the dispersion quality of CNT. In reference [40], it was shown that the percolation was even more easily attained in foam materials.

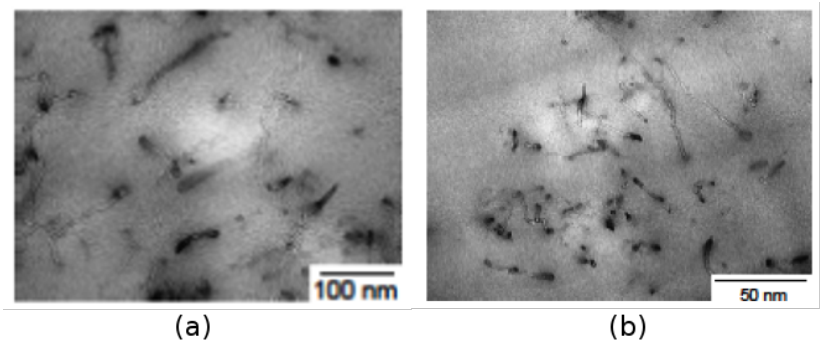

Figure 3.3: *TEM micrography of the dispersion of 1wt% of CNT in (a) PU and (b) PC*

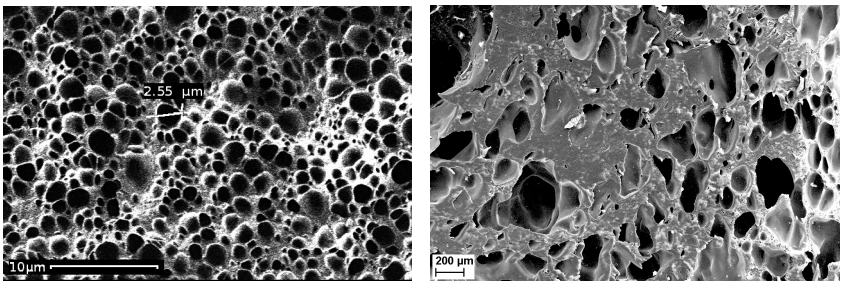

(a) $scCO_2$ foam, PU/2wt% CNT (b) Chemically foamed PC/1wt% CNT

Figure 3.4: *SEM micrography of the microstructure of nanocomposite foams*

Typical microstructures of a PU nanocomposite foamed via supercritical CO_2 are shown in Figure 3.4(a). The foam exhibits closed-cells of diameter ranging from 1 to 5 µm with rather regular distribution. The cell size resulting from chemical foaming is larger than with CO_2, ranging from 100 to 500 µm as depicted in Figure 3.4(b). This larger length scale is not impacting EM absorption since the cell size is at least one

order of magnitude smaller than the incoming wavelength. Indeed, the design operating frequency range for the absorption is from 5 to 40 GHz corresponding to wavelengths approximately from 5 cm down to 5 mm. The presence of very large cells at the tail of the distribution could potentially affect the mechanical response.

3.2.2 Overall reliability and dimensional control of the hybrid core

In this section, the *ex-situ* foaming followed by mechanical insertion is compared to the *in-situ* method.

Mechanical insertion

Figure 3.5 shows the results of the insertion in a 7 mm thick honeycomb

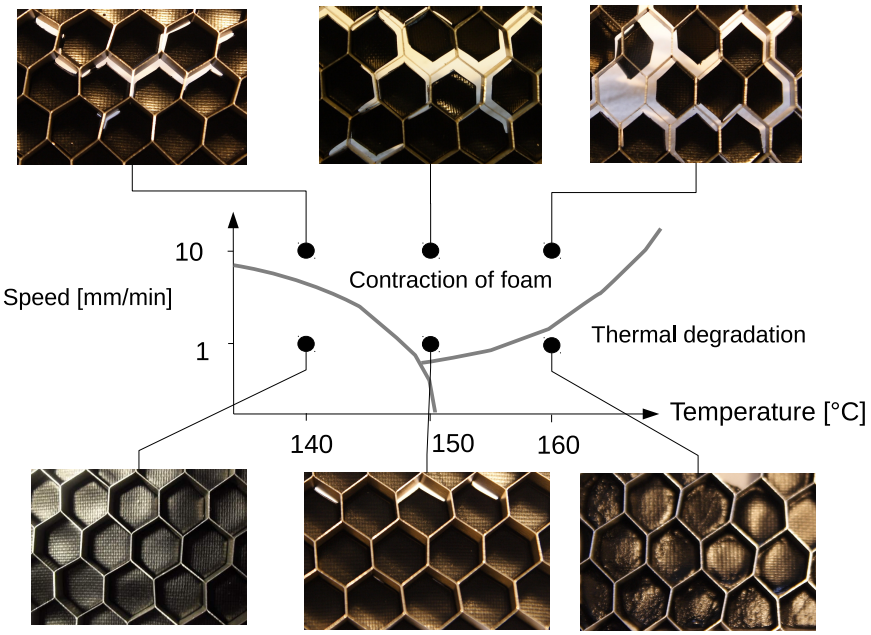

Figure 3.5: *Process map for $scCO_2$ PU foams mechanically inserted in a honeycomb.*

with cell size of 5 mm in term of speed and temperature. The quality of the hybrid resulting from insertion of a PU/2wt% CNT nanocomposite foamed with supercritical CO_2 very much depends on the speed of insertion and on the temperature of the hot plate. Each set of parameters has been tested three times. Several types of defects can be observed depending on the insertion conditions. If the speed of insertion is higher or equal to 10 mm·min^{-1}, the foam retracts during cooling and some evidences of tearing of the foam can be seen near the honeycomb walls. This phenomenon gets worse if the temperature increases, to the point that parts of the foam fall out off the honeycomb. If the speed is kept at 1 mm·min^{-1} but the temperature increased, the foam facing the hot plate starts being degraded due to the longer time of the insertion at high temperature, see Figure 3.6. The best conditions are for a speed of 1 mm·min^{-1} and a temperature of 140 °C. The process map corresponding to this insertion mechanism is shown in Figure 3.5.

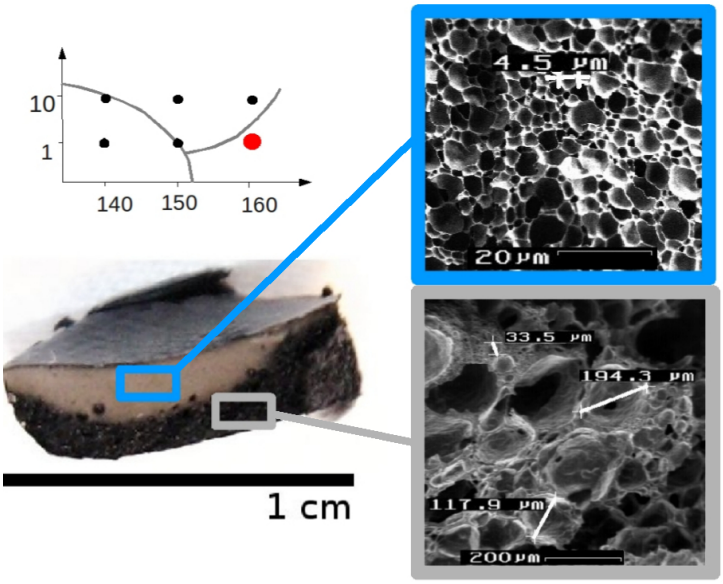

Figure 3.6: *Insertion of $scCO_2$ foamed PU at 160°C and 1 mm·min^{-1}, with above the microstructure of the foam and below the thermally affected zone*

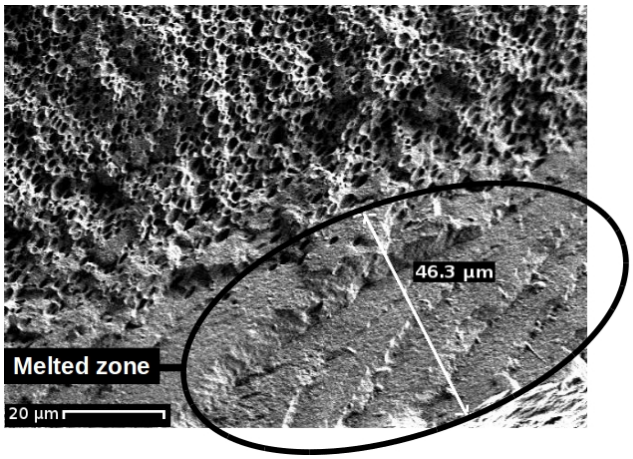

Figure 3.7: *Melted zone near the honeycomb after insertion of a PU ScCO2 foam at 140°C and 1 mm·min^{-1}*

Figure 3.6 reveals that the microstructure of the CO_2 foamed polymer inserted at 160 °C and 1 mm·min^{-1} was altered. Indeed, the insertion temperature was close to the polymer processing temperature and the insertion speed was too slow. This leads to the coalescence of the cells due to inflation of gas in the cell and the melting of the cell walls, resulting in cell size in the range of 200 µm. Figure 3.7 shows the foam in contact with the cell wall. In this region, a solid skin is formed. The thickness is around 50 µm. Compared to the cell size and the wavelength involved, this solid layer will have no influence on the EM behaviour of the hybrid. More details about the degradations observed during mechanical insertion of foam are given in appendix A.

The insertion inside a 7 mm thick honeycomb of a 7 mm thick PC foamed with a CFA has also been studied to check whether the larger foam cell size and quality of the foam affect the mechanical insertion. Figure 3.8 shows the results. On the cold side, the foam is flat but a thin layer of foam is not inserted. Some degradation of the foam is observed on the hot side. On this side, the foam in the honeycomb cell gets an hemispherical shape which results from the melting of the foam and the friction force between the wall and the foam. A cross section view of the cell is shown in Figure 3.9 reveals a degradation of the microstructure.

The foam has melted and forms a more dense layer on this side. As a result, the thickness is reduced and the foam does not entirely fill the honeycomb. A degradation of the EM properties can also be expected. Indeed, the thickness of the dense layer is larger than 1 mm which is close to the EM wavelength.

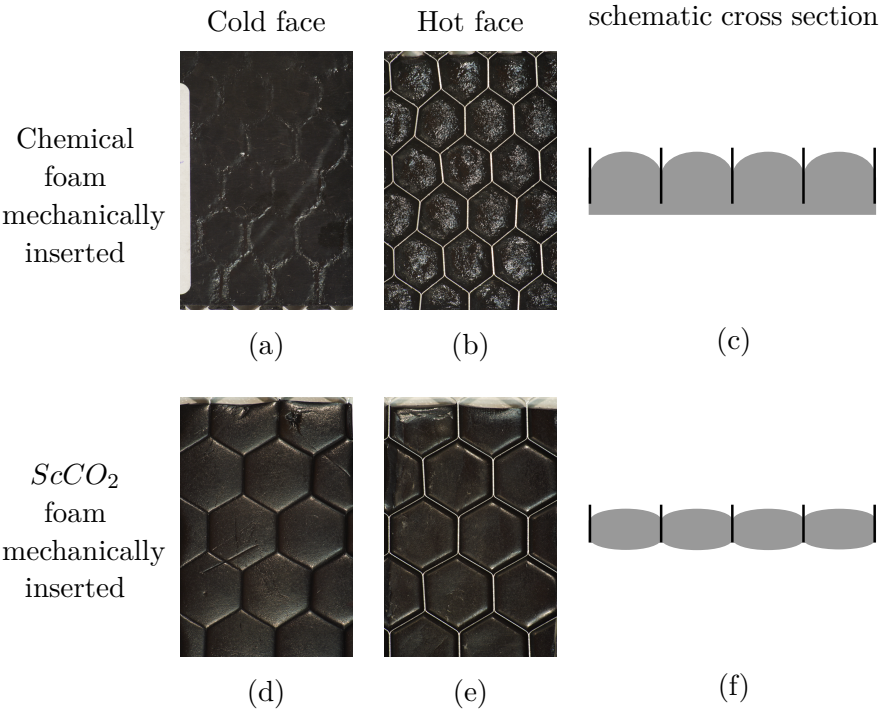

Figure 3.8: *(a b c): PC nanocomposite chemically foamed after insertion at* $220°C$ *and* $2.5\,mm{\cdot}min^{-1}$*. (d e f): PU nanocomposite* $scCO_2$ *foamed after insertion at* $140°C$ *and* $1\,mm{\cdot}min^{-1}$

As it can be seen in Figure 3.8, the insertion of a 2 mm thick PU foamed with $scCO_2$ inside a honeycomb with a thickness of 3 mm exhibits some defects. The foam slightly expands above the honeycomb on the cold side. This comes from the very elastic behaviour of CO_2 PU foam. During the insertion of the honeycomb, the foam is compressed on the cold plate. At the end of the insertion, the foam returns to its original

shape and slightly expands outside the HC. On hot plate side, there is an empty space between the honeycomb cell wall and the foam. If the insertion condition is not optimized other defects can occur, see Figure 3.5.

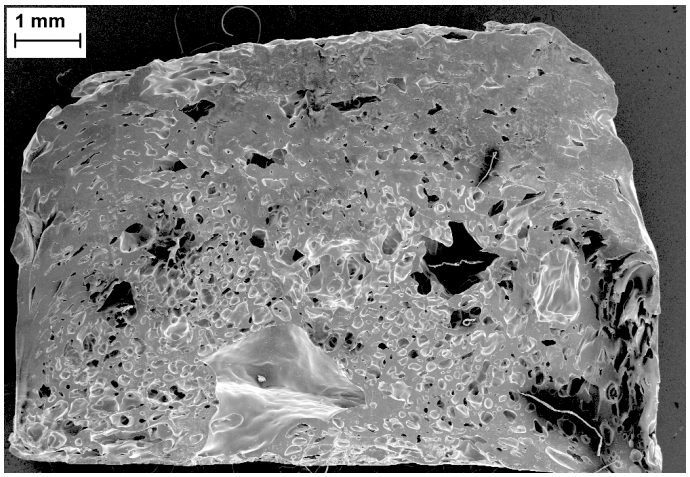

Figure 3.9: *SEM micrography of a HC cell cross section of an inserted chemically foamed PC at 240°C and 1 mm·min^{-1}*

In-situ foaming

Figure 3.10 shows representative samples of PC/CNT chemically foamed inside honeycombs of various cell sizes and heights. No open space between the aluminum cell wall and the foam is observed with this process. Also there is no surface defect and no extra care is required to generate a flat surface. The overall geometry appears thus much more planar and finished than with mechanical insertion.

Figure 3.11 and 3.12 show hybrids with a thickness of 6 mm produced by *in situ* supercritical CO_2 foaming for a PC and PU matrix respectively: the honeycomb did not resist to the stress induced by the foaming process with large voids appearing in the middle of some of the honeycomb cells.

X=	2 mm	3 mm	5 mm	7 mm	11 mm
					
t=	7 mm 2 mm	3 mm	7 mm	3 mm	4 mm
w=	50μm	60μm	100μm 60μm	100μm	60μm

Figure 3.10: *in situ foaming by CFA for PC/1wt% matrix inside several HC sizes and heights*

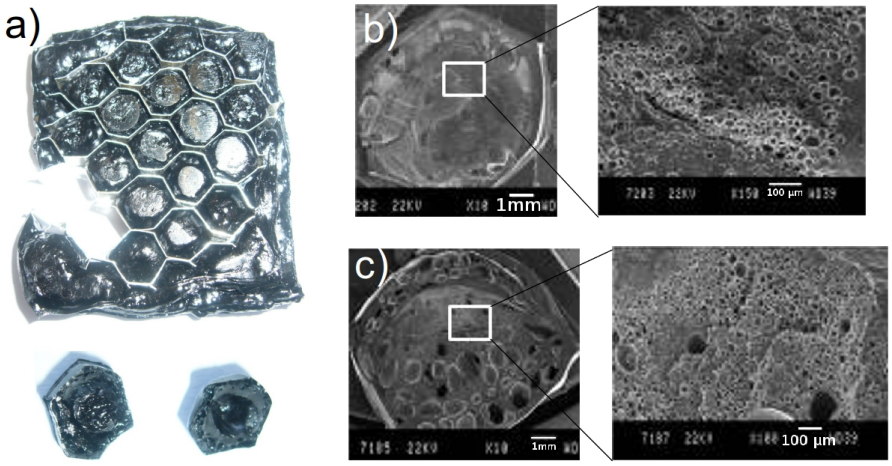

Figure 3.11: *in-situ scCO2 foaming of PC based matrix, a) general view, b) in-plane cross section of a cell, c) transverse cross section of a 6 mm thick honeycomb cell.*

Figure 3.13 shows that a reduction of the height of the honeycomb down to 3 mm combined with constraining the external honeycomb boundary using the unfoamed nanocomposite leads to uncracked samples and ho-

mogeneous foam. But the large internal stress gradients during foaming generate significant distortions of the honeycomb.

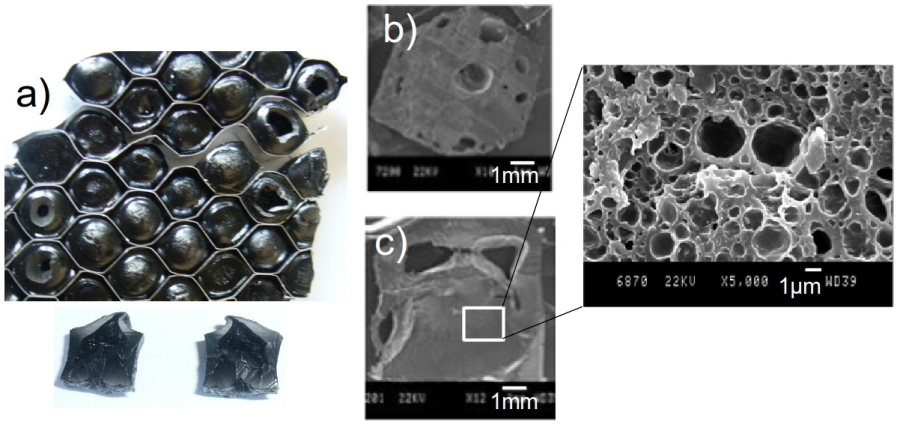

Figure 3.12: *in situ scCO2 foaming of PU based matrix, a) general view, b) in-plane cross section of a cell, c) transverse cross section of a 6 mm thick honeycomb cell.*

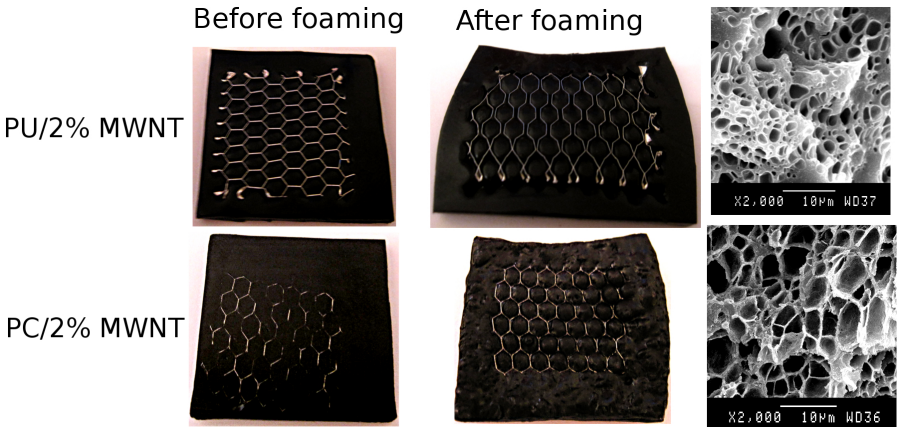

Figure 3.13: *in situ scCO2 foaming of PU based matrix within 3 mm thick HC at the top and PC based matrix at the bottom.*

3.2.3 Demonstration of electromagnetic absorption performance

The relative complex permittivity, ε_r^* and permeability, μ_r^* of a material are the two material parameters needed in order to fully describe the absorption response of this kind of material under an EM field. Because all the constituents of the hybrid are non magnetic, the permeability μ_r^* is real and equal to unity. The relative complex permittivity, ε_r^* is expressed as [23]

$$\varepsilon_r^* = \varepsilon_r - \frac{j\sigma}{\varepsilon_0 \omega} \tag{3.1}$$

with ε_0 the permittivity of vacuum, ε_r the dielectric constant, σ the electrical conductivity, and ω the radian frequency equal to $\omega = 2\pi f$ where f is the frequency. In order to maximize the EM absorption, the dielectric constant of the foam needs to be as close as possible to 1 and the electrical conductivity must be in the range of 1 to 5 S/m [41].

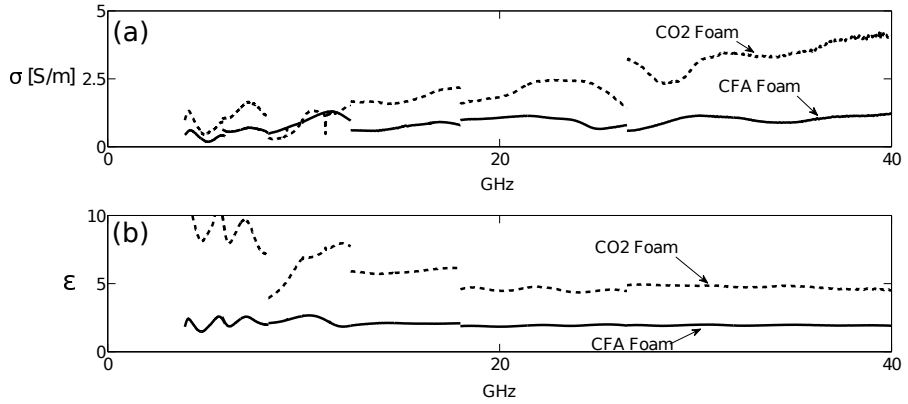

Figure 3.14: *variation as function of the frequency of (a) electrical conductivity and (b) dielectric constant for PU foam filled with 1wt% of CNT. Dash line is a foam of 0.36 g·cm^{-3} foamed with supercritical CO_2 and solid line is a foam of 0.48 g·cm^{-3} foamed with chemical foaming agent.*

The EM characterization of PU with 1% of CNT foamed with scCO_2 or CFA is shown in Figure 3.14. The density of the foam is 0.36 g·cm^{-3}

for scCO_2 foaming and $0.48\,\mathrm{g{\cdot}cm^{-3}}$ for chemical foaming. Both foams exhibit adequate EM response. But, keeping the polymer matrix and the amount of CNT identical, a lower foam density should lead to a lower dielectric constant and a lower electrical conductivity. Despite a lower density, the foams produced by supercritical CO_2 involve an higher dielectric constant and a better conductivity. This behaviour is probably due to differences in the foam expansion and microstructure. Indeed, in the case of scCO_2 foaming, the foam is formed from a solid plate which expands to reach its final attainable density. With chemical foaming, the foam is formed from a compressed powder in a mould with almost no expansion. Furthermore, the cell wall thickness in the CO_2 route is in the 500 nm range as illustrated in Figure 3.6 and Figure 3.7. The large expansion means that the CNT in the matrix are stretched within the cell walls of the CO_2 foam. This stretch increases the effectiveness of the resulting percolating network and leads to an higher conductivity and dielectric constant [40] [42].

The fraction of EM power absorbed by a slab of material, denoted hereby absorption index A, is defined by the ratio between the absorbed power P_{abs} and the incident power P_{in}, expressed as:

$$A = \frac{P_{abs}}{P_{in}} = 1 - \frac{P_{ref}}{P_{in}} - \frac{P_{out}}{P_{in}} \tag{3.2}$$

with P_{ref} and P_{out} the reflected and transmitted powers, respectively.

Figure 3.15 shows the variation of absorption index, reflection and transmission level as a function of frequency of hybrids made either by the *in-situ* or by the *ex-situ* foaming process. Except for the filling process, all other parameters are kept identical. The foam made of PC reinforced with 1wt% of CNT, foamed with a chemical foaming agent to the same density.

The *in-situ* foamed hybrid shows a cutoff frequency around 10 GHz due to the presence of the honeycomb. Below this cutoff, most of the incoming radiation is reflected back and cannot enter the material. Above the cutoff the EM wave enters the material with less reflection compared to a foam slab, meaning a higher level of absorption [41]. Due to the particular hybrid topology of the inserted foam, the absorption index

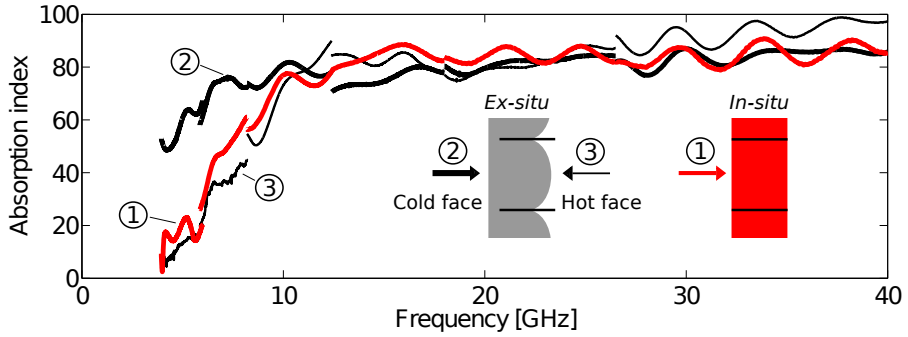

Figure 3.15: *Absorption index, A, in function of the frequency of an hybrid prepared by in-situ foaming, line number 1, or an hybrid prepared by ex-situ foaming followed by a mechanical insertion, line 2 and 3. Line 2 corresponds to a wave coming from the cold side and line 3 corresponds to hot face.*

depends on the face illuminated by the EM radiation. Below the cutoff, the remaining foam layer on the cold side allows the absorption of the incoming wave by lowering the impedance mismatch at the interface (see section 4.2).

Far above the cutoff, around 25 GHz, the hemispherical shape of the foam in the hot face improves the absorption. Indeed, the wavelength is on the order of magnitude of the hemispherical radius so that the non planar shape prevents the reflection to be normal to the surface. Instead, the reflection is partly towards the wall of the honeycomb which reflects again in the foam resulting in an improved absorption compared to a flat surface.

As highlighted in Figure 3.16, a partially filled honeycomb improves the absorption. The underlying mechanism is that a wave with a frequency between the cutoff frequency of the foam filled honeycomb and the empty honeycomb will be reflected back by the empty layer. This reflection prevents the wave to be transmitted through the hybrid and the reflected wave has to travel a second time through the dissipative layer. In this case, the overall reflectivity of the panel is increased but there is no transmitted radiation. This phenomenon can be replicated

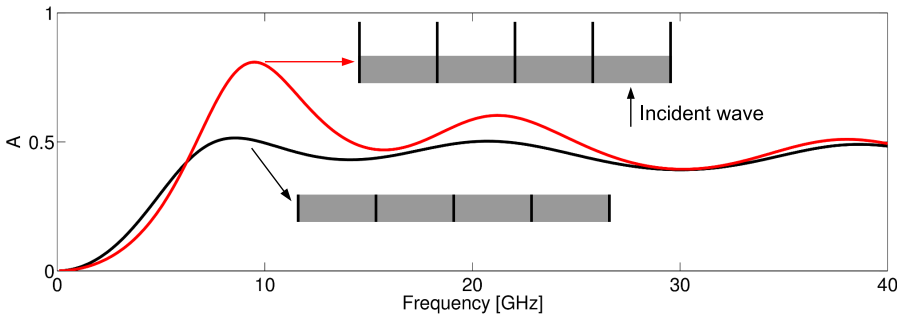

Figure 3.16: *Simulation of the absorption of an hybrid with a foam $\sigma = 0.8\ S/m$ and $\epsilon = 4$ in a HC with $X = 6\ mm$, (2) is an hybrid of 3 mm of thickness, (1) is a 3mm of foam inside a HC of 6mm.*

with a sandwich construction where one of the skin is highly conductive like a metallic or carbon fiber reinforced face or with a metallic coating. In other words, there is no need to fill the HC entirely which was one of the issue with mechanical insertion.

In order to determine the impact of the defects induced by the mechanical insertion, Figures 3.17(a) and 3.17(b) show a comparison of the absorption index of two scCO_2 foams from the same batch with different operating conditions for the insertion in the honeycomb. Because the foams come from the same batch, their permittivity, ε_r^*, is close so they should exhibit the same absorption capabilities. In Figure 3.17(a), one foam inserted at 150 °C and 10 mm·min^{-1} and the other one at 160 °C and 10 mm·min^{-1} are compared. They present different levels of foam contraction in the HC cell (see Figure 3.5). Despite the voids, the absorption capabilities of the hybrid is not affected significantly. This indicates that the defect size are sufficiently small in respect to the wavelength of the EM wave.

In Figure 3.17(b), the speed of insertion is 1 mm·min^{-1} with one mechanical insertion at 150 °C and the other at 160 °C. At 160 °C and 1 mm·min^{-1}, the foam presents a degradation of the microstructure with coalescence of the cells as highlighted in Figure 3.6. But the absorption level remains the same. This indicates that the CNT network is still

effective and that the cell diameter in the degraded zone is still sufficiently small with respect to the wavelength.

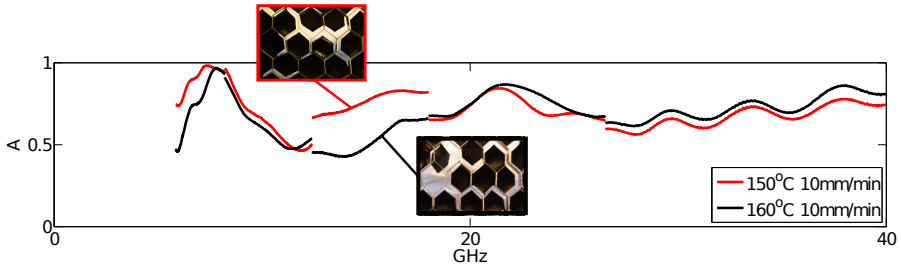

(a) PU/2wt% CNT CO_2 foamed inserted at $10\,\mathrm{mm{\cdot}min^{-1}}$ and 150 °C (black line) or $10\,\mathrm{mm{\cdot}min^{-1}}$ and 160 °C (red line)

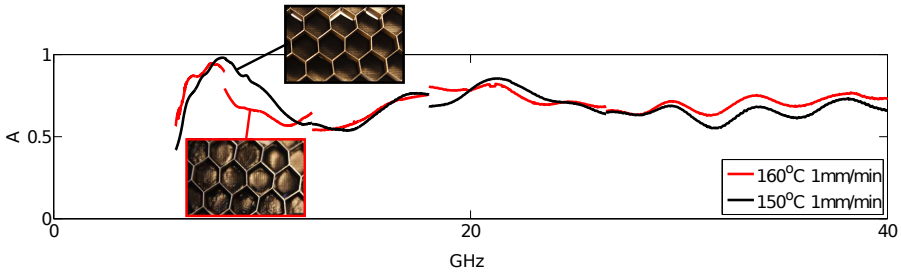

(b) PU/2wt% CNT CO_2 foamed inserted at $1\,\mathrm{mm{\cdot}min^{-1}}$ and 150 °C (black line) or $1\,\mathrm{mm{\cdot}min^{-1}}$ and 160 °C (red line)

Figure 3.17: *Influence of defects resulting from the mechanical insertion on the absorption index, (a) contraction of the foam in HC cells (b) thermal degradations (see Figure 3.5)*

3.3 Conclusions

Several processing routes have been followed to manufacture honeycomb filled with a nanocomposite foam for EM radiation absorption. An important conclusion resulting from this comparative analysis is that the electromagnetic absorption capacity of the new concept of hybrids described here is relatively insensitive to several types of apparent defects. Indeed, degradations, non completely filled honeycomb, or large foam

cell are not detrimental to EM absorption in the tested range of frequency. The question then is on the necessary mechanical performances required by the application. Note an important contribution to the structural performance will come from the face sheets.

In term of efficiency, scCO_2 foaming gives a finer microstructure and a more efficient carbon nanotube network than chemical foaming. This translates by an higher EM absorption index for foams with the same density. But the *in-situ* CO_2 foaming is still difficult to achieve without damaging the honeycomb. The minor defects due to the mechanical insertion of the foam inside the honeycomb does not affect the absorption capabilities but might be a major drawback in some application where a precise foam microstructure or sealing is needed. With the *in situ* chemical foaming method, it is more easy to generate a ready-to-use hybrid in a single processing step.

In terms of degrees of freedom, both polyurethane and polycarbonate proved to be suitable as hosting matrix. The final choice will depend on the rigidity needed for the foam and on the condition of use.

The choice of the processing route can thus be made as a function of the application and of the upscaling characteristics. The easier processing route is the *in-situ* foaming with the chemical foaming agent method because the finishing of the panel is excellent and the operation can be achieved in one step. But, in order to produce large panel with a semi-continuous process, the mechanical insertion of foamed nanocomposite with scCO_2 could be more suitable. Indeed, a large roll could push an heated honeycomb inside the foam in a more or less continuous way.

Chapter 4

Electromagnetic Absorption

The electromagnetic behaviour of the hybrids and of the sandwich panels is addressed in this chapter. A far-field approximation is used for the modelling. All the materials used to build the multifunctional panel possess a permeability equal to the unity. Therefore, the hybrid material can be reduced to a lossy dielectric slab in order to model the wave propagation. This chapter is divided in two sections. The first section, is dedicated to the EM absorption in the hybrids, the second is dedicated to the sandwich panels.

4.1 Hybrids

The EM absorption directly depends on the effective permittivity of the honeycomb filled with the nanocomposite foam which is modelled in this section. This effective permittivity can be then used to establish the transfer matrix. Derivation of the latter allows the extraction of the reflection and transmission, and, accordingly, the absorption of a dielectric layer. A finite element model is then used to assess the analytical model. Finally, actual samples have been characterized with a measurement method developed for this kind of material.

4.1.1 Effective permittivity

As stated in Section 2.2.1, the relative effective permittivity $\varepsilon_{r,eff}$ of a lossy slab writes

$$\varepsilon_{r,eff} = \varepsilon'_r - j\varepsilon''_r - \frac{j\sigma}{\omega\varepsilon_0}. \tag{4.1}$$

If the dielectric loss, ε''_r is neglected, equation (4.1) simplifies into:

$$\varepsilon_{r,eff} = \varepsilon'_r - \frac{j\sigma}{\omega\varepsilon_0} \tag{4.2}$$

with ε_r the relative permittivity, ε_0 the permittivity of vacuum, and σ the electrical conductivity of the material.

In the particular case of the nanocomposite foam, the relative permittivity follows a simple rule of mixture, see Section 2.1.3,

$$\begin{aligned}\varepsilon_{r,foam} &= f\varepsilon_{r,air} + (1-f)\varepsilon_{r,nanocomposite} \\ &= f\varepsilon'_{r,air} + (1-f)\varepsilon'_{r,nanocomposite} - (1-f)j\sigma_{nanocomposite}/\omega\varepsilon_0 \\ &= \varepsilon'_{r,foam} - j\sigma_{foam}/\omega\varepsilon_0 \end{aligned} \tag{4.3}$$

where f is the volume fraction of air, $\varepsilon_{r,air} = 1$ and $\varepsilon_{r,nanocomposite}$ is the relative permittivity of the nanocomposite involving its conductivity, using equation (4.2).

When the composite foam is inserted into the honeycomb structure, propagation inside each cell of the honeycomb is affected by the metallic walls of the cell. The problem is similar to that of a waveguide of rectangular cross section with metallic walls filled with a material of known complex permittivity $\varepsilon_{r,foam}$. The presence of the walls modifies the propagation constant, γ (remember equation (2.43)), with respect to pure Transverse ElectroMagnetic (TEM) propagation (neither electric nor magnetic field is in the direction of propagation) in free space: it becomes dependent on the width a and height b of the waveguide. For rectangular waveguides or cells, the canonical expression for the complex

propagation constant is

$$\gamma = j\sqrt{\varepsilon_{r,foam}\frac{\omega^2-\omega_0^2}{c_0^2}} = j\sqrt{\varepsilon_{r,foam}\frac{\omega^2}{c_0^2} - \left(\frac{m\pi}{a}\right)^2 - \left(\frac{n\pi}{b}\right)^2} \tag{4.4}$$

$$\gamma = \frac{j\omega\sqrt{\varepsilon_{effw}}}{c_0} \tag{4.5}$$

where $\omega = 2\pi f$, f is the frequency, c_0 is the speed of light and ε_{effw} is the equivalent of an effective permittivity associated with an equivalent TEM propagation.

Expression (4.4) implies the existence of a cutoff frequency f_0 depending on the size of the cell and on the index pair $(m,\ n)$ of the mode propagating inside the waveguide

$$f_0 = \frac{\omega_0}{2\pi} = \frac{c_0}{\sqrt{\varepsilon_{r,foam}}}\sqrt{\left(\frac{m}{2a}\right)^2 + \left(\frac{n}{2b}\right)^2}. \tag{4.6}$$

Above the cutoff frequency ($f > f_0$), $\gamma = j\beta$ is purely imaginary (if the losses are neglected), meaning that the propagation of the waves takes place along the z-axis with a transmission factor $e^{j\beta z}$ accounting for phase shift (or equivalently a delay of propagation in time domain). Below the cutoff ($f < f_0$), $\gamma = \alpha$ is purely real, meaning that the wave is attenuated with factor $e^{\alpha z}$, implying no propagation. Combining (4.4) with (4.3) of the foam permittivity, the effective permittivity of the waveguide can be rewritten as

$$\varepsilon_{r,effw} = \varepsilon'_{r,foam}\left(1 - \frac{\omega_0^2}{\omega^2}\right) - \frac{j\sigma_{foam}}{\omega\varepsilon_0}. \tag{4.7}$$

The positive or negative value of the real part of the effective permittivity is, thus, strongly related to the behaviour of the propagation constant, being purely real below cutoff, and imaginary above cutoff. Canonical expressions for the propagation constant exist only for rectangular or circular geometries. Using perturbation techniques, the cutoff frequency of a waveguide of arbitrary crosssection geometry is calculated from the variation ΔS of the surface of the cross section with respect to the

surface S of a rectangular one. The change of cutoff frequency resulting from an inward perturbation of the waveguide wall expresses, according to Harrington [43], as

$$\frac{\Delta f_0}{f_0} \approx \frac{\oint\!\!\oint_{\Delta S} (\varepsilon|E|^2 - \mu|H|^2)\, ds}{\oint\!\!\oint_{S} (\varepsilon|E|^2 + \mu|H|^2)\, ds} = -\frac{\Delta S}{S}. \tag{4.8}$$

The left-hand side of this expression assumes that the actual EM fields are approximated by corresponding electric field E and magnetic field H existing in the waveguide in absence of perturbation. It is valid when the perturbation is smooth enough, which is the case here: the lateral walls of the rectangular waveguide are progressively modified. Since the electric field is close to zero in the vicinity of the lateral walls for the dominant TE_{10}, mode of interest here, while the longitudinal magnetic field is maximum, the change in cutoff frequency is derived by using the analogy with the formulation available for cavity resonators [43], for the case of a perturbation occurring in a area where the magnetic field is maximum. The validity of this analogy can be verified by analytical calculations. Considering the hexagonal cell with edge size X and expressing X as a function of angle α and dimensions a and b of the rectangular cross section fitting the hexagon, the cutoff frequency f_{oh} of an hexagonal cell is given as

$$f_{0h} = f_0 \left(1 + \frac{cos\alpha}{1 + 2cos\alpha}\right) = \frac{5}{4} f_0, \quad for \quad \alpha = \frac{\pi}{3}. \tag{4.9}$$

Taking into account the fact that ΔS is negative owing to cross-section reduction, and that $\alpha = \frac{\pi}{3}$ for a regular hexagon. Next, according to [43], (4.4) and (4.7) established for a rectangular cell remain valid for the hexagonal cell, provided that (4.9) is used for the cutoff frequency f_o. The final expressions for the complex propagation constant, noted γ_h, and corresponding effective relative permittivity, noted $\varepsilon_{r,eff}$, associated with waves propagating through the hybrid material, reduce to

$$\gamma_h = j\sqrt{\varepsilon_{r,foam}\frac{\omega^2}{c_0^2} - \left(1 + \frac{cos\alpha}{1 + 2cos\alpha}\right)\left[\left(\frac{m\pi}{a}\right)^2 + \left(\frac{n\pi}{b}\right)^2\right]} \tag{4.10}$$

$$\varepsilon_{r,eff} = \varepsilon'_{r,foam} - \left(1 + \frac{cos\alpha}{1 + 2cos\alpha}\right)\left[\left(\frac{m\pi}{a}\right)^2 + \left(\frac{n\pi}{b}\right)^2\right]\left(\frac{c_0}{\omega}\right)^2 - \frac{j\sigma_{foam}}{\omega\varepsilon_0} \tag{4.11}$$

with $a = (1 + 2cos\alpha)\, X$ and $b = 2X sin\alpha$.

The geometric parameters of equations (4.10) and (4.11) are represented in Figure 4.1.

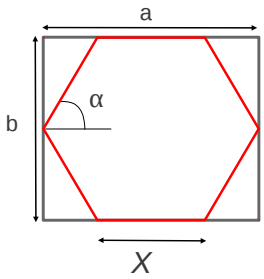

Figure 4.1: *Geometric parameters of equations (4.10) and (4.11)*

For the dominant mode (i.e., the mode having the lowest cutoff frequency), $m = 1$ and $n = 0$ and for a regular hexagonal cell ($\alpha = \frac{\pi}{3}$), (4.11) simplifies into

$$\varepsilon_{r,eff} = \varepsilon'_{r,foam} - \frac{5}{4}\left(\frac{\pi}{a}\right)^2\left(\frac{c_0}{\omega}\right)^2 - \frac{j\sigma_{foam}}{\omega\varepsilon_0} \quad . \tag{4.12}$$

The geometry of the honeycomb and/or the property of the foam can be tailored in order to improve the absorption in a specific range of frequencies. Indeed, if the geometry or the foam changes, the effective dielectric constant is affected. It means that the cut-off frequency is shifted, hence the range of frequencies over which absorption is improved is also modified.

Based on the analytical relationship (4.11), the following figures show how the real part of $\varepsilon_{r,eff}$ is affected respectively by the honeycomb size (Fig. 4.2), honeycomb angle (Fig. 4.3) and ε_r of the foam (Fig. 4.4). In order to decrease the cut-off frequency, the size of the hexagon or the dielectric constant of the foam has to be larger, or the angle has to be smaller.

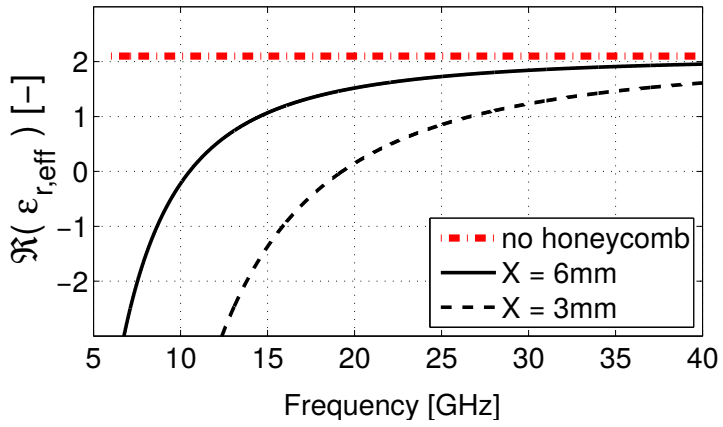

Figure 4.2: *Effect of the size of the honeycomb on* $\Re(\varepsilon_{r,eff})$ *calculated with* $\alpha = 60^o$, $\varepsilon_r = 2.1$, $\sigma = 1\ S/m$, $m = 1$ *and* $n = 0$ *in equation (4.11).*

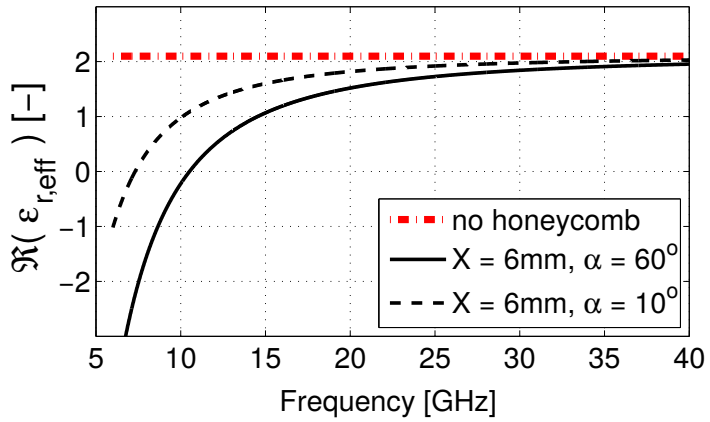

Figure 4.3: *Effect of the angle of the honeycomb on* $\Re(\varepsilon_{r,eff})$ *calculated with* $X = 6mm$, $\varepsilon_r = 2.1$, $\sigma = 1\ S/m$, $m = 1$ *and* $n = 0$ *in equation (4.11).*

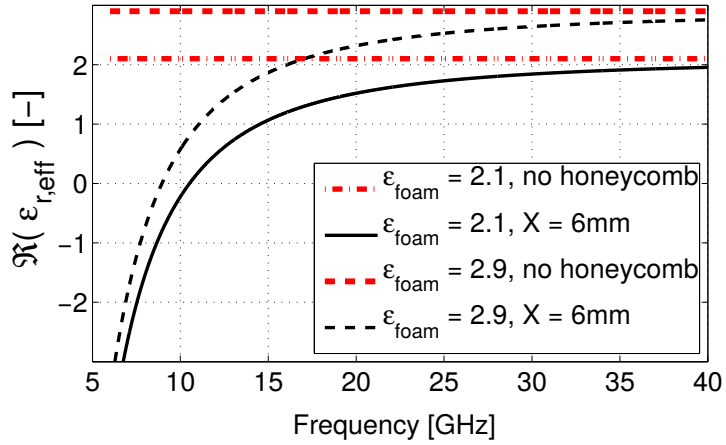

Figure 4.4: *Effect of ε_r of the foam on $\Re(\varepsilon_{r,eff})$ calculated with $\alpha = 60^o$, $X = 6mm$, $\sigma = 1\ S/m$, $m = 1$ and $n = 0$ in equation (4.11).*

4.1.2 Absorption model

A high EM absorption is achieved by reducing simultaneously the reflection of EM waves at the interface of the material with surrounding air and their transmission through the material. The fraction of EM power absorbed by a slab of material, denoted hereby absorption index A, is defined by the ratio between absorbed power P_{abs} and incident power P_{in}, expressed as:

$$\begin{aligned} A = \frac{P_{abs}}{P_{in}} &= 1 - \frac{P_{ref}}{P_{in}} - \frac{P_{out}}{P_{in}} \ , \\ &= 1 - |\Gamma|^2 - |T|^2 \ , \end{aligned} \tag{4.13}$$

with P_{ref} and P_{out} the reflected and the transmitted power, respectively.

Definition (4.13) implies that the absorption index A is improved when the reflected power P_{ref} and transmitted power P_{out} are decreased with respect to P_{in}.

For a single slab, the expression (4.13) for A can be rewritten, after some basic algebra, using the wave propagation formulation which depends on the effective permittivity of the medium. The reflection coefficient at the input interface of the slab writes

$$\Gamma = \frac{\rho\left(1 - e^{-2j\omega t\sqrt{\varepsilon_{r,eff}}/c_0}\right)}{1 - \rho^2 e^{-2j\omega t\sqrt{\varepsilon_{r,eff}}/c_0}} \tag{4.14}$$

and the transmission coefficient through the slab writes

$$T = \frac{(1-\rho^2)e^{-j\omega t\sqrt{\varepsilon_{r,eff}}/c_0}}{1 - \rho^2 e^{-2j\omega t\sqrt{\varepsilon_{r,eff}}/c_0}} \tag{4.15}$$

where $\omega = 2\pi f$, f is the frequency, t is the material thickness, c_0 is the speed of light, and ρ is the elementary reflection of the interface of the slab:

$$\rho = \frac{(1 - \sqrt{\varepsilon_{r,eff}})}{(1 + \sqrt{\varepsilon_{r,eff}})} \ . \tag{4.16}$$

However, it is not possible to generate a foam with a relative permittivity equal to the unity. The honeycomb structure incorporated into the

nanocomposite foam, shown in Fig. 1.4c, acts as a hexagonal waveguide with as consequence that the resulting multihierarchical material will show a decrease of the real part of its relative effective permittivity ($\Re(\varepsilon_{r,eff})$) near the cut-off frequency of the waveguide. The expression of the effective permittivity is given by equation (4.11).

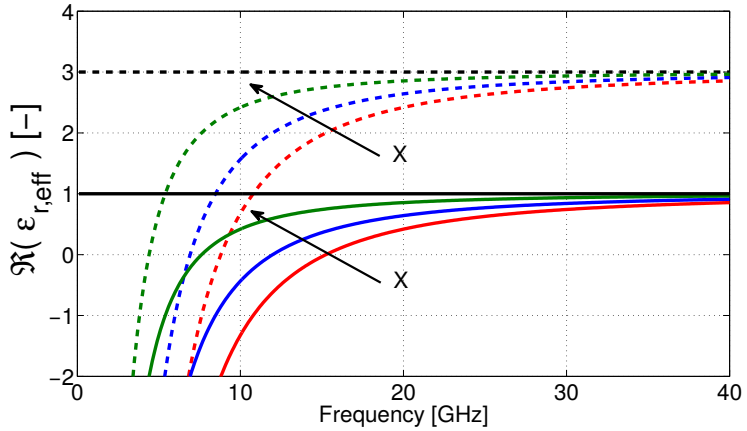

Figure 4.5: *Influence of the waveguide cell size X (5.5, 7 and 11 mm) on $\Re(\varepsilon_{r,eff})$ for the honeycomb filled with air ($\varepsilon_r = 1$) (solid lines) or with material characterized by σ=1 S/m and $\varepsilon_r = 3$ (dashed lines).*

If we look at the real part of the effective permittivity of the foam inside the waveguide, $\Re(\varepsilon_{r,eff})$ in equation (4.11), it can be concluded that below the cut-off frequency, $\Re(\varepsilon_{r,eff})$ is negative, and positive above, and remains always lower than the dielectric constant ε_r of the filling composite. The cut-off frequency is a function of the cell shape and of the relative permittivity ε_r of the filling material. Increasing the dielectric constant or the size of the hexagon will give a lower cut-off frequency. This behavior is illustrated in Figure 4.5.

4.1.3 Finite element modelling

Finite element modelling has been used to simulate EM reflection and transmission in the hybrid material. The software used is COMSOL. The foam has been modelled as an homogeneous material with a permittivity equivalent to the one measured experimentally. Different mesh refinements have been tested as well as different sizes of the Representative Volume Element (RVE).

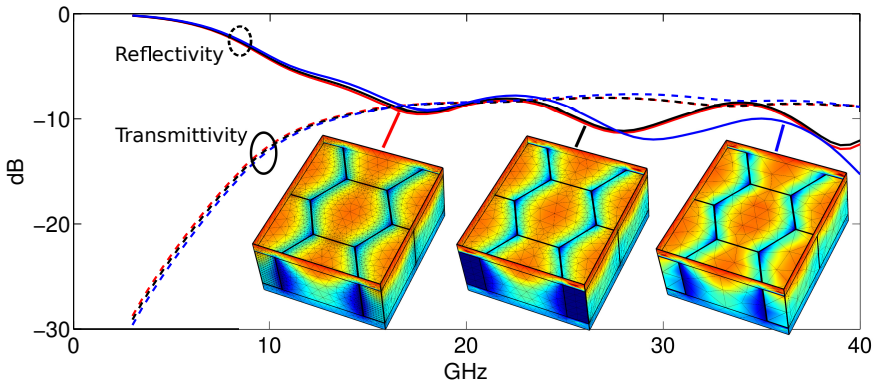

Figure 4.6: *Influence of the mesh size for the FEM simulation. Coarser mesh diverge at higher frequencies.*

The influence of the refinement of the mesh is shown in Figure 4.6. The coarser mesh diverges from the finer mesh at frequencies higher than 20 GHz that corresponds to a wavelength of 15 mm. At higher frequencies, the mean size of the coarser mesh elements, which is around 2.5 mm, is too close to the wavelength. No differences have been found between periodic boundary condition or symmetry planes implemented as perfect electric conductor for faces normal to the electric field and perfect magnetic conductor for faces normal to the magnetic field. The symmetries of the problem have been taken into account to limit simulation time.

Figure 4.7 shows no influence between the three RVE considered in the study: the smallest unit cell of the honeycomb, one hexagonal cell with the nearby cells cut in half and finally several hexagonal cells.

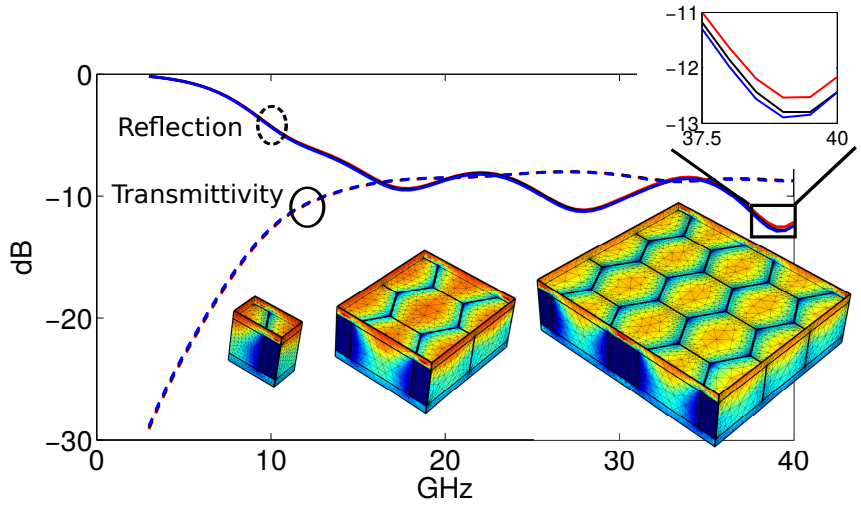

Figure 4.7: *Influence of the RVE size on the FEM simulation results. The three curves corresponding to the three different RVE cannot be distinguished indicating that the boundary conditions have been correctly imposed.*

4.1.4 Experimental measurement method

A measurement method have been especially developed for the hybrid material [44]. Nanocomposite foams are usually characterized using free space or guided wave techniques [45]. A very clean and efficient guided wave technique used for the characterization of foamed composites is the Line-Line method, which has been proposed in [46] for various types of materials such as microwave substrates, sandy soils, and liquids, using various transmission line topologies: microstrips, slotlines, and metallic rectangular waveguides. In the present section, only the waveguide topology is considered. The material-under-test (MUT) is successively inserted inside two rectangular waveguides of different lengths (the inner volume of the waveguide completely filled by the MUT) and its effective permittivity, from which the dielectric constant and electrical conductivity can be retrieved, is extracted from the S-parameters measurements of the two filled waveguides. The Line-Line method has been shown

to be quite equivalent to standard transmission-reflection and resonant cavity techniques [47]. Many characterization methods are based on the measurement of only one length of waveguide but require the numerical resolution of the inverse problem to extract permittivity values, [48] [49].

However, the main disadvantage of the Line-Line technique is that the samples have to be cut to fit the waveguides and this process has to be repeated for each frequency band considered. First, it is a destructive process. Second, a clean and precise machining of the sample is not always possible, for example, when samples are hard or brittle. This is especially true at higher frequencies because the dimensions of the waveguide cross section become very small.

To characterize samples composed of nanocomposite foam embedded in a metallic honeycomb, a new method has been developed that avoided these difficulties. It is based on the Line-Line technique but for which no waveguides are required as sample holders.

In the standard Line-Line technique proposed in [46], the MUT must fully fill the inner volume of two waveguides of different lengths; a "short" and a "long" one. Both waveguides are then successively connected, via coax-to-waveguide transitions, to a vector network analyzer (VNA) and the corresponding S-parameters are measured after a simple short-open-load-through calibration of the VNA. The value of the propagation constant γ can be calculated from these parameters [50]. For a waveguide of cross section $a \times b$, where b is smaller than a, the complex permittivity of the MUT filling the waveguide can be written as follows [51]

$$\varepsilon_{MUT} = c_0^2 \frac{-\gamma^2 + \pi^2/a^2}{\omega}. \tag{4.17}$$

For the modified Line-Line, the MUT is directly put and pressed between the coaxial-to-waveguide transitions of the desired frequency band, as shown in Figure 4.8. The MUT therefore has to be a rather thin (typically less than 1-cm thick) plate and must have two very flat and parallel faces. The transitions are then connected to the VNA and the S-parameters are measured, cf. Figure 4.8(c), this corresponds to the measurement of the "long" waveguide line. A measurement with the transitions pressed against one another is then a substitute for the "short"

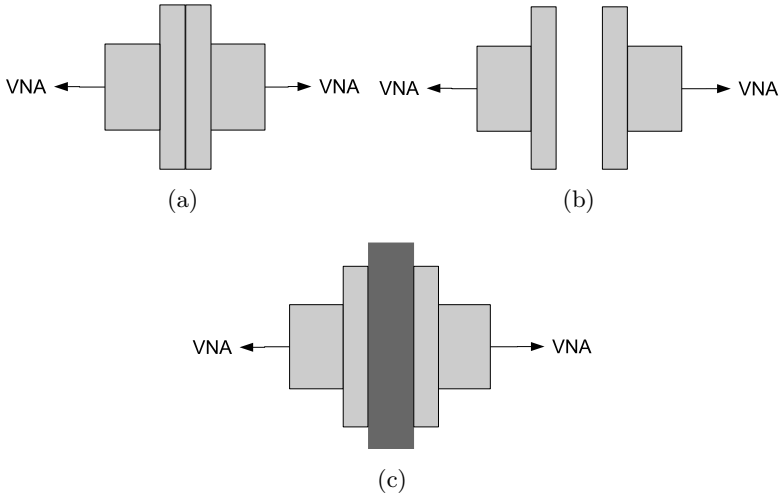

Figure 4.8: *Diagram of experimental set-up for the modified Line-Line technique, with the transitions against one another (a), the transitions separated by a length of air corresponding to the thickness of the sample (b), and with the sample inserted between the transitions without waveguide (c).*

line measurement, cf. Figure 4.8(a). A third measurement is made with nothing but air between the transitions, separated by a length of air equal to the sample thickness, cf. Figure 4.8(b). This last measurement is used as a correction to the measurement with the sample, to compensate for the absence of an actual waveguide. Indeed, using the transitions without waveguides and separated by a layer of air is very similar to free-space operation of a pair of antennas. The coax-to-waveguide to transitions are not necessarily very directive antennas. The emitted field has therefore the shape of a cone of unknown dispersion, and part of it might not reach the opposite transition or might also be reflected by the flanges. Because of this limitation, the modified Line-Line technique is a priori less exact and sensitive than the original Line-Line technique. Furthermore, a very precise alignment of the coaxial-to-waveguide transitions is necessary to minimize additional

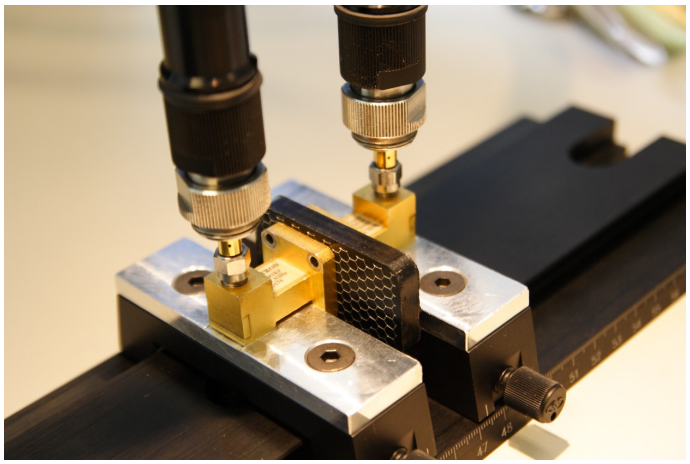

Figure 4.9: *Picture of the measurement of hybrid using the modified Line-Line method using a graduated rail and associated carriages especially designed to maintain the transitions in very good alignment and parallelism, at a known distance*

energy losses. This last concern was addressed by designing a specific set-up to align the waveguide-to-coax transitions. As shown in Figure 4.9, the transitions are bolted to small carriages that can be moved along a graduated rail. The parallelism was precisely checked during the set-up fabrication and the distance or length between the transitions can be externally measured or determined from the graduations, ensuring its exact value and adequate reproducibility of the positioning of the transitions.

The measurements were performed using a Vector Network Analyzer (VNA) Model Wiltron (Anritsu) 360, which allows covering the 40MHz - 40GHz frequency range or the model N5247A PNA-X 67(70) GHz from Agilent covering the 10MHz-67GHz frequency range of the four scattering parameters for any device connected between its two ports.

4.1.5 Results

Complex effective permittivity

The waveguide effect on $\Re(\varepsilon_{r,eff})$ is highlighted in Fig. 4.10 for honeycomb filled with PC-CNT 1wt% and 7.5wt% of CFA. Below the cut-off frequency, $\Re(\varepsilon_{r,eff})$ is negative for the hybrid while it remains almost constant and positive over the whole frequency range for the nanocomposite foam alone. The conductivity is not significantly modified by the presence of the metallic honeycomb. The cut-off frequency is identified at 10.87 GHz. It can be seen in Fig. 4.10 that the predictions obtained with the help of the analytical model matches the measurements, validating (4.11). The geometrical parameters were $X = 0$ or 5.5 mm and $\alpha = 60°$. The measured permittivity at 40 GHz represents here the relative permittivity of the foam and a linear fit was used for the measured conductivity over the studied range of frequencies.

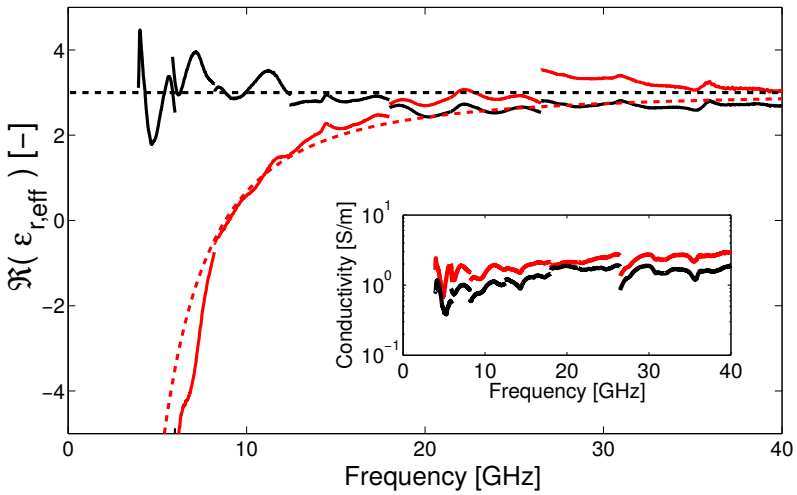

Figure 4.10: *Measurements (solid lines) and predictions (dashed lines) of the real part of $\varepsilon_{r,eff}$ with frequency for 7 mm thick PC-CNT 1wt.% foams with and without honeycomb (X=5.5 mm). Inside: measured conductivities of the samples.*

Experimental validation of the analytical and finite element model

Experimental measurements of hybrid panels have been compared to the analytical and finite element model. The panel have been process with a 4 mm thick and 10 mm cell size honeycomb. The foam filling the HC is a PC foam with 1 wt% of CNT. The density is set to $0.5\,\mathrm{g{\cdot}cm^{-3}}$.

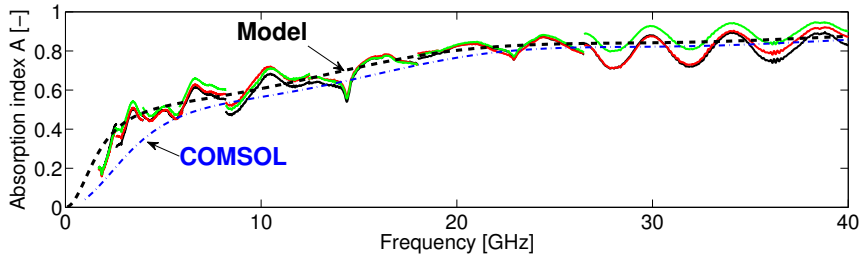

(a) Absorption index

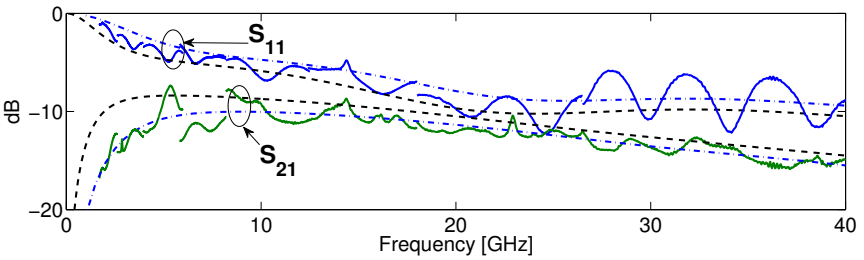

(b) S parameters

Figure 4.11: *Measurement of 4 mm thick hybrids with a honeycomb size X equal to 10 mm. The dielectric constant used in the models of the foam is the experimental value and is equal to 2.5. The conductivity used in the models is a linear fit of the experimental values. Discontinued solid lines are the experimental measurement of three different samples, the dashed line is a fit obtained thanks to the analytical model and the dashed-dot line is obtained with FEM. For clarity, only one sample is represented in Figure (b).*

Three different panels have been measured with TE_{10} propagation mode in order to check the reproducibility of the measurements. The measure-

ments have been used to extract the EM properties of the foam in order to insert them in the analytical and finite element model. The foam has a dielectric constant equal to 2.5. The conductivity used is a linear fit of the experimental values.

Figure 4.11.a shows the absorption index while Figure 4.11.b shows the reflection and the transmission. There is a good match between the absorption measured and the one predicted by the analytical model. FEM mostly underestimates the absorption at frequencies below 10 GHz. Because the foam EM properties are analytically extracted from the measurements may explain why there is a better match for the analytical model.

Effect of honeycomb wall thickness

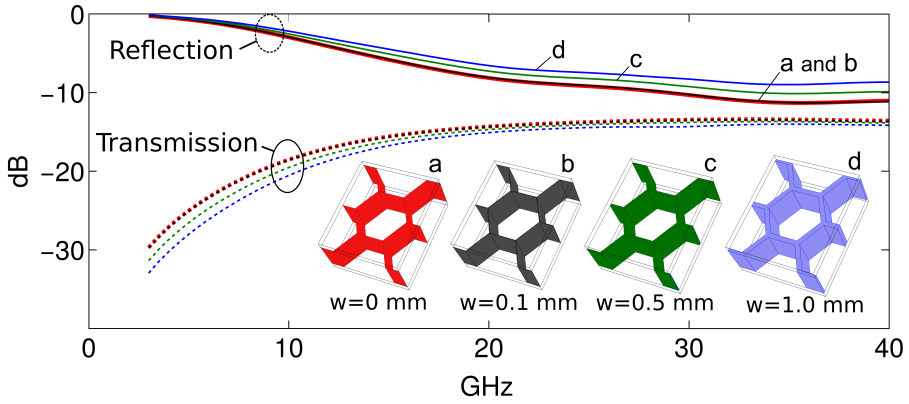

Figure 4.12: *Reflection (solid line) and transmission (dashed line) for hybrid with cell wall thickness, w, which is infinitely thin in red (a), 0.1 mm thick in black (b), 0.5 mm thick in green (c) and 1 mm thick in blue (d).*

Figure 4.12 shows the influence of the thickness of the honeycomb cell wall, w, on the S-parameters. Thickness ranging from 0 to 1 mm have been simulated. The FEM shows that thicknesses close to zero have no influence on the reflection and transmission of the hybrid. But as the wall becomes thicker, the reflection increases. A fraction of the incoming

radiation is reflected by the edges of the cell. The analytical model which does not take into account the honeycomb wall thickness, is then limited to thin walled honeycomb.

Temperature and humidity sensitivity

The operating condition of some potential applications for the hybrid material might be extreme in term of temperature and humidity. In order to evaluate these parameters on the absorption, measurements of the S-parameter have been realized in a climatic chamber. The same modified line-line method have been used. The climatic conditions that were used are indicated in Figure 4.13. For clarity, only measurements indicated by a vertical line on Fig. 4.13 are shown.

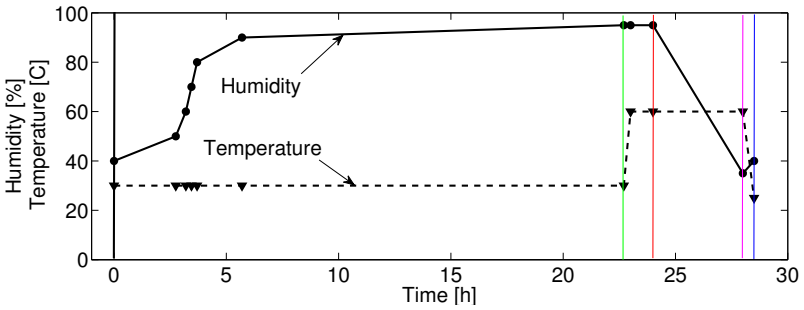

Figure 4.13: *Humidity and temperature profile corresponding to the environmental measurements. Dots represent measurement points. Vertical lines indicate measurements represented in Figure 4.14.*

Figure 4.14 shows that, in the range studied, the climatic condition has little influence on the reflection and transmission properties of the hybrid. Note that the lower reflection is obtained at 65 °C and 95% of humidity while the higher reflection is at 25 °C and 35% of humidity.

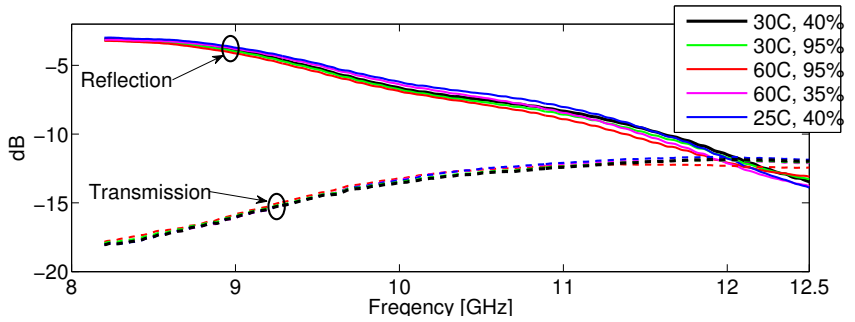

Figure 4.14: *S parameter for climatic condition in the X-band.*

Sensitivity to the polarisation and incidence angle

Depending on the polarisation of the incident EM field with respect to the honeycomb cell, the propagating mode of the wave inside the cell will vary. As shown in equation 4.11, the real part of the effective permittivity depends on the mode of propagation.

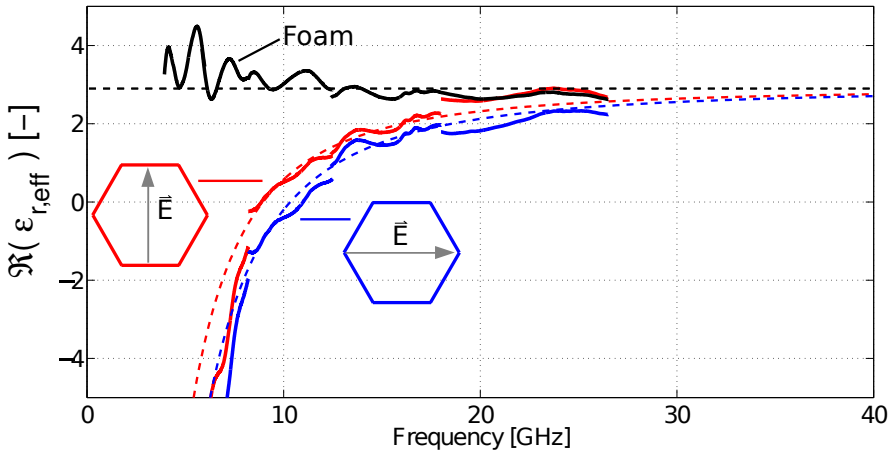

Figure 4.15: *Experimental measurement and analytical effective permittivity for 0° and 90° polarisation angle.*

Figure 4.15 compares $\varepsilon'_{r,eff}$ of a nanocomposite foam and of an hybrid for two polarisations of the electric field. In the graph, the red curve

corresponds to the mode of propagation TE_{10} (with $m = 1$ and $n = 0$ in equation (4.11)) and the blue curve corresponds to the TE_{01} mode (hence $m = 0$ and $n = 1$).

A more extensive analysis of the influence of the polarisation and incidence angle has been performed thanks to FEM. Figure 4.16 shows the absorption index, A, for several polarisation angle, ϕ, and incidence angle, θ. The incidence angle ranges from normal incidence, 0°, to 80°. Figure 4.16 reveals that for θ equal to 20° and 40°, A is close to the absorption at normal incidence for $\phi = 0°$ and 90°. However, A is higher for $\phi = 22.5°$, 45° and 67.5°. Indeed, the oblique incidence reduces the reflection and elongates the path of the wave inside the absorber which decreases the transmission coefficient. If θ is increased furthermore, the reflection is increased which reduces the total amount of power absorbed. For normal incidence, FEM does not predict an influence of the polarisation angle. This last point is still under investigation.

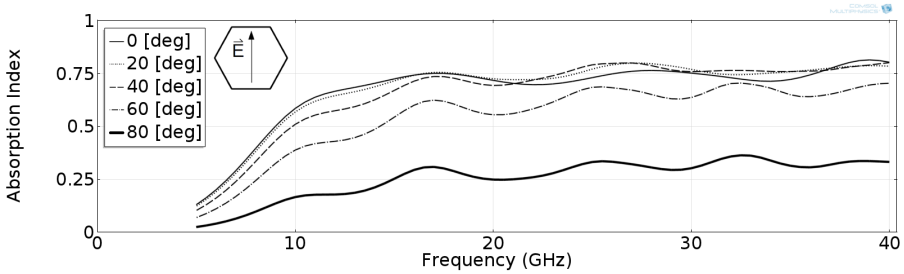

(a) $\phi = 0°$

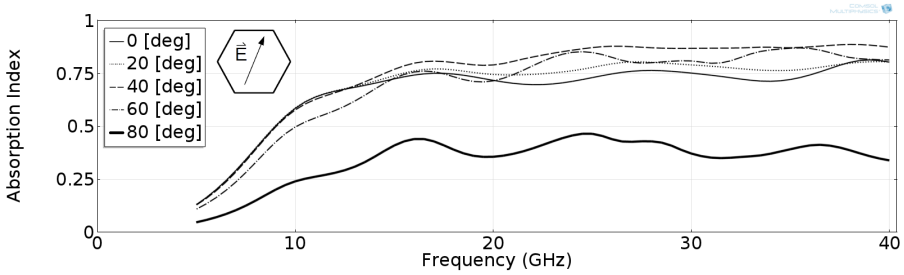

(b) $\phi = 22.5°$

Figure 4.16: *Finite element modelling of the influence of the incidence angle on the absorption index: for a polarisation angle, ϕ equal to 0° (a), 22.5° (b), 45° (c), 67.5° (d) and 90° (e). Part 1*

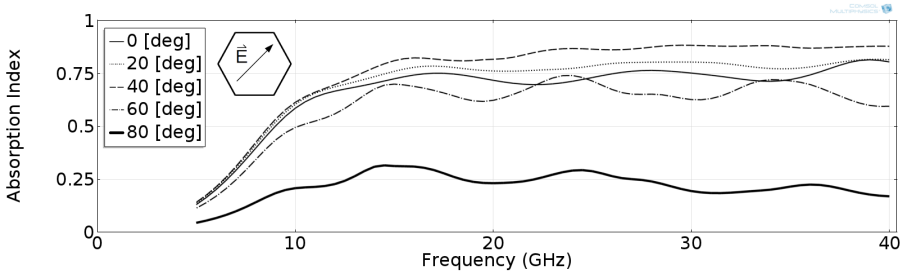

(c) $\phi = 45°$

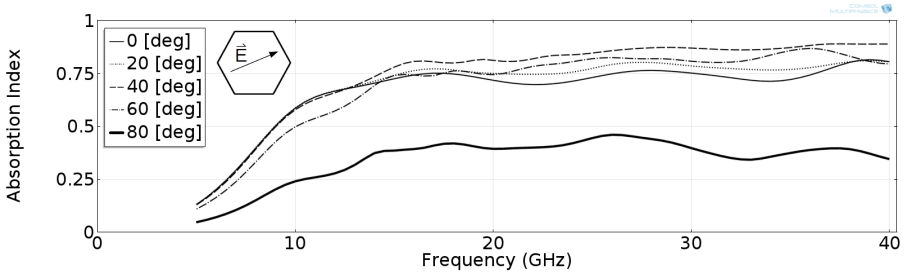

(d) $\phi = 67.5°$

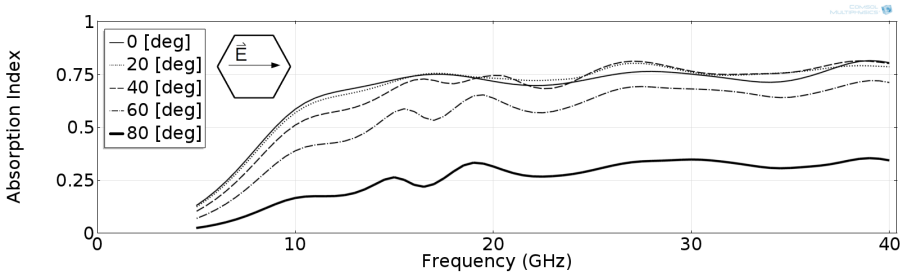

(e) $\phi = 90°$

Figure 4.16: *Finite element modelling of the influence of the incidence angle on the absorption index: for a polarisation angle, ϕ equal to 0° (a), 22.5° (b), 45° (c), 67.5° (d) and 90° (e). Part 2*

4.2 Sandwich Panel

In this section, a transfer matrix for the sandwich panel is determined using the chain product of the transfer matrix of the faces and the core, here the hybrid. In order to keep the absorption capability of the panel, the face sheet facing the incoming radiation needs to be transparent to EM radiation.

4.2.1 Absorption model and FEM modelling

The sandwich panel is obtained by adding a layer of Glass Fiber Reinforced Polymer (GFRP) on each face of the core slab (Fig. 1.4d). Calculation of the absorption index in this case can be made using the product of chain matrix [9] of input GFRP, hybrid core and output GFRP, respectively, which are function of the elementary reflection, ρ_i, and transmission, τ_i, coefficients at each interfaces.

$$\rho_i = \frac{(\sqrt{\varepsilon_{eff,(i)}} - \sqrt{\varepsilon_{eff,(i+1)}})}{(\sqrt{\varepsilon_{eff,(i)}} + \sqrt{\varepsilon_{eff,(i+1)}})} \tag{4.18}$$

$$\tau_i = 1 + \rho_i \tag{4.19}$$

with i varying from 1 to 4, corresponding to the interface air-GFRP, GFRP-hybrid, hybrid-GFRP, GFRP-air (Fig. 4.17).

Assuming EM wave incident from the left hand side interface 1 at Fig. 4.17, the expression for the overall reflection, Γ_1, is calculated from reflection of each slab starting at interface 4 ($i = 4 \rightarrow 1$, see Fig. 4.17a):

$$\Gamma_i = \frac{\rho_i + \Gamma_{(i+1)} e^{-2jk_i l_i}}{1 + \rho_i \Gamma_{(i+1)} e^{-2jk_i l_i}} \tag{4.20}$$

Because there is no wave entering the panel from the right hand side (interface 4 at Fig. 4.17) Γ_4 is simply equal to ρ_4.

The overall transmission coefficient of the sandwich, T, writes

$$T = (T_1 T_2 T_3 \tau_2 \tau_3)^{-1} \tag{4.21}$$

with T_i the transmission coefficient of one slab in the sandwich (see Fig. 4.17b):

$$T_i = \frac{\tau_i \tau_{(i+1)} e^{-jk_i l_i}}{1 + \rho_i e^{-2jk_i l_i} \Gamma_{(i+1)}} \ . \tag{4.22}$$

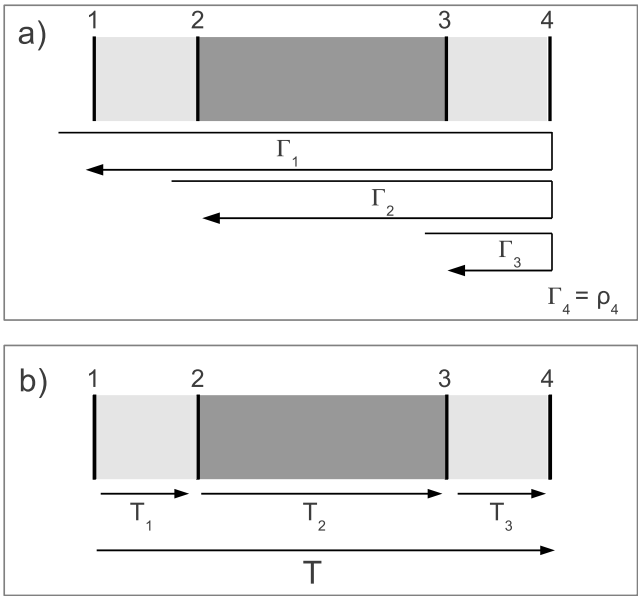

Figure 4.17: *Schematic view of (a) the reflexion coefficient Γ_i and (b) transmission coefficient T_i. The interface varying from 1 to 4 correspond to the interface air-GFRP, GFRP-hybrid, hybrid-GFRP, GFRP-air.*

4.2.2 Results

The same modified line-line method described in the previous section has been used to characterize the absorption of the sandwich panel. The absorption indices extracted from the measured S-parameters of the hybrid ($t = 7\,\text{mm}$) and sandwich ($t = 9.4\,\text{mm}$) with foam or hybrid cores are shown in Fig. 4.18. If two sandwich structures are compared, it is observed that below 10 GHz, the foam core involves better absorption indices than the hybrid core due to the cut-off, i.e. negative values

of $\varepsilon_{r,eff}$. However, from 10 to 18 GHz the hybrid with $X = 5.5\,\text{mm}$ performs better than the nanocomposite foam. Above 18 GHz, the absorption index is close to the one of the nanocomposite foam. At high frequencies the absorption index of the hybrid and of the nanocomposite foam become similar.

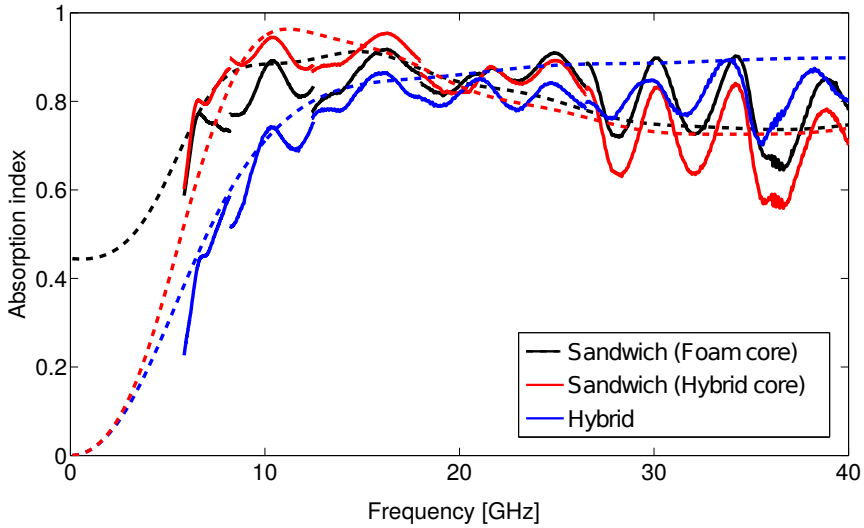

Figure 4.18: *Variation of the measured (solid lines) and predicted (dashed lines) absorption index as a function of the frequency for 7 mm thick honeycomb ($X = 5.5\,\text{mm}$) filled with PC-CNT 1wt.% foam (blue), for sandwich with a foam core (black) and for sandwich with hybrid core (red). The parameters of the model are $\varepsilon_{r,face} = 5$, $t_f = 1.2\,\text{mm}$, $\varepsilon_{r,foam} = 3$, the conductivity is a linear fit of the measurement (Fig. 4.10).*

Adding face sheets to the hybrid improves the absorption below 20 GHz by lowering the overall reflection of the sandwich (Fig. 4.19). Above 20 GHz, the sandwich panel involves a higher reflection than the hybrid alone. As a result, the amount of power absorbed by the material is lower (see equation (4.13)). Some differences between the measurements and predictions were observed. Predictions were made using a linear fit of σ over the frequency range and by picking $\varepsilon_{r,foam}$ at 40 GHz, here equal

to 3. Locally, variations in σ are changing the absorption levels. The true value of $\varepsilon_{r,foam}$ should be a little higher because of the remaining influence of the honeycomb waveguide at 40 GHz (see example in Fig. 4.5). The foam microstructure and the non perfect hexagonal shape of the metallic honeycomb could lead to some oscillations and shift of the cut-off in the data compared to the predictions. Also, the dielectric constant of the glue was approximated to be the same as the face sheet and equal to 5. The thickness of the layer of glue is also not equal to 0.2 mm everywhere on the sample.

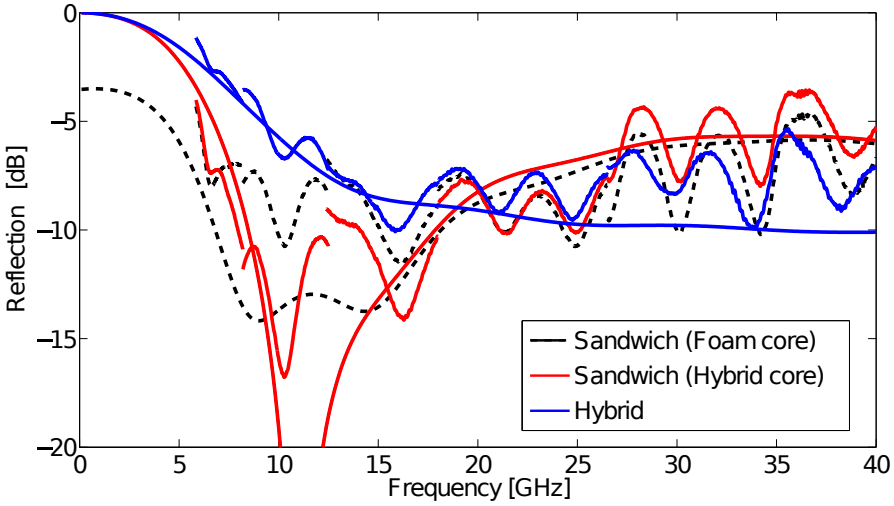

Figure 4.19: *Variation of the measured (solid lines) and predicted (dashed lines) reflection as a function of the frequency for 7 mm thick honeycomb ($X = 5.5\,mm$) filled with PC-CNT 1wt.% foam (blue), for sandwich with a foam core (black) and for sandwich with hybrid core (red). The parameters of the model are $\varepsilon_{r,face} = 5$, $t_f = 1.2\,mm$, $\varepsilon_{r,foam} = 3$, the conductivity is a linear fit of the measurement (Fig. 4.10.)*

In Figure 4.20, FEM has been used to compare the absorption index of an hybrid panel and a sandwich panel with 0.5 mm or 1.5 mm thick face sheets. As expected from the measurements, the sandwich construc-

tion improves the absorption. Compared to thick face sheets, thin face sheets shows a smaller improvement of the absorption but over a wider frequency range.

The interface impedance of a complex dielectric layer, Z_{in}, can be extracted from the reflection coefficient, S_{11}, with the following expression

$$S_{11} = \frac{(Z_{in} - Z_0)}{(Z_{in} + Z_0)} \quad , \tag{4.23}$$

leading to,

$$Z_{in} = Z_0 \frac{(1 + S_{11})}{(1 - S_{11})} \quad . \tag{4.24}$$

As it can be observed from equation (4.23), if the mismatch between the interface impedance and the air impedance is important, the reflection will be important. In Figure 4.21, the mismatch of impedance for the hybrid and for the sandwich panels is represented in the complex space. For the sandwich panel, the mismatch is reduced thanks to the GFRP faces which act as a matching layer. Indeed, the absorption peak at 13 GHz of the sandwich panel with 1.5 mm thick faces corresponds to the smallest mismatch between the three panels at this frequency.

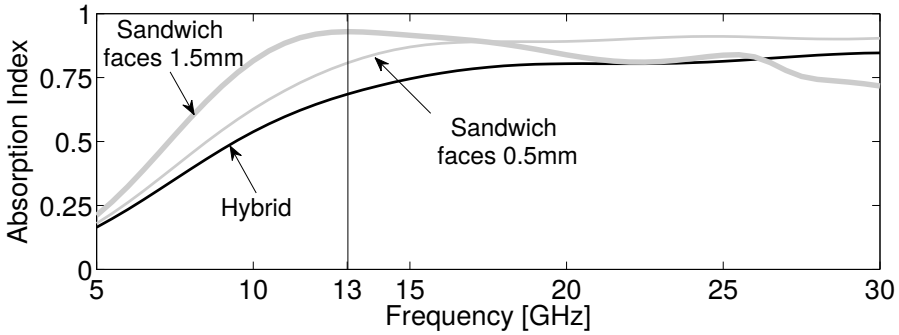

Figure 4.20: *FEM of the absorption index for an hybrid panel (black) and a sandwich panel with 0.5 mm (thin gray) or 1.5 mm (thick gray).*

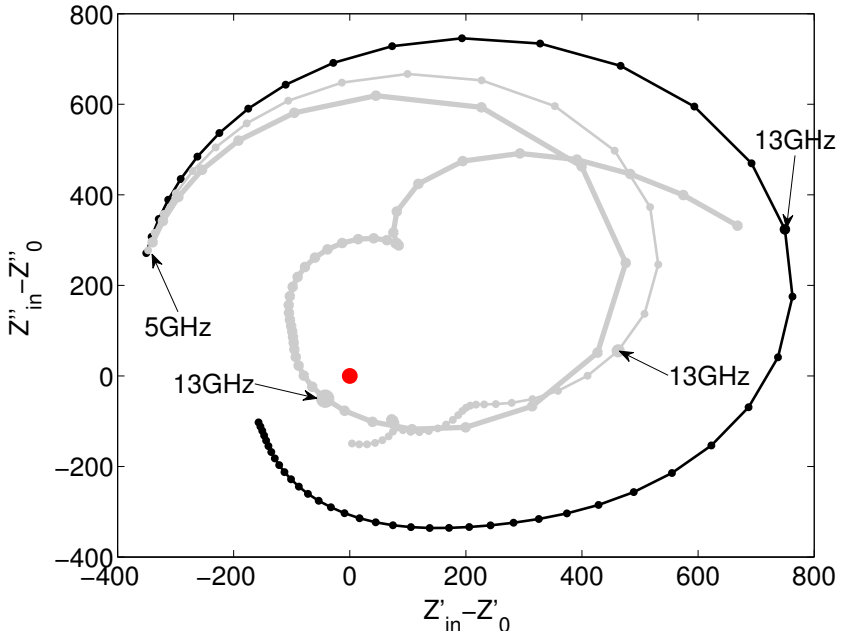

Figure 4.21: *Mismatch between interface impedance and air impedance , $Z_{in} - Z_0$, in complex space for an hybrid panel (black) and a sandwich panel with 0.5 mm (thin gray) or 1.5 mm (thick gray). Each dots is the mismatch at one frequency, the isolated red dot correspond to a perfect match meaning $Z_{in} - Z_0 = 0$.*

4.3 Conclusion

In this chapter, we have shown that the foam filled honeycomb cells act like a waveguide by influencing the real part of the effective permittivity. This creates a cutoff frequency below which the reflection of the hybrid is increased and above which the matching of the hybrid and air is improved, therefore reducing the reflection. An analytical model has been developed to predict the level of absorption of an hybrid slab or of a sandwich panel with an hybrid core. The absorption level and the cutoff frequency of the hybrid are not significantly impacted by :

- the environmental operating conditions as the humidity or temperature in the 8-12 GHz frequency band,
- the polarisation of the incoming signal relative to the honeycomb orientation,
- the incidence angle of the EM radiation, which is, up to 40°, slightly higher compared to normal incidence.

The addition of face sheets transparent to EM wave to produce the sandwich structure reduces the mismatch between the hybrid and air but only within a specific range of frequencies.

Chapter 5

Metamaterial approach for absorption below cutoff frequency

In this chapter, the absorption frequency band of the hybrid is enlarged thanks to left-handed propagation below cutoff while preserving a good balance between stiffness/weight ratio, thermal conductivity, and compacity.

5.1 Introduction

A metamaterial is a synthetic composite material with a structure such that it exhibits properties not usually found in natural materials. A more general definition is given by Lee et als. [52] : "A material whose effective properties arose not from the bulk behavior of the materials which composed it, but more from their deliberate structuring. Therefore, metamaterials sit at the intersection of two classical categories, materials and devices". Metamaterials have emerged from the EM domain with material having a negative permittivity and negative permeability but are not restricted to EM. Metamaterial can be used to manipulate mechanical properties [53] [54], in order to obtain, for example, a negative Poisson's ratio or to manipulate acoustic properties [55], for example, a negative dynamic bulk modulus and negative effective mass density.

Although the EM properties of a material are fully specified by the permittivity ε and permeability μ, the refractive index $n = \sqrt{\varepsilon_r \mu_r}$ is also often used. By convention the positive square root is used for n. If ε_r or μ_r is negative, n becomes imaginary, meaning no transmission in the material. However, when ε_r and μ are negative, n is real but it is necessary to take the negative square root for n [56]. Materials with negative n have interesting properties which are illustrated on Figure 5.1. Refraction follows the Snell's law, $n_1 sin\theta_1 = n_2 sin\theta_2$, but as n_2 is negative, the rays will be refracted on the same side of the normal on entering the material. In conventional materials, the group velocity, which characterizes the flow of energy, and the phase velocity, which characterizes the movement of the wave fronts are parallel. By contrast, the group and phase velocities point in opposite directions when $\varepsilon < 0$ and $\mu < 0$. For plane waves propagating in electromagnetic metamaterials, the electric field, magnetic field and wave vector follow a left-hand rule. This is a reversal of direction when compared to the behaviour of conventional optical materials.

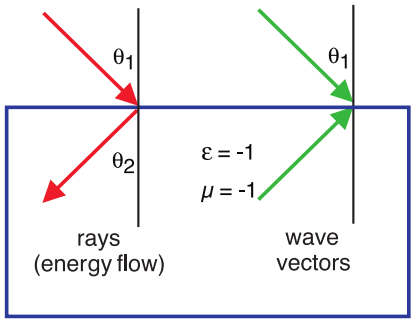

Figure 5.1: *From [56] Negative refraction in operation: On the left, a ray enters a negatively refracting medium and is bent the wrong way relative to the surface normal, forming a chevron at the interface. On the right, we sketch the wave vectors: Negative refraction requires that the wave vector and group velocity (the ray velocity) point in opposite directions.*

In order to tune the permittivity and permeability to the desired values, several strategies exist. At gigahertz frequencies, the more common

method is to use periodic structure with sub-wavelength size. In order to control the permittivity, a wired medium is often used, Figure 5.2(a) while Split Ring Resonators (SRR) are wildly used to control the permeability, Figure 5.2(b). Combination of the two leads to double negative medium exhibiting a negative refractive index, Figure 5.3. SRRs are narrowband and lossy due to their resonant behaviour.

Split ring resonators are loops made of an electrical conductor metal. When a magnetic flux penetrates the ring, a current is induced in the loop. The split in the ring acts as a capacitance. This capacitance allows the ring to resonate at wavelength much larger than the ring diameter. Because the magnetic flux needs to penetrate the ring, the resonance occurs for one polarization only.

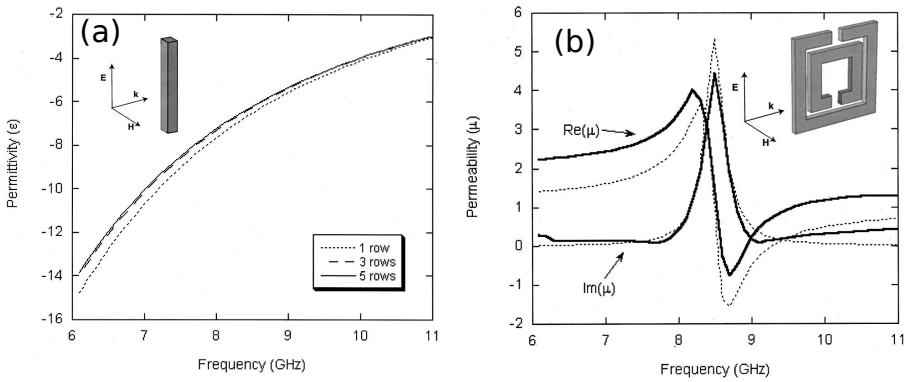

Figure 5.2: *From [57] (a) Real part of the permittivity as a function of frequency for a wire medium and (b) Permeability as a function of frequency for the SRR medium, for one or more unit cell lengths. The solid dark lines correspond to the real and imaginary parts of the permeability determined by simulation (transfer matrix method), while the dashed lines were obtained from analytical model by assuming parameters chosen to approximate the SRR medium. Note that at ∼8.5 GHz the real part of the permeability goes negative, with a bandwidth of ∼0.5 GHz. The inset depicts the orientation of the wire or SRR with respect to the incident radiation.*

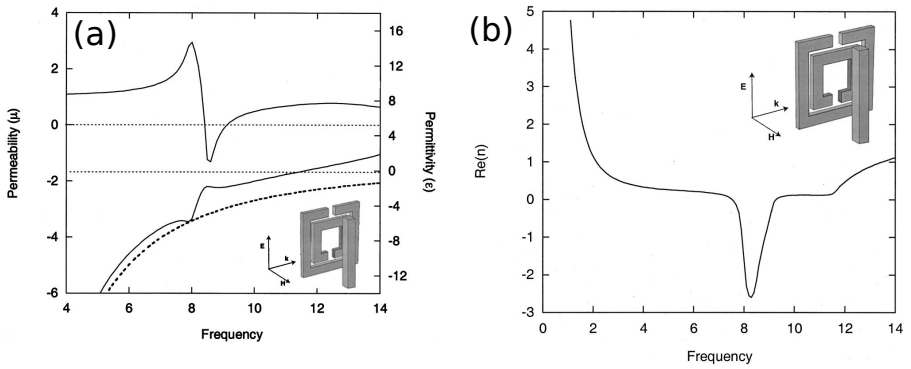

Figure 5.3: *From [57] (a) Recovered $\Re\mu$ [top curve, left-hand scale] and $\Re\varepsilon$ bottom, solid curve, right-hand scale as a function of frequency for the combination SRR/wire medium. The flat dashed lines indicate the zero values for the two axes(offset for clarity) Note that while the addition of the SRR medium to the wire medium results in a more positive permittivity (solid line) than wires alone (dashed curve), nevertheless there is a frequency region ∼8.5-9.0 GHz where both μ and ε are negative. and (b) Refractive index (n) as a function of frequency for the combination SRR/wire medium. The region where the index is negative corresponds to the frequency region where both μ and ε are simultaneously negative.*

Metamaterials can be used in order to absorb EM radiations. Metamaterials allow to manipulate the imaginary part of the permittivity and the permeability in order to increase the tangent losses. A wideband ultrathin metamaterial absorber based on circuit analog absorber has been proposed in reference [58].

Thanks to the metallic honeycomb, the stiffness and the thermal conductivity of the hybrid is increased. In terms of electromagnetic behaviour, each cell of the hybrid acts like an effective metallic waveguide filled with a lossy medium. As explained in section 4.1.1, it exhibits a cutoff frequency above which the absorption is improved over the nanocomposite because of improved matching at air/composite interface ($0 < \varepsilon'_{eff} < \varepsilon'_{nanocomposite}$). But below this cutoff no propagation is possible due to a negative effective permittivity ($\varepsilon'_{eff} < 0$), see Figure 5.4.

In order to recover absorption below this cutoff while keeping the same thickness and almost the same architecture, a metamaterial combining $\varepsilon' < 0$ and $\mu' < 0$ is created by the inclusion of splits rings resonators (SRR) that resonate below the cutoff of the honeycomb cell [59]. Such structure achieves EM absorption over a wider frequency band thanks to left-handed propagation below cutoff, while preserving a good balance between stiffness/weight ratio, thermal conductivity, and compacity.

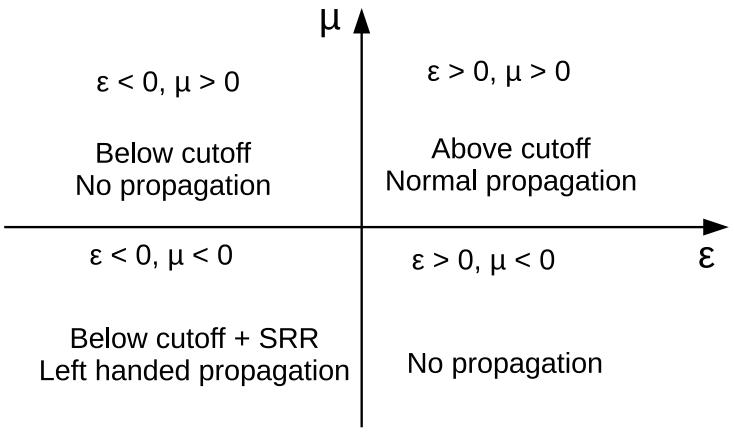

Figure 5.4: *Propagation map as a function of the sign of the permittivity and the permeability. In the hybrid, only the permittivity is negative below cutoff implying no propagation inside the honeycomb cell. The addition of a split ring resonator in the cell, sets the permeability to negative value allowing left handed propagation into the cell.*

5.2 Process of the metamaterial

The split ring resonators are made of copper on a Rogers RT Duroid 5870 dielectric substrate. The layer of Cu is $17\mu m$ thick on a 0.5 mm thick dielectric with ε equal to 2.33. The rings have an external diameter of 6 mm, are 0.15 mm wide with 10° gap opening. A precise positioning of the rings inside the cell is required in order to activate the resonance.

With the foaming method developed for the hybrid, this precision cannot be achieved. Instead, a bi-component epoxy resin (Epofix struer) is used as host medium for multiwalled carbon nanotubes (Nanocyl^{TM} NC 7000). 0.75% in weight of CNT were added to the resin and mixed by ultrasonication for 7 min before adding the hardener. The mix was cured at room temperature in a vacuum oven to avoid bubbles. A 7 mm thick honeycomb was used (CRIII-3/8-5052-.004-5.4, HexWeb®, Hexcel), involving 100 µm thick aluminium sheets forming 5.5 mm-sided hexagons.

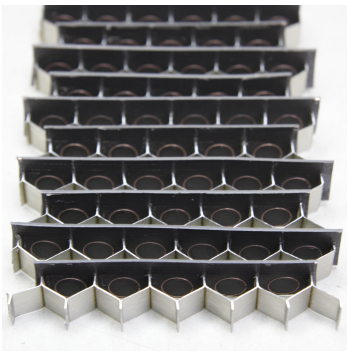

(a) Step 1: SRR before pouring the composite.

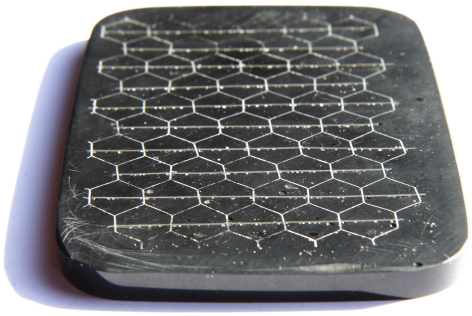

(b) Step 3: Final metamaterial after removing the exceeding material.

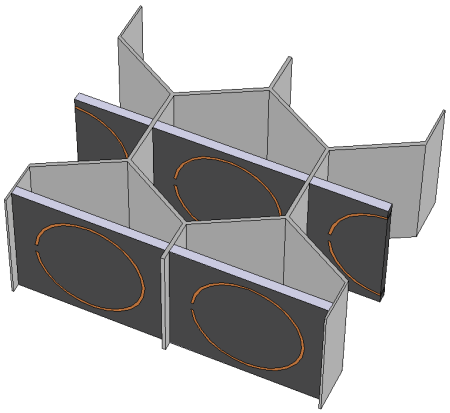

(c) Geometry for the simulation

Figure 5.5: *(a,b) Processing steps and (c) idealized structure for FE simulation*

The process, illustrated on Figure 5.5, is composed of 3 stages. First, strips of Rogers dielectric substrate with metallic single split rings are inserted in the honeycomb, Figure 5.5(c). The height of the substrate strip is kept greater than the height of the honeycomb cells for easier manipulation (cf. Figure 5.5(a)). In a second step, the nanocomposite is poured in the previous structure. Finally, all the exceeding (substrate of the rings and epoxy) is mechanically removed, Figure 5.5(b). Some bubbles still remain in the resin despite curing under vacuum.

5.3 Absorption FEM modelling and Measurement

The measurements were performed using a Vector Network Analyzer (VNA) Model Agilent PNA-X N5247A, which allows the measurement over the 10 MHz - 67 GHz frequency range of the four scattering parameters for any device connected between the two ports. The same method described in section 4.1.4 is used.

COMSOL simulations are performed with periodic boundary condition, and with a layer of 1.5 mm of air at each side of the honeycomb. Figure 5.5(c) shows the geometry used for the simulation. One strip of rings is slightly shifted from the center of the cell.

5.4 Results

Figure 5.6 compares the transmission scattering parameters S_{21} for two air-filled configurations: the honeycomb alone (top red curves), and the corresponding metamaterial configuration of Fig. 5.5(a) including single SRR in the HC cell (bottom black curves). During the measurements, the substrate outside the honeycomb is facing Port 2 and the distance between the transition launchers is equal for the two samples. No significant transmission is observed in the HC alone (top graph) because the cutoff is located around 18 GHz. When SRRs are inserted, significant transmission peaks appear (bottom black curves), that are associated to resonances induced by the SRR around 5 GHz, 6.8 GHz, and 12.3 GHz.

Despite the extra substrate in port 2 for the measurement (remember Fig.5.5(a)), and imperfect positioning of SRR occurs in some HC cells, there is a good agreement between the experimental data and FEM simulations.

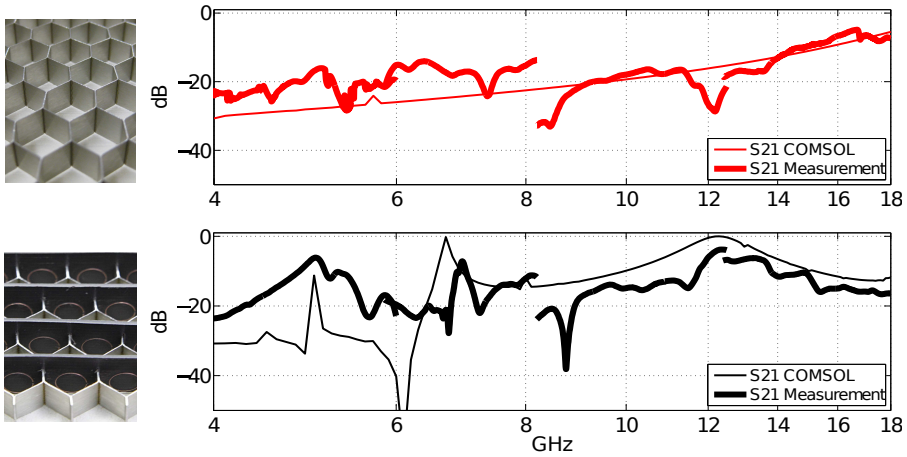

Figure 5.6: *S_{21} parameter of the HC (red) and metamaterial (black) for measurement (thick) and simulation (thin).*

Figure 5.7 considers the case where a conductive nanocomposite is filling each of the two configurations studied at Figure 5.6. Because of losses, an absorption index associated to power balance can be defined as $A = \frac{P_{abs}}{P_{in}} = 1 - |S_{11}|^2 - |S_{21}|^2$ [23]. As expected from Fig. 5.6, since filling the honeycomb with SRR in each cell allows power penetration in the structure below the cutoff frequency of the HC (in this case at 9GHz), significant absorption maxima are observed around 4.5GHz and 7.2GHz below the cutoff frequency, that are not present when only the nanocomposite is filling the honeycomb. As a result, the absorption bandwidth at a given geometry (HC cell size and thickness) is improved. The carbon nanotubes-epoxy composite is a less effective EM absorber compared to the nanocomposite foam studied in Chapter 4. Therefore, the absorption index of the hybrid filled with carbon nanotubes-epoxy composite is lower.

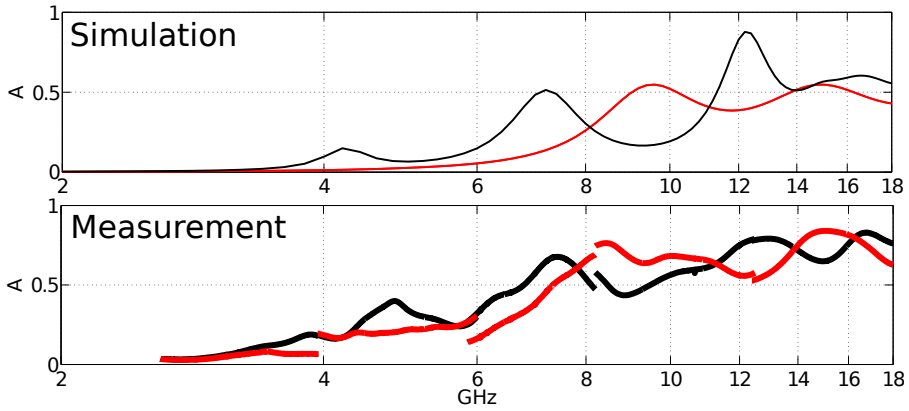

Figure 5.7: *Absorbed power of the HC (red) and metamaterial (black) for measurement (thick) and simulation (thin).*

On Figure 5.8, the left-handed propagation below the cutoff for the filled honeycomb can be confirmed by comparing the phase shift of the signal for one or two layers of honeycomb with SRRs. Indeed, because phase velocity within the left-handed transmission band is negative, an increase of the material thickness shifts the transmitted wave in the opposite compared to the right-handed transmission band [60].

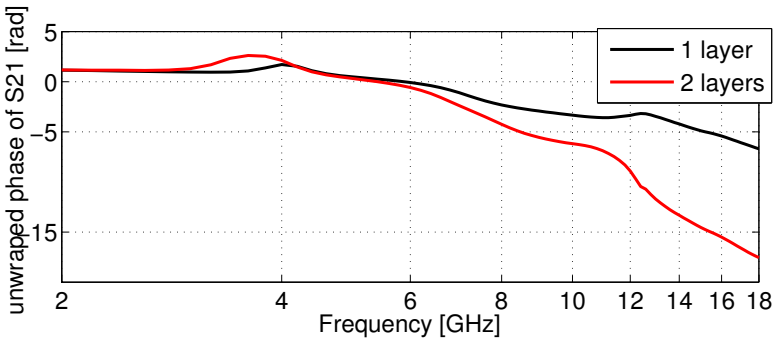

Figure 5.8: *phase in radian of the simulation for 1 and 2 layer of metamaterial*

Geometries other than "C" shaped SRR can be used. Square SRRs represented on Figure 5.9 can have their capacitance easily tuned and maximize the magnetic flux that can enter the ring. Two sizes of square SRR have been tested: 5 mm and 6 mm side length. Figure 5.9 shows that if the size of the SRR is increased, the resonance will occur at a lower frequency. Figure 5.9 also shows that alternating two sizes of SRR in the honeycomb cells broaden the peaks at the expense of the intensity.

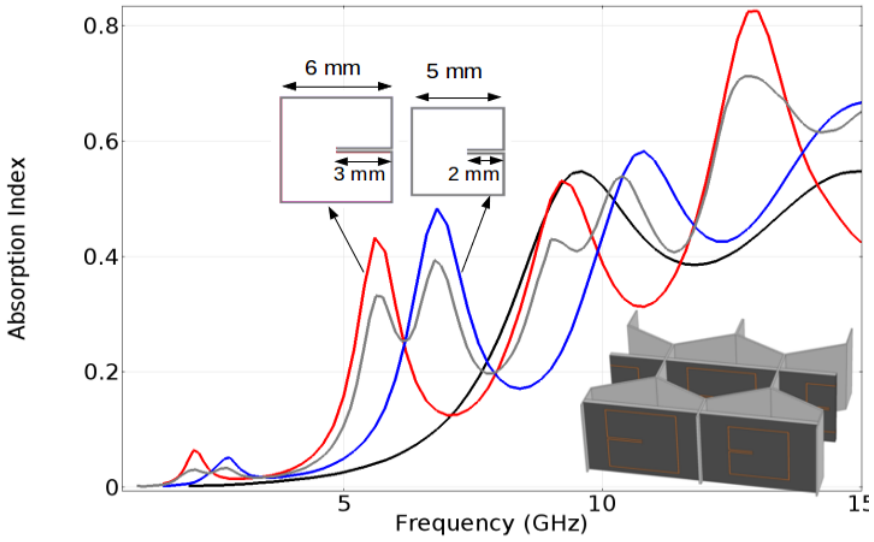

Figure 5.9: *Simulated absorption index for square Split Ring Resonator. Black line is without SRR in HC cell, red line is with large SRR, in blue with smaller SRR and the gray line corresponds to a mix of large and small SRR. The inset depicts the disposition of the SRRs of mixed sizes in the HC cells.*

On Figure 5.10 the S-parameters of a metamaterial realised with SRR with 5 mm sides length is shown. The lefthanded peak of the modelling is slightly shifted compared to the measurement.

By alternating the size of the SRR in each cell, several absorption peaks below cutoff can be obtained. On figure 5.11, experimental measurements confirm the prediction of the FEM.

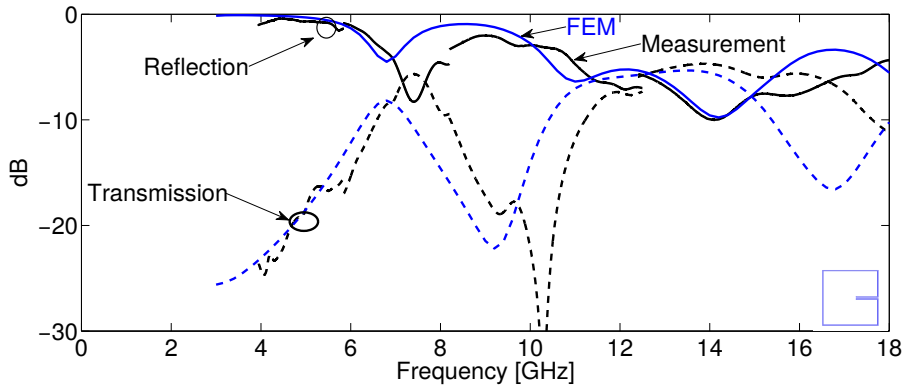

Figure 5.10: *S-parameters for square SRR of 5 mm size. In blue the FE modelling and in black the measurement.*

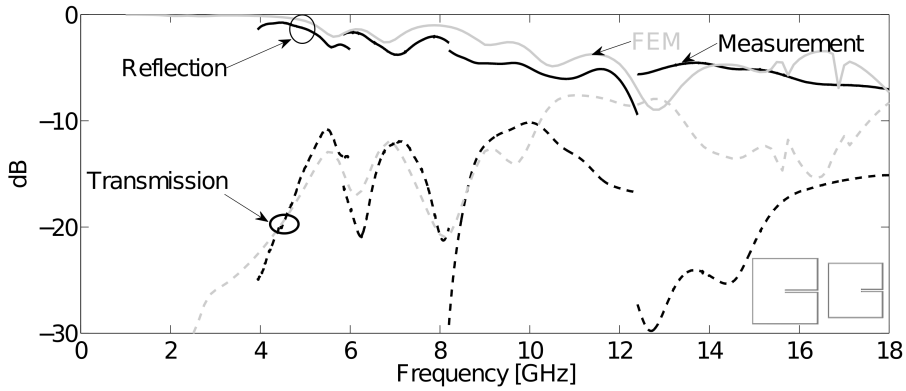

Figure 5.11: *S-parameters for square SRR with two sizes mixed.*

5.5 Conclusion

Thanks to the addition of split ring resonators in each cell of the honeycomb, left-handed propagation below the cutoff has been achieved, enlarging the operation bandwidth at a given geometry size. But adding SRRs complicates the process and is time consuming. SRRs are also sensitive to the polarization of the incoming radiation, the magnetic

field needs to be perpendicular to the SRR plane. Due to the resonance nature of SRR, the left-handed propagation is narrowband but using different sizes of SRR can enlarge the band.

A left handed structure could also be easily built by printing split ring resonators and strips on each cell face of a dielectric honeycomb. Such structure would be less sensitive to the incident polarisation of the incoming radiation.

Another alternative to the SRRs to activate left-handed propagation is by introducing ferromagnetic nanoparticules [61] [62]. These particles exhibit a ferromagnetic resonance which induces, around the resonance frequency, a negative effective permeability which is similar to SRRs. Such particles can be dispersed into the hosting matrix in the same processing step than the CNT.

Chapter 6

Mechanical properties

This chapter addresses the mechanical performances of the hybrids and sandwich panels with a hybrid as core. Four-points bending, compression and impact have been carried out until failure of the material. All the hybrid and foam samples manufactured for mechanical testing are made of PC foam with 1 wt% of CNT and a density of $0.55\,\mathrm{g{\cdot}cm^{-3}}$.

6.1 Stiffness and strength

6.1.1 Flexural rigidity

Both three- and four-points bending tests are widely used to characterize the mechanical response of panels that are essentially designed to resist bending. The four-points bending test has the advantage to produce a pure-bending zone in-between the internal loading points (Figure 6.1). Outside this zone, the panel is loaded in shear and bending.

From Zenkert [7], the displacement δ_F, at the loading point in a four-points bending test configuration is given by

$$\delta_F = \frac{F(L-l)^2(L+2l)}{48}d + \frac{F(L-l)}{4}f \tag{6.1}$$

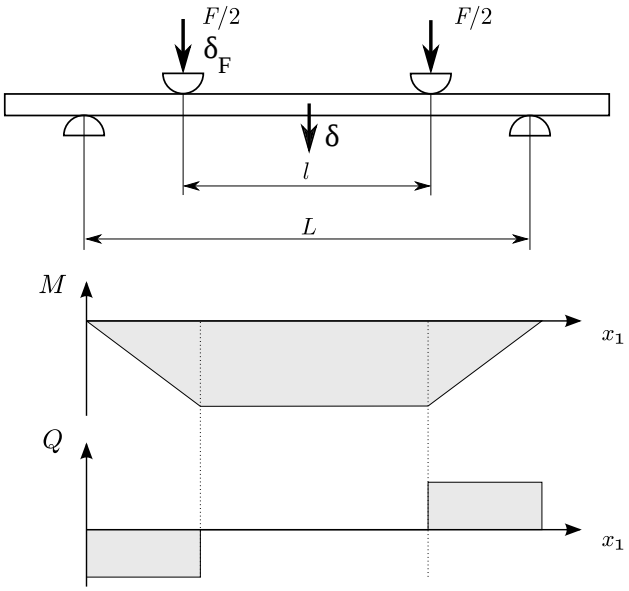

Figure 6.1: *From [8], four-points bending test setup. The load is share on the two loading points. The upper and lower span length are respectively l and L. Variations of the bending moment M and the transverse force Q along the beam for a four-points bending test. δ_F is the displacement at the loading point and δ is the displacement at the centre of the beam.*

while the displacement at the center of the beam is given by

$$\delta = \frac{F(L-l)(2L^2+2Ll-l^2)}{48}d + \frac{F(L-l)}{4}f \tag{6.2}$$

where d is the flexural compliance and f is the shear compliance of the panel under test. Indeed, a four point bending test, involves both bending and shear deformation.

For a homogeneous beam of thickness h and width b, d and f are given by

$$d = \frac{1}{EI} = \frac{12}{bh^3E} \tag{6.3}$$

$$f = \frac{1}{AG} = \frac{1}{bhG} \tag{6.4}$$

with E the flexural modulus G the shear modulus, I the moment of inertia and A the cross section area.

For a sandwich beam with faces of thickness t_f and core of thickness t_c, EI is the sum of three contributions, see equation (6.5). The first one is the flexion of the faces around their own neutral axis. The second is the flexion of the two faces around the neutral axis of the sandwich and the last one is the flexion of the core around its own neutral axis. If the faces are thin compared to the overall thickness and the core much weaker than the faces, the first and the third contributions can be neglected:

$$d = \frac{1}{E_{eff}I} = \frac{1}{\frac{E_f b t_f^3}{6} + \frac{E_f t_f b (t_f+t_c)^2}{2} + \frac{E_c b t_c^3}{12}} \approx \frac{2}{E_f t_f b (t_f + t_c)^2} \tag{6.5}$$

with E_f and E_c the flexural modulus of the face and core, respectively

In a sandwich construction, the shear load is, if the faces are thin, entirely supported by the core. In this case the shear compliance f is given by

$$f = \frac{1}{AG_{eff}} \approx \frac{t_c}{G_c b (t_f + t_c)^2} \tag{6.6}$$

with G_c the shear modulus of the core.

From equation (6.1), the compliance of the specimen, is given by

$$S_F = \frac{(L-l)^2(L+2l)}{48} d + \frac{(L-l)}{4} f \tag{6.7}$$

if the displacement of the loading point is used or it is given by

$$S = \frac{(L-l)(2L^2+2Ll-l^2)}{48} d + \frac{(L-l)}{4} f \tag{6.8}$$

if the deflection at the center of the beam is used.

A series of four points bending test has been performed with a mechanical testing machine ZWICK of 250 kN capacity both on the hybrid and sandwich beams in order to determine the flexural rigidity. The

displacement at the center of the beam, δ, is measured with an extensometer. The length of the beam is 150 mm and the width is around 25 mm for the foam and 45 mm for the hybrid core (which represents the size of 5 cells). The span lengths for the testing setup are 50 mm for l, and 100 mm or 120 mm for L. If sandwich panel is replaced by an homogeneous beam, neglecting the displacement due to transverse shear load, the corresponding equivalent flexural modulus, E_{eq}, can be extracted from [7]:

$$\frac{\partial \delta}{\partial F} = S = \frac{(L-l)(2L^2+2Ll-l^2)}{48}\frac{1}{E_{eq}I} \tag{6.9}$$

with I equal to the second moment of area. S is calculated with a linear fit of the force-deflection curve between 0.65 and 1 mm deflection.

The sandwich configurations for the four-points bending tests are summarized in Table 6.1. Not all the combinations involved in Table 6.1 have been tested. Only the overlined conditions have been addressed.

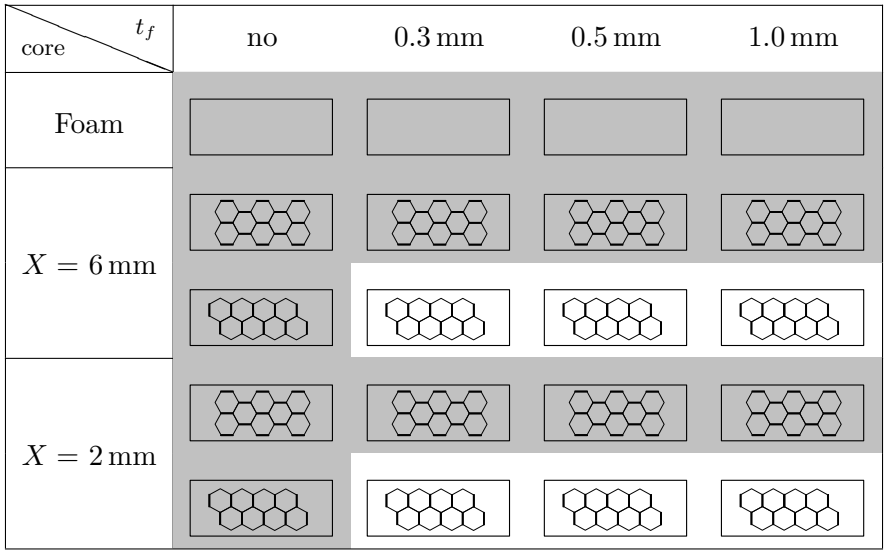

Table 6.1: *Overview of the sandwich configurations for the bending tests, core and face sheets thickness t_f, with overlining on the one effectively tested.*

Foam and hybrid

All the foam and hybrid beams prepared for the tests are 7.7 mm thick. All the beams have been tested in four-points bending with loading point spacing of l =50 mm and L =100 mm.

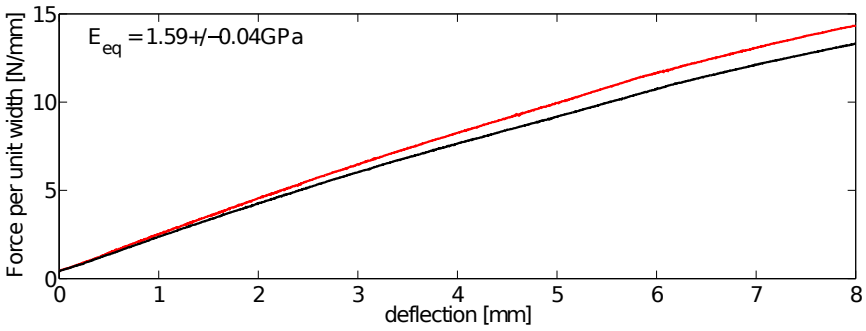

Figure 6.2: *Variation of the force per unit width as a function of the deflection of foam panels under four-points bending with l =50 mm and L =100 mm.*

Figure 6.2 shows the force per unit width as a function of the deflection of foam panels. The panels are 25.5 mm wide. The bending modulus is equal to 1.59±0.04 GPa

Two sizes of honeycomb cell for the hybrids have been tested, one is X = 2 mm, Figure 6.3, and one is X = 6 mm, Figure 6.4. The panel width is equal to 25.5 and 50 mm for X = 2 and 6 mm, respectively. For each of them, two orientations of the honeycomb inside the beam have been considered, one with the double walls of the honeycomb parallel to the long edge of the beam, and the other one with the double walls perpendicular to the long edge of the beam.

Compared to the foam, hybrids are more stiff thanks to the presence of the honeycomb. With no surprise, the equivalent bending modulus, E_{eq}, is dependent on the honeycomb orientation. The stiffness is higher, when the double walls are oriented in the longitudinal direction. The upper and lower bounds for the approximation of the stiffness (see section

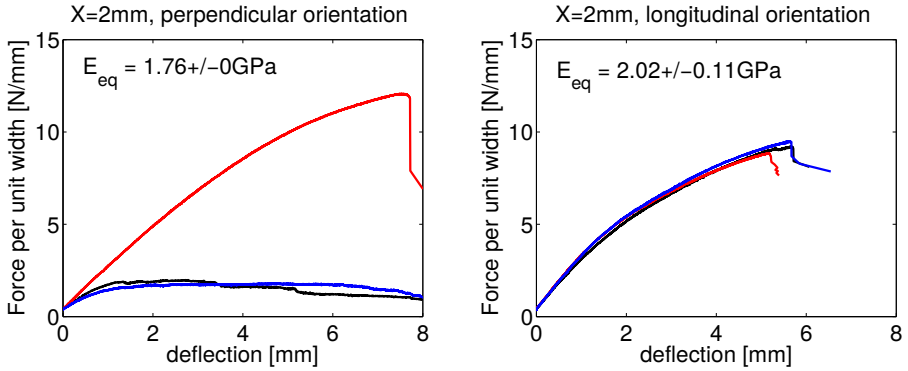

Figure 6.3: *Variation of the force per unit width as a function of the deflection of hybrid panels with $X = 2\,mm$ in four-points bending with $l = 50\,mm$ and $L = 100\,mm$.*

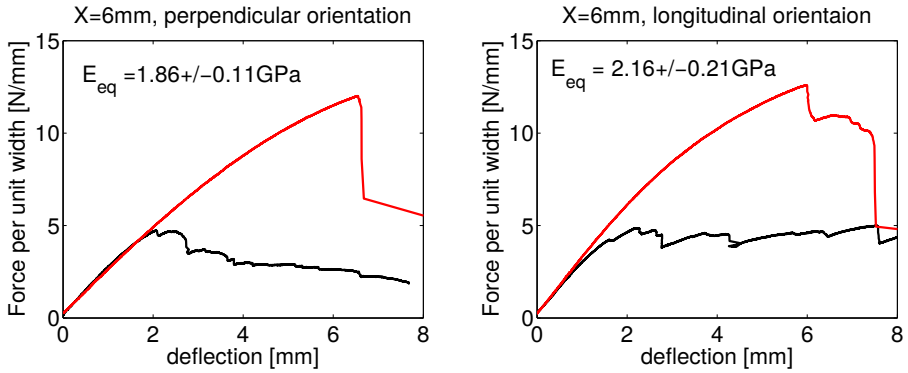

Figure 6.4: *Variation of the force per unit width as a function of the deflection of hybrid panels with $X = 6\,mm$ in four-points bending with $l = 50\,mm$ and $L = 100\,mm$.*

2.1.2) of the hybrid panel are $E_{up} \approx 4.04\,\text{GPa}$ and $E_{low} \approx 1.66\,\text{GPa}$, for $X = 6\,\text{mm}$, and $E_{up} \approx 5.26\,\text{GPa}$ and $E_{low} \approx 1.69\,\text{GPa}$ for $X = 2\,\text{mm}$. The first observation is that the stiffness is close to the lower bound, no matter of the honeycomb orientation. The second observation, is that the honeycomb with $X = 2\,\text{mm}$ should be slightly stiffer than with $X =$

6 mm. But with small cell size, the honeycomb involves more defects, which result in a less align hexagonal pattern.

Sandwich

Figure 6.5 shows the equivalent flexural modulus as a function of the face thickness for test carried on sandwich panels with a foam core or an hybrid with $X = 6\,\text{mm}$. The lower span length for the test was set to 100 mm (triangle dot) or 120 mm (circular dot). As expected, using an hybrid core improves the rigidity of the panel over a foam core. This increase can be attributed to the higher shear modulus of the core. Indeed, generally in sandwich panel, the flexural load is carried by the faces whereas the transverse shear load is carried by the core.

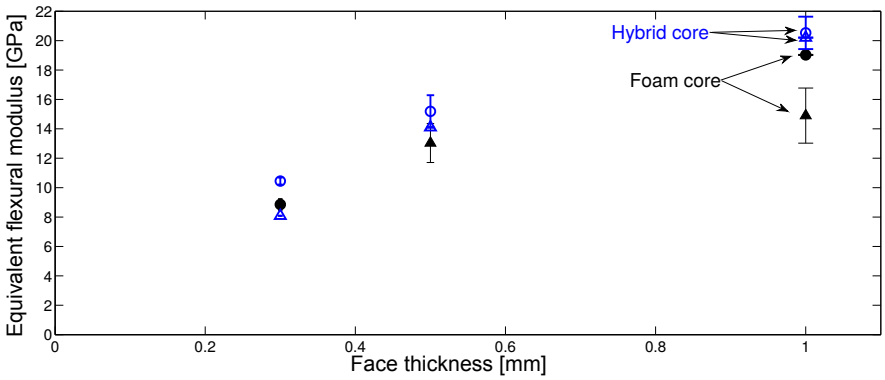

Figure 6.5: *Equivalent flexural modulus as a function of the face thickness for a span length of 100 mm (triangle dot) or 120 mm (circular dot).*

The non ideality of the processing and the error in the measurements combined to a low contribution of the shear deflection have not allowed the use of the analytical analysis to extract the shear modulus of the hybrid core from the experimental measurements. The reason is most probably that the shear deflection is very small and the procedure involving somehow subtracting a large quantity from an other large quantity is inaccurate.

6.1.2 Compression

The combination of the foam and honeycomb provides high crushing resistance. The hybrid, the foam and the honeycomb without the glass fiber reinforced polymer faces have been tested in compression, using an universal mechanical testing machine ZWICK (max loading 250 kN). All samples have a diameter equal to 24 mm. The initial height is 6 mm for the hybrid (inset of Figure 6.6), 7.64 mm for the foam and the 7 mm for the honeycomb. A load of 200N is applied before testing. Figure 6.6 shows the corresponding engineering stress-strain curves. Loading/unloading cycles are applied while deforming the honeycomb and the foam. The hybrid shows a higher crushing resistance, equal to 10.8 MPa, compared to the foam (6 MPa) or honeycomb (5.5 MPa). Even after the buckling of the honeycomb walls in the hybrid, the crushing strength is 30 to 40% higher than the strength of the foam. Postmortem analysis (Fig 6.7.a and b) shows a buckling mode with smaller wavelength in the hybrid compared to the honeycomb alone, in agreement with the analysis of reference [63].

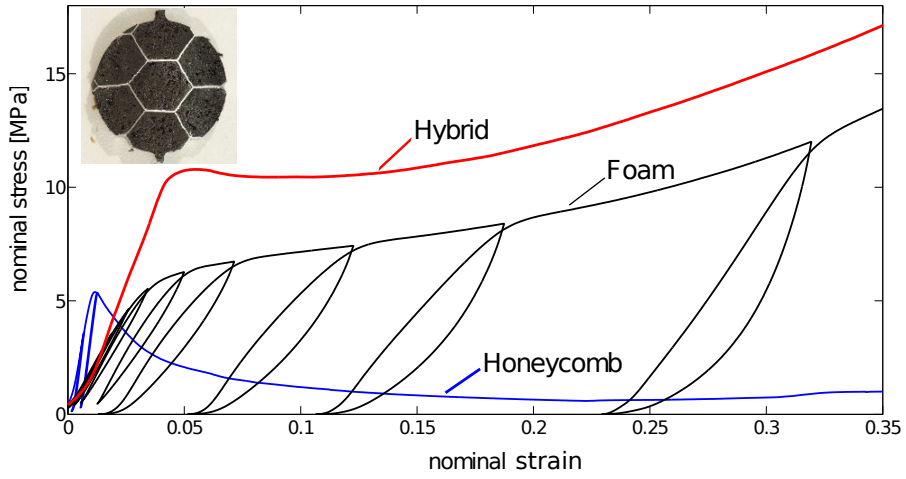

Figure 6.6: *Engineering stress-strain curve, inset is the hybrid sample*

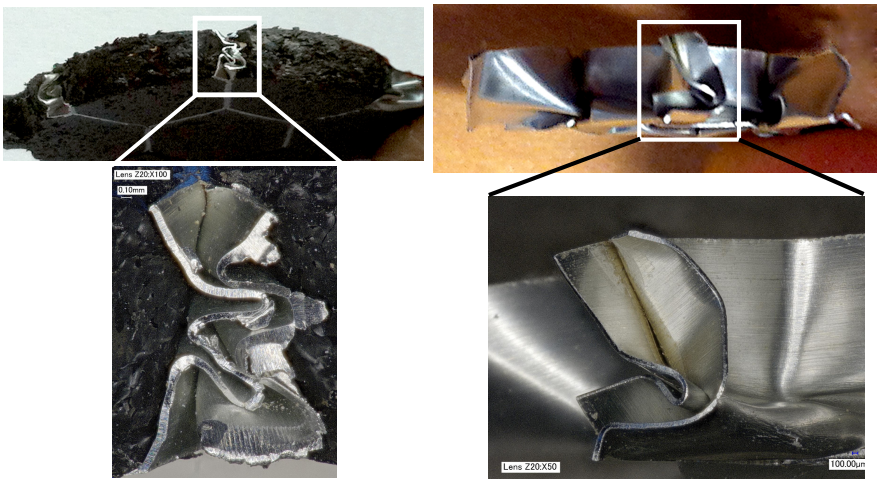

(a) (b)

Figure 6.7: *a) lateral view of the hybrid after the compression* $\varepsilon = 0.61$*, b) lateral view of the honeycomb after the compression,* $\varepsilon = 0.48$

This demonstrates a true effect on the compression strength where the small increase in density associated to the honeycomb is more than compensated by the increase in compression strength.

6.2 Fracture

6.2.1 Flexural failure

Hybrids

Figure 6.3 and 6.4 show that some panels involve early sign of failure. The reason is that the mould used for processing the panel is slightly higher than the honeycomb height which is equal to 7 mm. As a result, a thin layer of foam is presents on one or on the two sides of the panel. If this layer is present on the side which is undergoing tension during the

test, it will prevent the decohesion of the foam from honeycomb. The failure of the panel is then delayed.

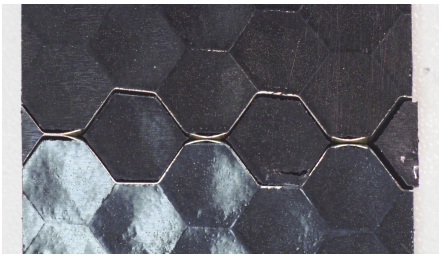

(a) double wall oriented perpendicularly to the direction of the beam.

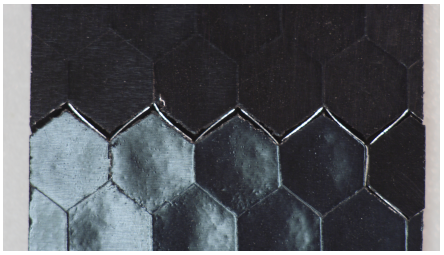

(b) double wall oriented in the longitudinal direction of the beam.

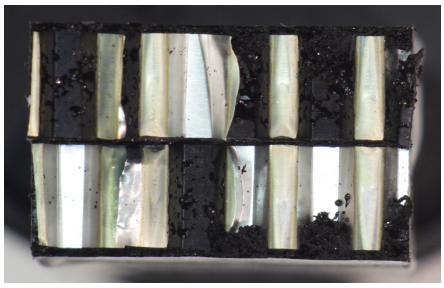

(c) double wall oriented perpendicularly to the direction of the beam.

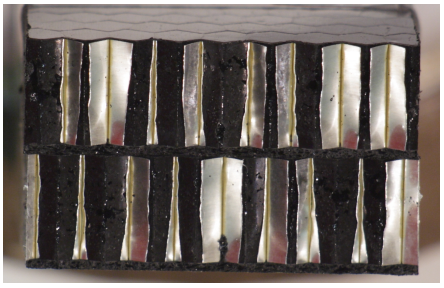

(d) double wall oriented longitudinal to the direction of the beam.

Figure 6.8: *The rupture of the hybrids depends on the orientation of the honeycomb. (a, b) $X = 6\,mm$ (c, d)$X = 2\,mm$*

Figure 6.8 shows how fracture proceeds in the hybrid. The common starting point of the rupture is the decohesion of the foam with respect to the honeycomb cell wall. Depending on the orientation, the following consist of either the fracture of the aluminium along the junction between the simple and the double wall for the longitudinal orientation, or the debonding of the double wall for the perpendicular orientation.

Sandwich

The variation of the force per unit width as a function of the deflection of the four-points bending tests carried on sandwich panels are shown in Figure 6.9. The solid line corresponds to a span length of 100 mm and the dashed line corresponds to a span lenght of 120 mm. The non-linear part of the cure at high load comes from plastic shear banding and/or from the failure of the faces under the loading point. The non-linear part is emphasized when the lower span length is equal to 100 mm.

Depending on the sandwich configuration, different failure mechanisms occur. For panels with a foam core, indentation of the skin under the loading points is observed for all skin thicknesses. At high load, a clear shear deformation band develops in the foam between the upper and lower loading points. Sandwich panels with an hybrid core show several fracture modes. For 1 mm thick faces, fracture essentially occurs in the shear loaded part of the beam. It is due either to the debonding of the faces from the core or to the decohesion of the foam from the honeycomb wall as shown in Figure 6.10. For 0.5 mm thick faces, most panels fail by the indentation of the faces under the loading point. Other panels fail by shear collapse as for thicker faces.

Sandwich panels involving 0.3 mm thick sheets essentially fail by face indentation. But some panels have failed also in the pure bending zone. The failure is illustrated in Figure 6.11. Here, the crack starts from the bottom face, goes through the core and finally follows the interface between the foam and the glue. In the hybrid, the path of the crack has a tendency to follow the interface of the foam and the honeycomb wall but also to propagate inside the foam. The final aspect of the crack is similar to the one of Figure 6.8.

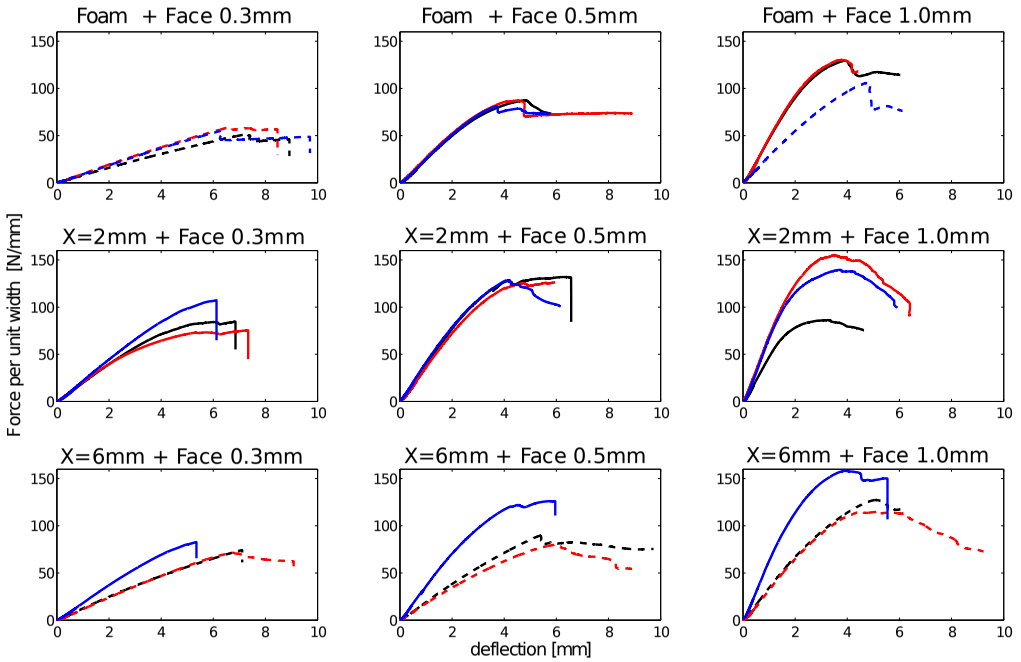

Figure 6.9: *Variation of the Force per unit width as a function of the deflection of sandwich panels. The first row shows the response with a foam core, the second and third rows the response with a hybrid core, $X = 2\,mm$, and $X = 6\,mm$, respectively. The first column shows the response with 0.3 mm thick faces, the second 0.5 mm thick, and the third 1 mm thick. Bending tests have been carried with a lower span length of 100 mm (solid line) or 120 mm (dashed line).*

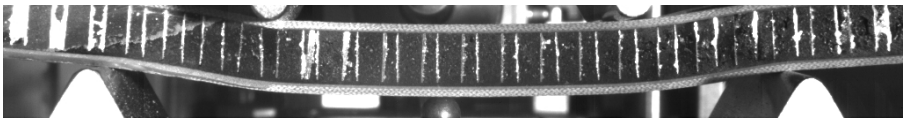

Figure 6.10: *Shear fracture of the core for a sandwich sample with 1 mm thick faces and honeycomb cell size of 2 mm*

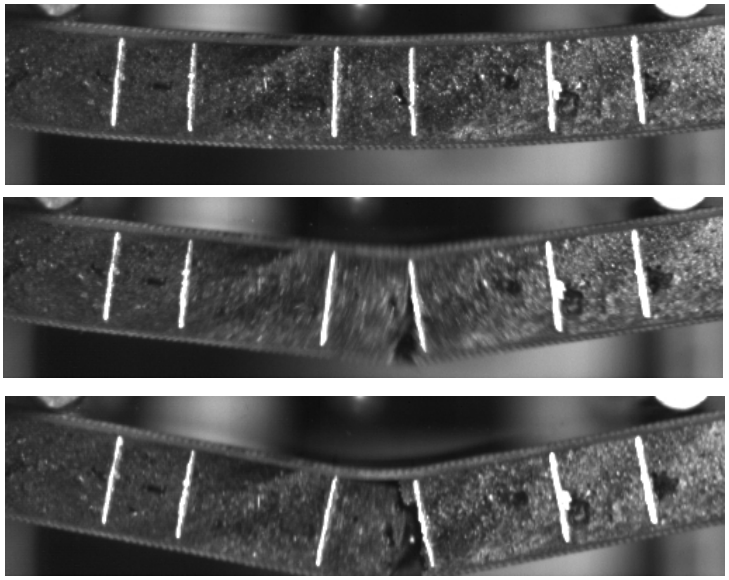

Figure 6.11: *Picture before, during, and after the failure of the sandwich panel with an hybrid core with $X = 6$ mm and 0.3 mm thick faces. The time interval between the pictures is 1/10 000 s.*

6.2.2 Impact resistance

Low speed impact tests have been carried out on the hybrids and on the sandwich panels. The test machine is a Instron Dynatup 9250 HV. The head of the impactor is hemispherical with a 12 mm diameter. The brittle-ductile behaviour of a material during an impact can be qualitatively characterized by the force as a function of the time curves, see

Figure 6.12.

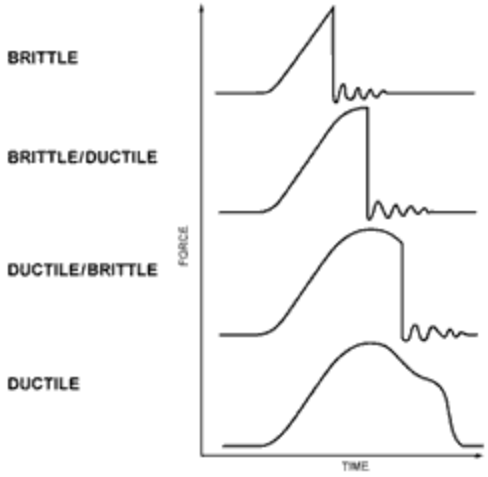

Figure 6.12: *From [64], idealized response force the time response curve for various brittle/ductile material behaviour during an impact test.*

Foam or hybrid panel

Pictures of the impact zone are shown in Figure 6.13. The energy stored in the panel and variation of the load as a function of time are presented in Figure 6.14.

The load time curve of the foam panel reveals a ductile/brittle behaviour. The probable damage history in the panel is the following. At the early stage of the impact, the foam is crushed under the impactor head until radial cracks suddenly propagate. The cracks propagate until almost complete unloading of the panel. At this point the panel is again loaded until it gives rise to a smooth propagation of the cracks. The energy dissipated by the foam is less than 20 J. The remaining energy has probably been absorbed by the anti-rebound system of the machine.

The hybrid panels do not exhibit a brittle behaviour. The failure mechanism, in this case, is associated to the honeycomb. Its presence has

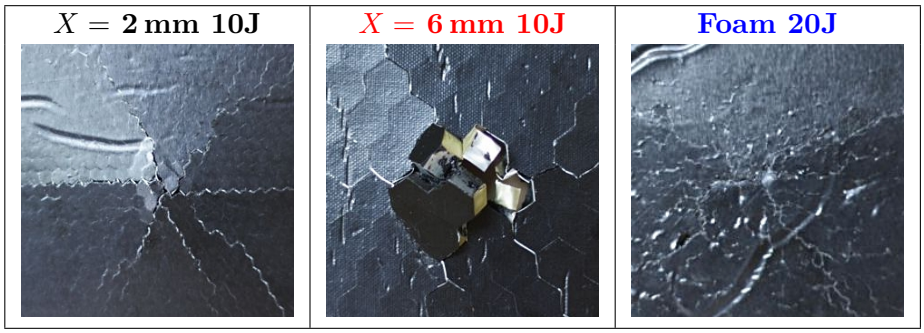

Figure 6.13: *Pictures of the bottom side of low speed impacts on foam or hybrid panels. The energy of the impact is 20 J for foam and 10 J for hybrid.*

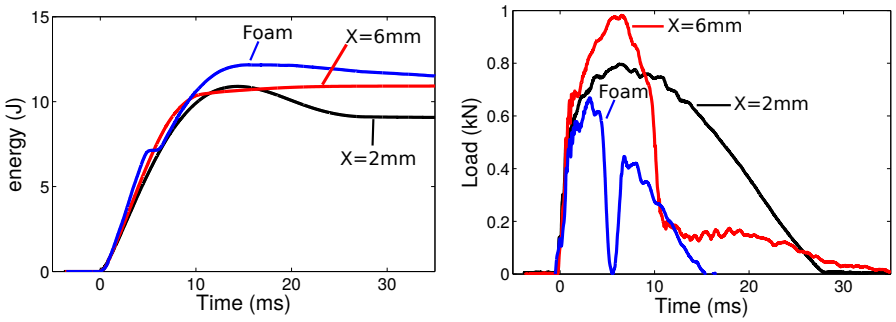

(a) (b)

Figure 6.14: *(a) Energy stored and (b) evolution of the force as a function of time in foam or in the hybrid panels during low speed impact. The impact energy is 20 J for the foam and 10 J for the hybrids.*

segmented the foam which cannot react as a whole homogeneous system. During the impact, the low adherence between the foam and the honeycomb does not allow the foam to significantly deform and dissipate energy. Instead, it is the honeycomb that absorbs the impact energy. It

does by the debounding of the double walls or cracks along the junction of single and double wall, the failure is similar as in flexion (see Figure 6.8). On the back side of the panel, cracks develop in the form of debonding between the foam and the honeycomb.

The hybrid made of honeycomb with a cell size equal to 2 mm has better impact performances thanks to a higher honeycomb density ($0.13\,g{\cdot}cm^{-3}$ versus $0.09\,g{\cdot}cm^{-3}$ for 6 mm) and a cell size much smaller than the impactor characteristic dimension. The panel is not perforated and the damaged zone is smaller compared to the cell size equal to 6 mm.

Sandwich panels

Three sandwich panels with 0.5 mm thick face but involving different 7mm thick cores, have been impacted at 50 J with a low speed impactor (Instron dynatup 9250HV machine). The diameter of the steel impactor is equal to 12 mm. The top and bottom faces of the impacted panel are shown in Figure 6.15 whereas the absorbed kinetic energy and the force seen by the impactor as a function of time is plotted in Figure 6.16.

Only the foam core and hybrid core allow the absorption of the impact. The load-time curve gives more insight about the behaviour of the panels. The top face of the sandwich with the honeycomb core, has been penetrated at a load of 3kN quickly followed by the bottom face. The honeycomb has opposed little resistance to the impactor. The damaged zone is barely larger than the impact tip diameter. With the foam core, the panel fails at a load of 7 kN, at this load, a crack has propagated through the core and the faces. After the first failure, some delamination and/or crack propagation occur. The final crack at the back is equal to 85 mm. The analysis of the hybrid panel is more complicated due to a combination of several failure modes. A 3D tomography image of the impacted zone obtained with a Tomohawk system, see figure 6.17, shows that the foam in the cell under the impactor has been pushed out leading to a wide debonding of the bottom face. Moreover, the cross section views of Fig.6.17.S1 and 6.17.S2 show the multiple folding of the honeycomb walls and the tearing of the foam in the cell under the im-

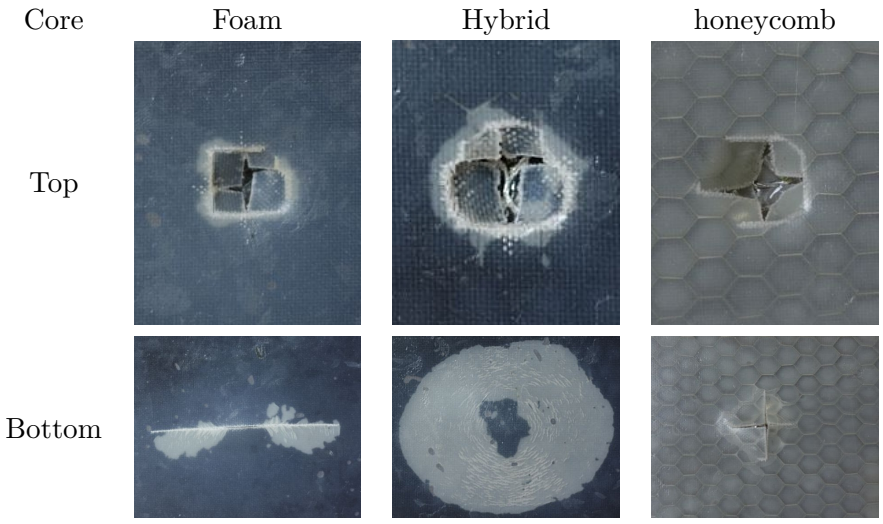

Figure 6.15: *Low speed impact of 50J on sandwich panels made of 0.5mm GFRP face sheets and 7mm thick core. Pictures of impacted sandwich, 1st row is a zoom in of the top face and the 2th row shows the bottom face.*

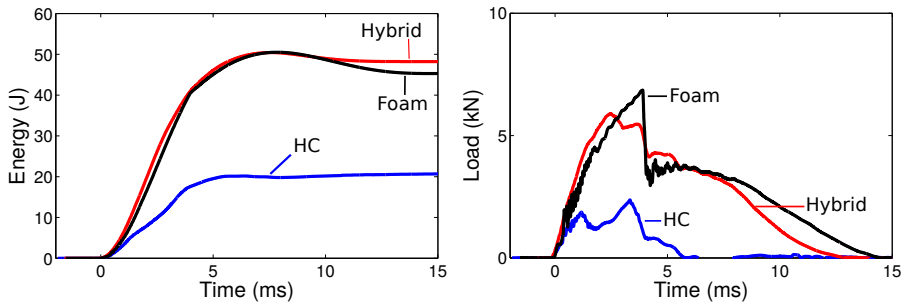

Figure 6.16: *Variation of the absorbed energy and of the force on the indent as a function of time.*

pactor head. These two mechanisms dissipate a lot of energy and keep the damage in the honeycomb localized, see the 3D view Fig.6.17.a.

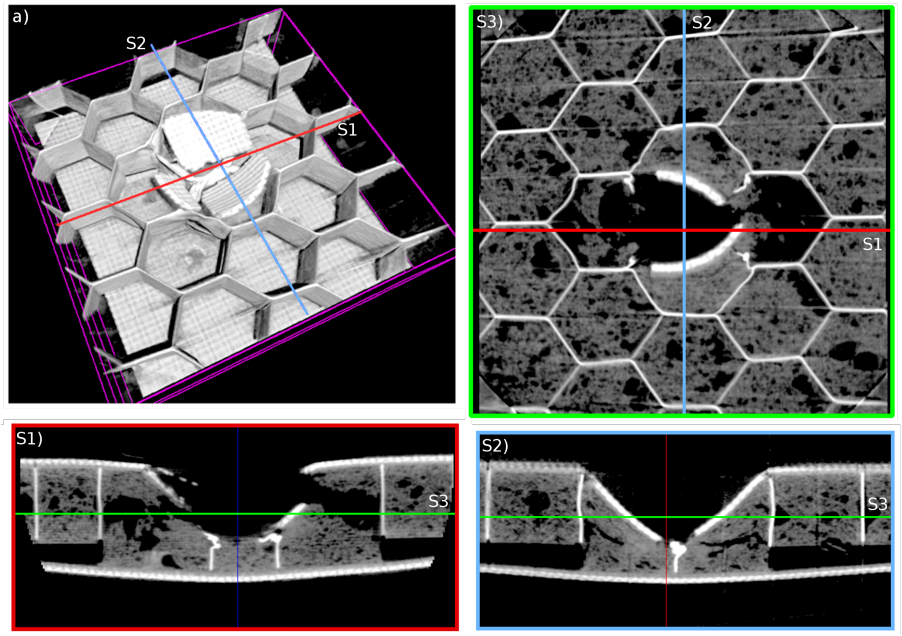

Figure 6.17: *CT scan of the sandwich panel made of 0.5mm GFRP faces sheets and 7mm thick hybrid core impacted at 50J: a) 3D view of the bottom half of the sandwich (foam is not shown), S1) vertical cross section, S2) vertical cross section, S3) horizontal cross section*

6.3 Conclusion

In this chapter, mechanical characterisation has been carried on the foam, on the hybrid and on sandwich panels with both foam and hybrid core. Regarding the elastic bending stiffness, the presence of the honeycomb provides an increase of the stiffness compared to foam panel. For panels without face sheets, the increase of bending stiffness is due to a higher bending modulus but the improvement is close to the lower bound of the composite approximation. For sandwich panels, the improvement comes from a higher shear modulus as the bending contribution of the core is low in this configuration.

In case of crushing, the honeycomb also plays a positive role. The pres-

ence of the honeycomb increases the energy needed to crush the core, and the presence of the foam leads to a small wavelength buckling mode in the honeycomb wall, by increasing even more the energy needed to crush the core.

The failure strength of hybrid panels is highly limited by the low cohesion between the foam and the honeycomb, especially during bending and impact. This is a point to address in future researches. During impact, foam panels have a more brittle-ductile response. The addition of the honeycomb segments the panel and prevents the propagation of large cracks. But because of the low cohesion, the foam does not participate any more to the energy absorption. The presence of face sheets vastly increases the dissipation capability. The crushing of the foam and of the honeycomb becomes possible and energy is also dissipated by the debonding between the core and back face. Compared to a sandwich with a foam core, the hybrid core prevents the cracking of the back face at the cost of a wider debonding area.

Chapter 7

Multifunctional design

The aim of this chapter is to provide a first design approach for a panel with the minimum possible mass or overall thickness under the constraint of attaining a specified level of bending stiffness, S^*, and of electromagnetic absorption, A^*, at a frequency f^*. The values of A^*, f^* and S^* are set by the application. The design requirements, expressed in terms of constraints, objectives, free variables and fix variables, are listed in table 7.1.

Function	Light or thin stiff beam for EM absorption
Constraints	Absorption index $A > A^*$ at frequency f^* Stiffness of the beam $S > S^*$
Objectives	Minimize the mass and/or the thickness, and/or maximize operating bandwidth
Free variables	core thickness, t_c, face sheet thickness t_f, size of hexagon, X, foam density, ρ
Fixed variables	skin and HC material, polymer matrix, CNT content, HC wall thickness and orientation, symmetric sandwich construction, wave polarisation

Table 7.1: *Design requirements*

Because increasing the performance of a function A often means decreasing the performance of a function B, multi-functional materials are made to reach compromises, see Chapter 2, section 1. As a preliminary step toward the optimization of the system for specific applications, the sensitivity of the design variables will be analysed by creating a set of sandwich configurations from a multi-dimensional grid of the design variables. Each candidate will be numerically tested and only candidates passing the constraints are kept. In order to illustrate what would be the optimum configuration, the lightest or the thinnest configuration is selected among the potential candidates.

7.1 Search for the best candidate

The algorithm followed to find candidates fulfilling the constraints is shown in Figure 7.1. For each set of variable (skin thickness, t_f, foam density, ρ, and honeycomb size, X), the core thickness, t_c, is increased until the specified absorption index is achieved for a given frequency f^*. If it is not possible to attain A^* due to a reflection which is to high, the candidate is rejected. This is done thanks to the analytical model developed in Chapter 4. To fulfil the mechanical requirement, the thickness of the core needed to achieve a given stiffness is linearly extrapolated from FE simulations of this configuration, see the right part of Figure 7.1. For each frequency, if the level of absorption required is reached by the candidate, the core thickness that will fulfil both constrains is the maximum between the EM selected thickness and the mechanical selected thickness. Indeed, a core thicker than imposed by the constraint will simply outperform the constraint (EM or mechanical). In the final stage, for each frequency, the configuration which is the thinnest, with the face sheets included, is selected. At this stage, if it is the lightest panel that is looked for, the thickness is converted into mass per surface unit.

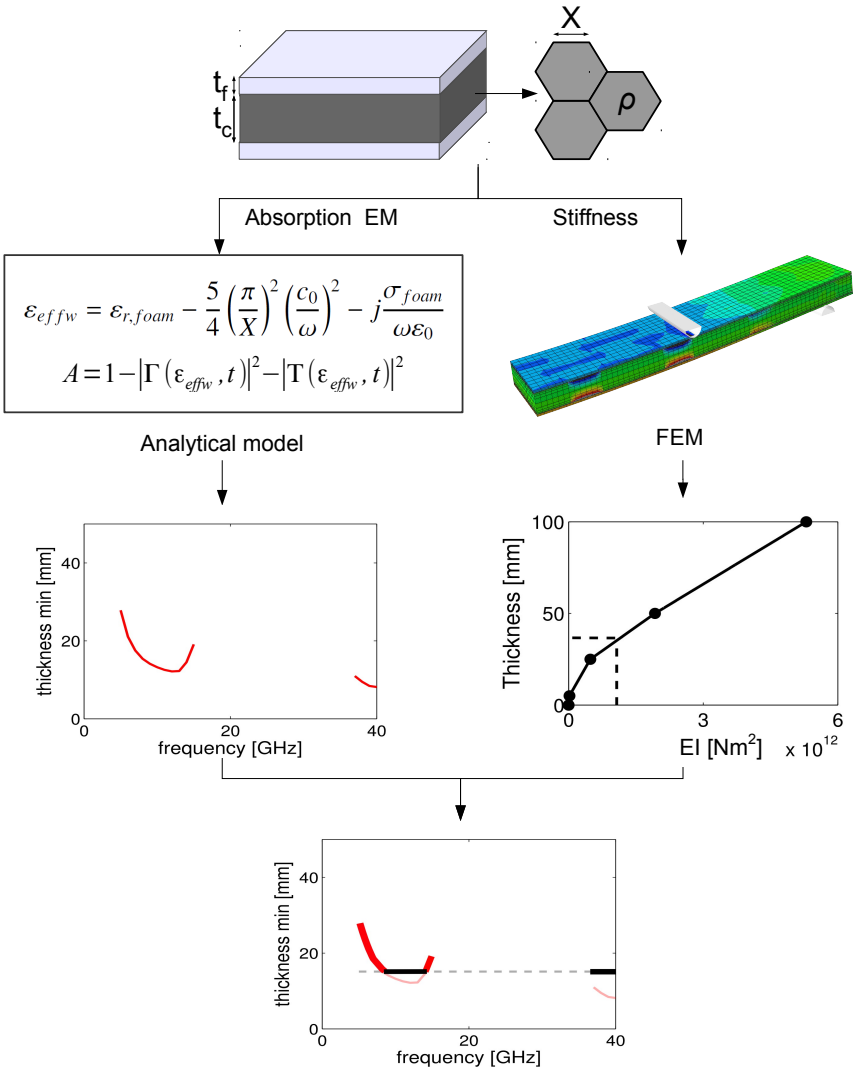

Figure 7.1: *Algorithm followed to design a sandwich configuration at a given absorption index and rigidity. For each possible configuration of the skin thickness, t_f, the foam density, ρ, and the HC size, X, (see top part of the figure) the core thickness, t_c, needed to fulfil the specifications (EM on the left and mechanical on the right) is computed. Then, for each frequency, the maximum of the two thicknesses is chosen (see bottom part of the figure).*

7.2 Electromagnetic absorption

The analytical model describing the behaviour of the panel was presented in Chapter 4. In order to provide data to the model, foam specimens of several densities have been manufactured to experimentally measure the complex permittivity. Polycarbonate (PC Makrolon 2805, Bayer) was used as hosting polymer matrix for the dispersion of 1wt% multiwalled carbon nanotubes (Nanocyl^{TM} NC 7000, 90%) and 7.5wt% chemical foaming agent (Hydrocerol HK40B, Clariant). 7 mm thick foams were prepared using a mould introduced in a Fontijne press working under 15 tons. The nanocomposite powder was poured into the honeycomb cells. The amount of powder was calculated to reach a foam density of 0.2, 0.3, 0.4, 0.5, and 0.6 g·cm^{-3}.

The measured dielectric constant, ϵ_{foam}, and the conductivity, σ_{foam}, are shown in Figure 7.2. For each foam density, an exponential fit has been applied for use in the design analysis.

The EM characteristics of a glass fiber reinforced E-glass/Epoxy sheet (SI403240, Goodfellow) has also been measured. The conductivity is close to zero and the dielectric constant is around 4.2 .

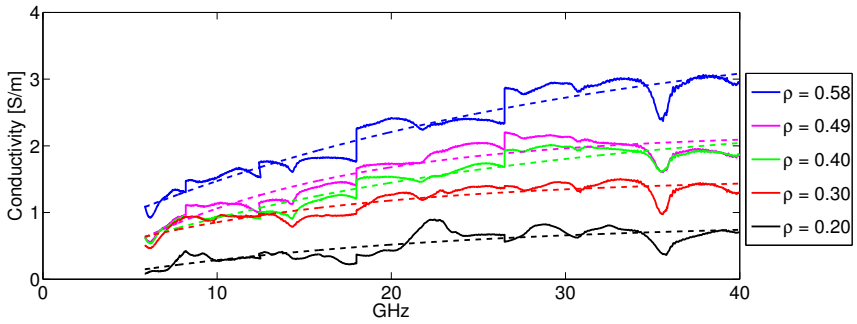

(a) Conductivity, straight line is experimental measurement, dash line is the fit.

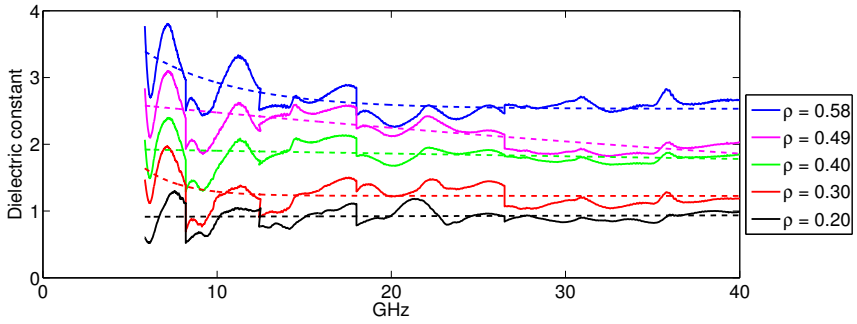

(b) Dielectric constant, straight line is experimental measurement, dash line is the fit.

Figure 7.2: *Electrical characterization of the PC foam with 1wt% of CNT for density, ρ equal to 0.2, 0.3, 0.4, 0.5, and 0.6 $g{\cdot}cm^{-3}$*

7.3 Bending Stiffness

In order to estimate the flexural stiffness of the panel, fully elastic finite element analysis of the four points bending test has been performed using the software Abaqus. The geometry of the model is the following: the upper span length is set equal to 90 mm and the lower span is set equal to 180 mm, the loading supports are cylinders defined as rigid solid bodies with a diameter of 4 mm. The total length of the beam is equal to 200 mm. The width is adjusted to comprise five honeycomb cells.

The thickness of the honeycomb wall is set equal to 0.1 mm. The double wall of the honeycomb is also included in the model. The orientation of the honeycomb in the core is fixed and corresponds to the double wall being aligned with the long edge of the beam. The meshing is made of quadratic elements. The number of elements is kept constant while the thickness of the core and/or of the skin changes. Only one quarter of the geometry of the panel is modelled for symmetry reasons, as on right part of Figure 7.1. The modelling of a four points bending test by FEM has been selected on purpose. The next development of the design method would be to include non-elastic constraint for example maximum load bearing or impact resistance but this has not been accomplish in the context of this thesis. All materials in the model are linear elastic. The Young's modulus of the face sheets is equal to 10 GPa, the Young's modulus of aluminium honeycomb walls is set to 70 GPa. The bending stiffness of the polycarbonate foam is taken from [3] and is equal to 1.25 GPa for a density of 0.55 g·cm^{-3}. In order to estimate the stiffness of the other foam densities, i.e. 0.2, 0.3, 0.4, 0.5, and 0.6 g·cm^{-3}, the following rule has been applied [4]:

$$E_{foam} = E_{solid} \left(\frac{\rho_{foam}}{1.2} \right)^2 . \tag{7.1}$$

Four core thicknesses (5, 25, 50, and 100 mm) have been simulated in order to compute the thickness needed to achieve the required panel rigidity, EI. The rigidity of the panel is computed with the following equation:

$$EI = \frac{F}{\delta} \frac{(L-l)(2L^2 + 2Ll - l^2)}{48} \tag{7.2}$$

where F is the force acting on the panel at the loading pad, δ is the deflection at the centre of the panel, l is the upper span length and L is the lower span length. With this approach, the shear deformation is not specifically taken in consideration but integrated into an effective EI.

7.4 Sensitivity analysis

7.4.1 Electromagnetic sensitivity

Both the reflection and the transmission need to be kept at low level to maximize A. The absorption index can thus be *reflection limited* and/or *transmission limited*.

If the absorption of the panel is limited by the transmission, the core thickness and/or of the electrical conductivity of the foam should be increased. The electrical conductivity of the foam increases with density.

If the absorption is limited by reflection, the honeycomb cell size needs to be adjusted with respect to the cutoff frequency or the honeycomb should be removed ($X = 0$). The foam density can be reduced to lower the mismatch between the interface and the air. Finally, the thickness of the skin can be adjusted to produce a better match. The optimal skin thickness will depend on the frequency and on the effective EM properties of the hybrid.

The sensitivity of the absorption index, A, relative to the geometric parameters, X, t_c, t_f and to the foam density ρ_{foam} is shown in Figure 7.3, Figure 7.4, and Figure 7.5 for 7 GHz, 15 GHz, 30 GHz, respectively. For each frequency, the lightest candidate attaining 95% of absorption is represented. Each subfigure shows the evolution of the absorption index as a function of one parameter with all the other parameters keeping their nominal value.

At 7 GHz, the most sensitive parameter is the honeycomb cell size. At this frequency, X should be larger than 8 mm to put the panel EM behaviour above the cutoff and to avoid reflection. Lowering the foam density to $0.2\,\mathrm{g{\cdot}cm^{-3}}$ without an increase of the core thickness reduces the absorption capabilities which is then *transmission limited*. The face sheet thickness is not a sensitive parameter at this frequency. As long as the absorption index is limited by transmission, increasing the thickness increases A until a plateau, limited by reflection is reached. As the attenuation of an EM wave in a material is a negative exponential function (see equation (2.42)), the absorption of the last fraction of the EM radiation power requires an exponential increase of the thickness.

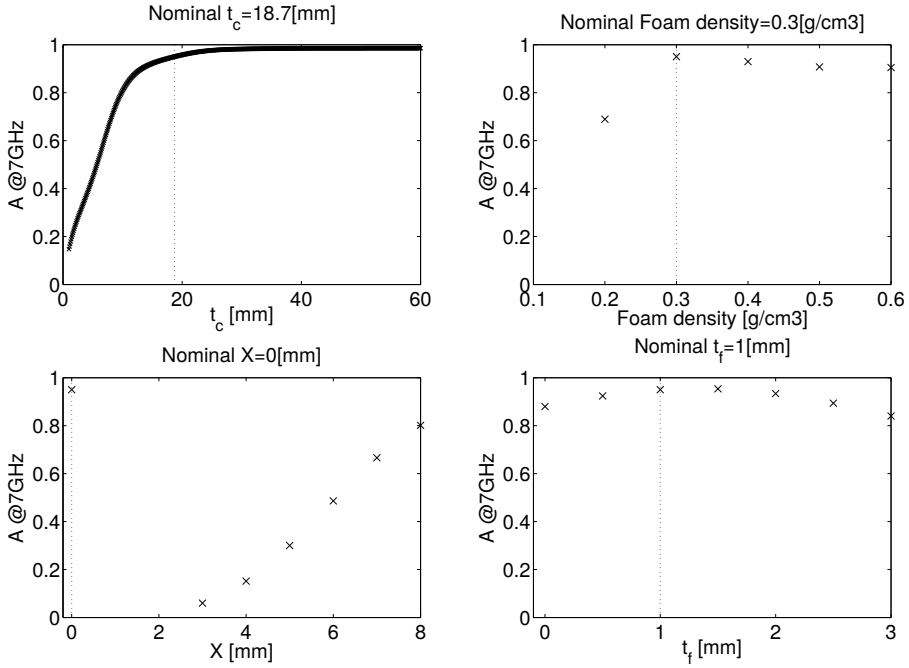

Figure 7.3: *Variation of the absorption index, A, as a function of the geometric parameters, core thickness t_c (top left), honeycomb cell size X (bottom left), face sheet thickness, t_f (bottom right) and of the foam density ρ_{foam} (top right) for the lightest candidate at 7 GHz. The candidate has a core thickness of 18.7 mm, face thickness of 1 mm, no honeycomb $X = 0$ mm and a foam density of 0.3 g·cm^{-3}.*

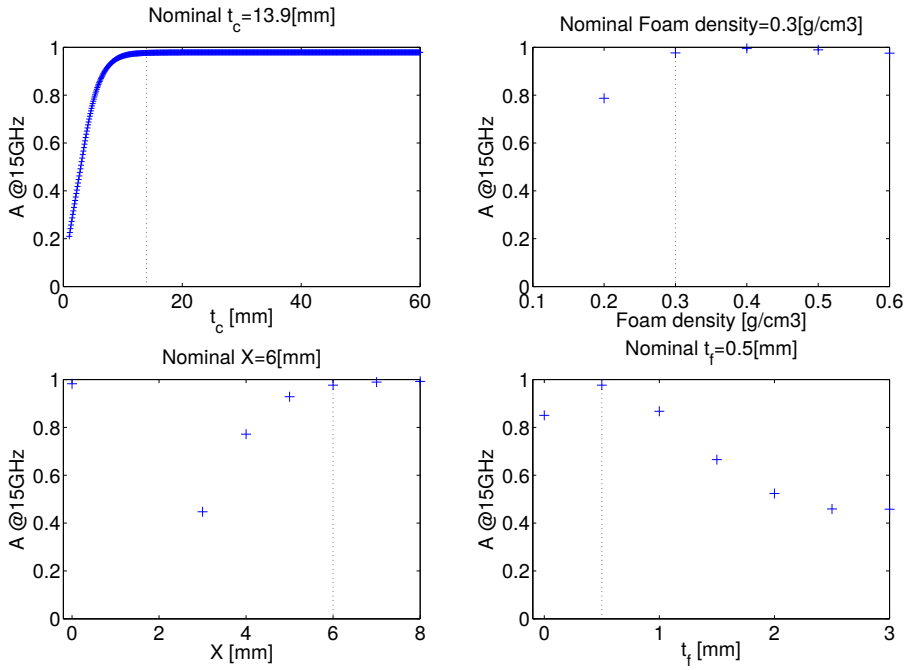

Figure 7.4: *Variation of the absorption index, A, as a function of the geometric parameters, core thickness t_c (top left), honeycomb cell size X (bottom left), face sheet thickness, t_f (bottom right) and of the foam density ρ_{foam} (top right) for the lightest candidate at 15 GHz. The candidate has a core thickness of 13.9 mm, face thickness of 0.5 mm, honeycomb cell size of 6 mm and a foam density of 0.3 g·cm^{-3}.*

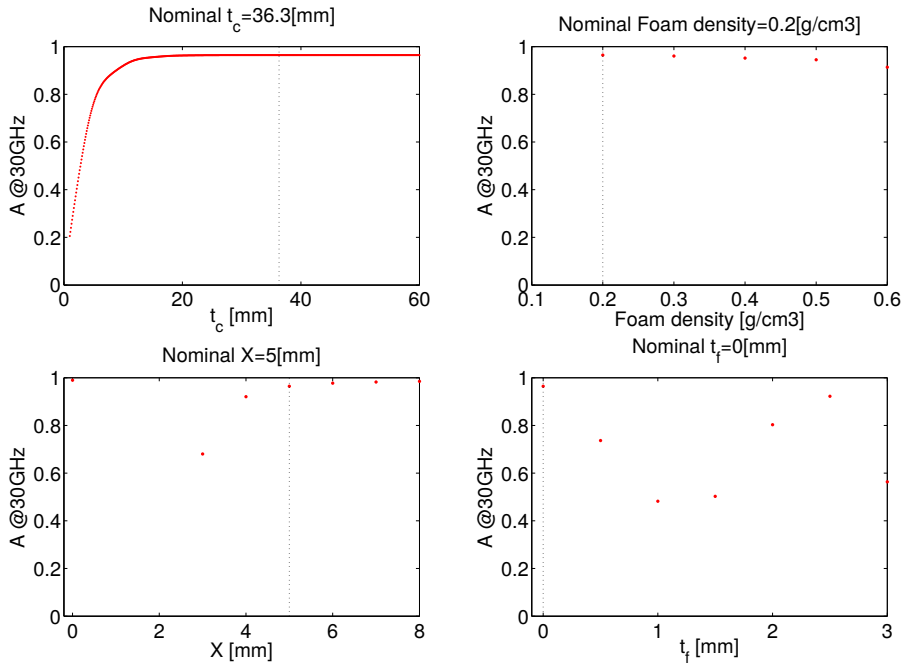

Figure 7.5: *Variation of the absorption index, A, as a function of the geometric parameters, core thickness t_c (top left), honeycomb cell size X (bottom left), face sheet thickness, t_f (bottom right) and of the foam density ρ_{foam} (top right) for the lightest candidate at 30 GHz. The candidate has a core thickness of 36.3 mm, no faces $t_f = 0$ mm, honeycomb cell size of 5 mm and a foam density of 0.2 g·cm^{-3}.*

The face sheet thickness becomes an increasingly sensitive parameter at higher frequencies. For honeycomb sizes with cutoff well below the considered frequency no difference will be found when varying X.

In Figure 7.6, 7.7, and 7.8, the sensitivity of the candidate to the frequency or, in other words, to the bandwidth at which $A > 0.95$ is shown.

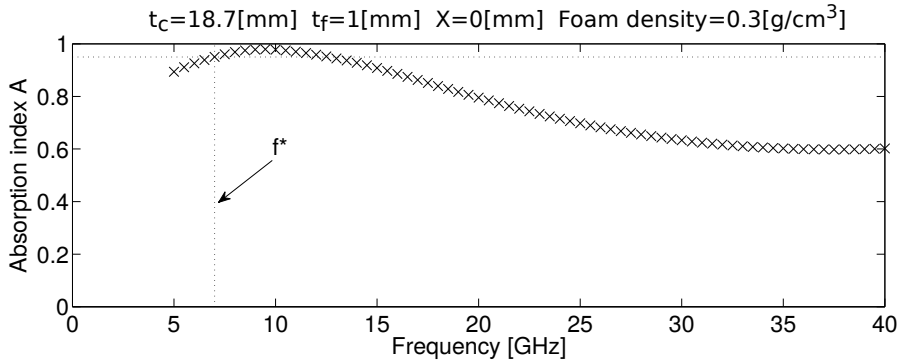

Figure 7.6: *Absorption index as a function of the frequency for the lightest candidate designed with f^* equal to 7 GHz.*

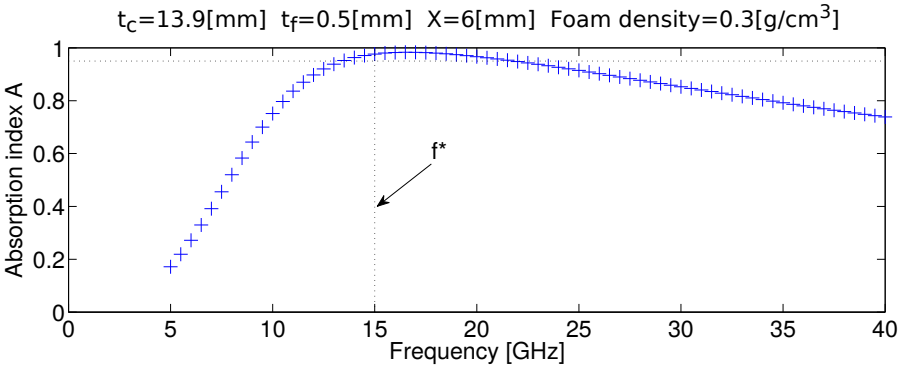

Figure 7.7: *Absorption index as a function of the frequency for the lightest candidate designed with f^* equal to 15 GHz.*

The following observations are general trends and some specific configurations may behave differently. Thick faces strongly reduce the absorption bandwidth. Thicker faces produce a better matching between the

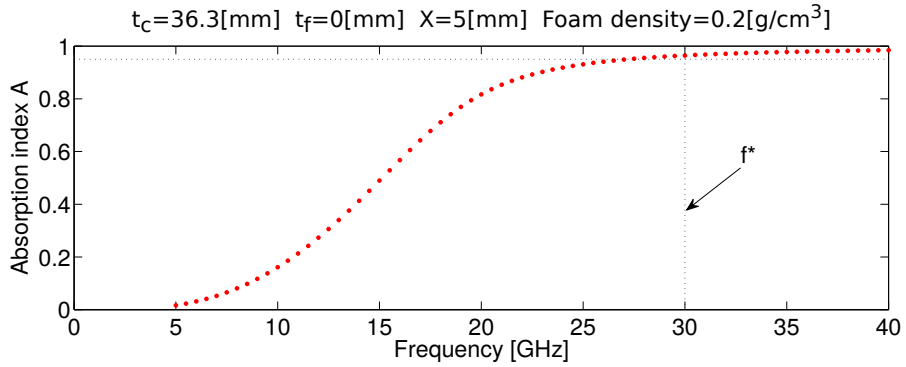

Figure 7.8: *Absorption index as a function of the frequency for the lightest candidate designed with f^* equal to 30 GHz.*

air and the panel which reduces the reflection but this occurs over a narrower band of frequencies. The reflection at non-matched frequencies is larger than without face sheets. A smaller honeycomb cell size also reduces the bandwidth due to the cutoff occurring at higher frequencies. A thick core prevents the absorption to be limited by transmission at lower frequencies and thus helps increasing the bandwidth. It is more difficult to analyse the influence of the foam density on the bandwidth but the use of higher foam densities tends to broaden the matching frequencies of thick face sheet.

7.4.2 Mechanical sensitivity

The sensitivity of the stiffness is shown in Figure 7.9. For sandwich structures, the degree of sensitivity of the different parameters depends of the loading condition. Indeed, the problem can be divided in three domains, which depend of the slenderness of the beam, defined as the span length divided by the panel thickness. If the slenderness is high, bending is the dominant loading mode. As the slenderness decreases, shear loading, will become more and more dominant, especially for sandwich panels. At the extreme, for very thick panels, the indentation under the loading pad will dominate.

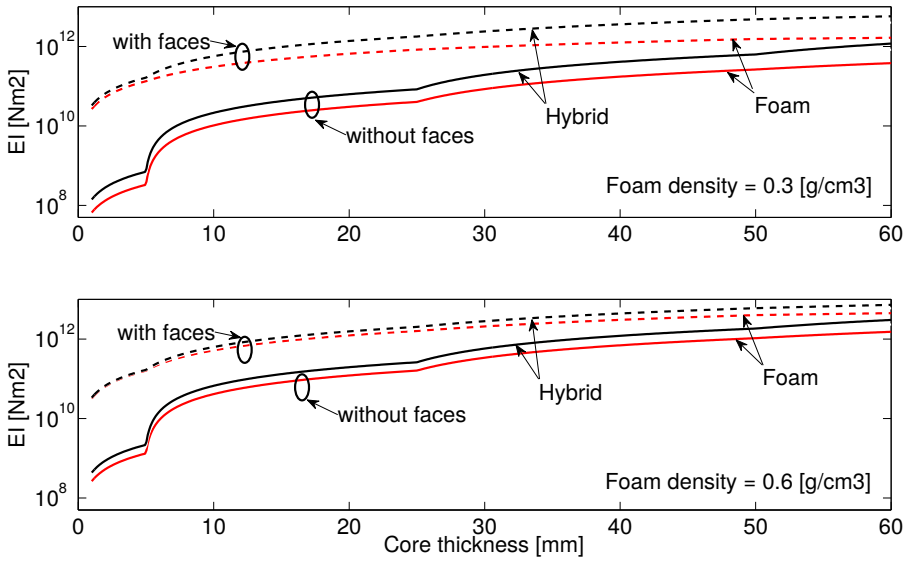

Figure 7.9: *Variation of the stiffness as a function of the core thickness for foam (red line) or hybrid ($X = 2\,mm$, black line) with $3\,mm$ thick face sheets (dashed line) or without face (solid line). Top graph is for a foam density of $0.3\,g{\cdot}cm^{-3}$ and bottom graph is for $0.6\,g{\cdot}cm^{-3}$.*

If bending is dominant, the face sheet thickness is the only sensitive parameter for the sandwich panels. For panels without faces, denser foams or the addition of honeycomb results in a stiffer panel.

When shear becomes dominant, the shear deformation in the core knocks down the overall stiffness of a sandwich panel. If the sandwich is built with a foam core, a denser foam increases the shear modulus of the core. If the core is an hybrid, the shear deformation is mostly carried by the honeycomb. Therefore, smaller honeycomb cells size reduces the impact of the foam density.

Finally, for extremely thick panels, most of the deformation is located under the loading pad. Limiting this deformation can be done by using thicker faces, denser foam or smaller honeycomb cell size.

The graphs of Figure 7.10 show the stiffness divided by the mass of the panel. This approach reveals that for all beam slenderness:

- a sandwich configuration is very effective,
- the added mass coming from the honeycomb is well rewarded in terms of stiffness,
- an increase of the foam density results in lower effectiveness of the sandwich panel.

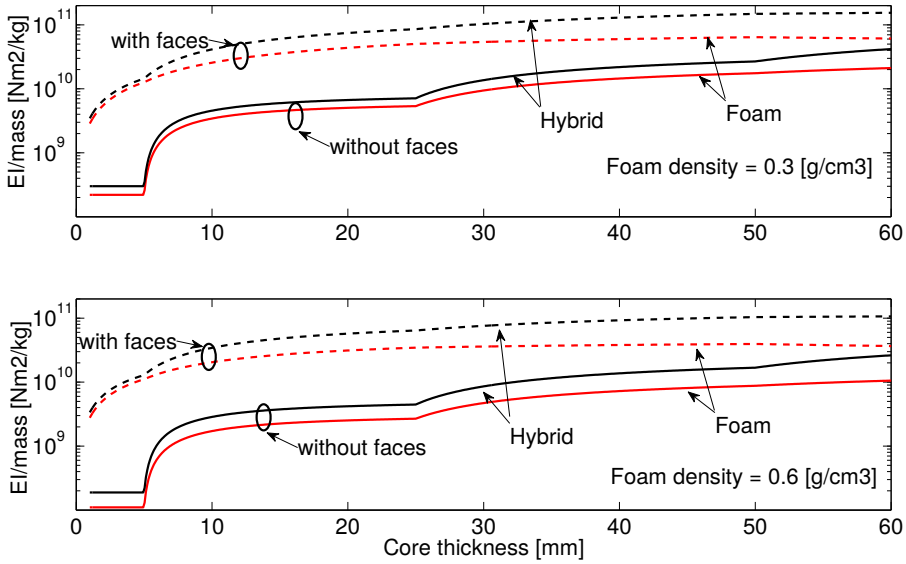

Figure 7.10: *Variation of the stiffness divided by the mass as a function of the core thickness for foam (red line) or hybrid ($X = 2\,mm$, black line) with 3 mm thick face sheets (dashed line) or without face (solid line). Top graph is for a foam density of $0.3\,g{\cdot}cm^{-3}$ and bottom graph is for $0.6\,g{\cdot}cm^{-3}$.*

7.5 Results and discussion

7.5.1 Minimize mass and/or thickness

Figure 7.11 and 7.12 show the configuration (size of hexagon, foam density and face sheet thickness) which gives the minimum thickness or mass per unit surface in order to absorb 95% of EM radiation between 1 and 40 GHz with no requirement on the rigidity in black (cross, '×'), with a rigidity, EI, equal to $1 \times 10^{10}\,\mathrm{N{\cdot}m^2}$ in blue (plus sign, '+') or $5 \times 10^{11}\,\mathrm{N{\cdot}m^2}$ in red (dots, '.'). The foam density vary from 0.2 to $0.6\,\mathrm{g{\cdot}cm^{-3}}$ by step of $0.1\,\mathrm{g{\cdot}cm^{-3}}$, the hexagon size from 0 (no honeycomb) to 8 mm by step of 1 mm, and the face sheet from 0 to 3 mm by step of 0.5 mm.

In order to minimize the overall thickness, without requirement on the rigidity, the use of the most dissipating medium, in other word, the higher foam density, is mandatory. But this goes along with high reflection. The later can be reduce thanks to the adequate size of hexagon and face sheet thickness at each frequency. Because the face sheet does not absorb any EM radiation, the thinnest face sheet giving the best matching needs to be selected to keep the overall thickness low. If the panel must be rigid, the thickness of the core is the maximum between what is required to absorb the EM power and what is required to attain the specified rigidity. In this case, the gain in flexural rigidity added by thicker face sheets might be an option to greatly reduce the core thickness.

To minimize the mass, if there is no requirement on the rigidity, the best solution avoids non-absorbing element like the honeycomb and the face sheets and keeps the foam density low. If the rigidity of the panel have to be taken in account, the best solution takes advantages of thicker faces, and of the honeycomb. Indeed, the shear modulus and the bending modulus of the core is increased by the presence of the honeycomb.

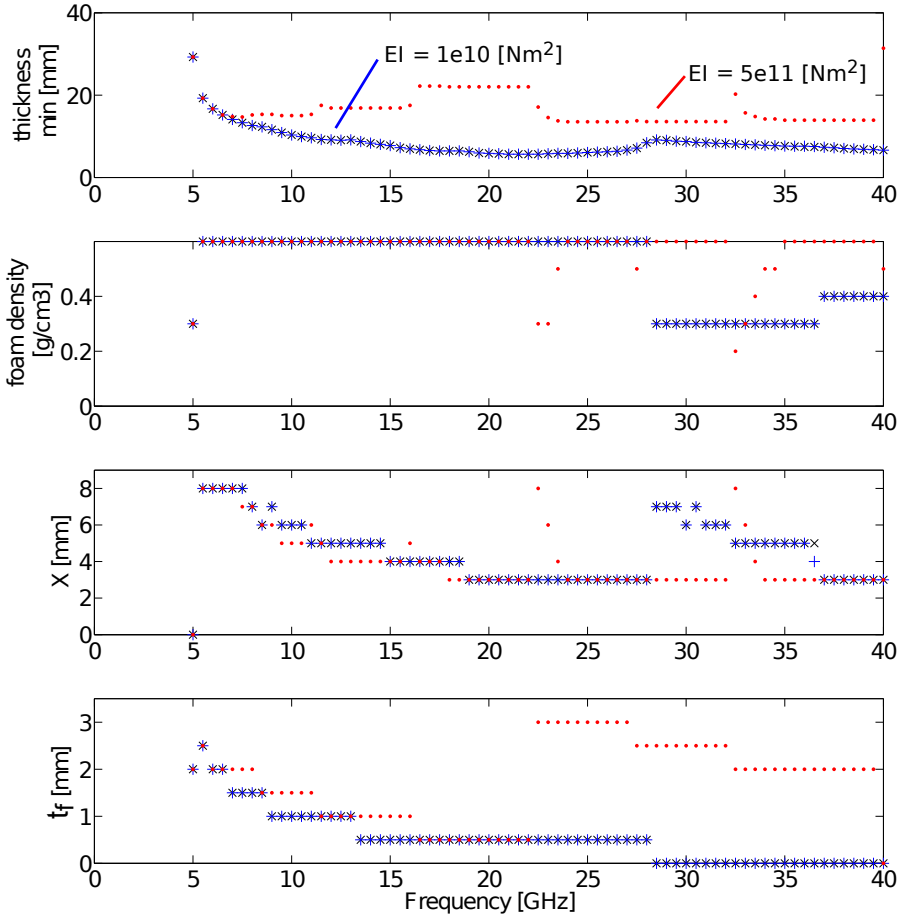

Figure 7.11: *Total minimum thickness and corresponding configuration of the thinnest candidate able to absorb 95% of the incoming EM signal as a function of the frequency with either no requirement on the rigidity, (black crosses), a rigidity equal to 1×10^{10} N·m^2 (blue plus sign) or 5×10^{11} N·m^2 (red dots). From top to bottom, graphs give the total thickness (core+faces), foam density, honeycomb cell size, and the face sheet thickness.*

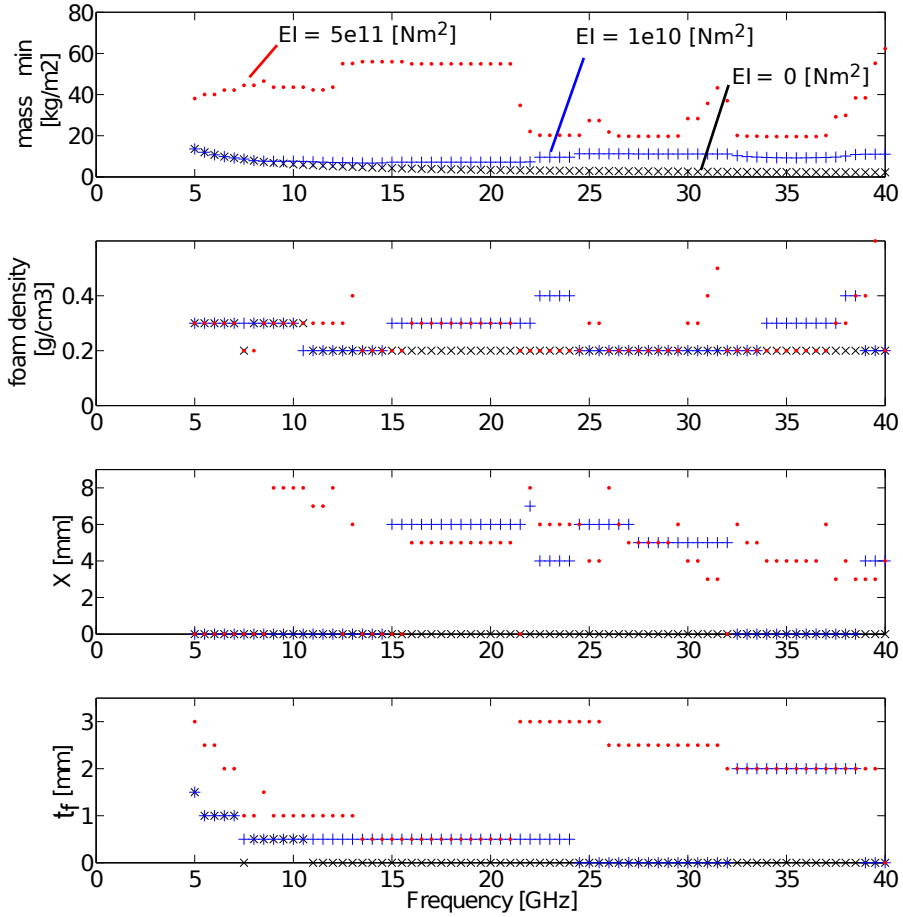

Figure 7.12: *Minimum mass per unit area and configuration of of the lightest candidate able to absorb 95% of the incoming EM signal as a function of the frequency with either no requirement on the rigidity, (black crosses), a rigidity equal to 1×10^{10} N·m^2 (blue plus sign) or 5×10^{11} N·m^2 (red dots). From top to bottom, graph give the mass, foam density, honeycomb cell size, and the face sheet thickness.*

Figures 7.13, 7.14, and 7.15, show the trade off between thin or light panel at 7 GHz, 15 GHz, and 30 GHz, respectively. For each, a hand-drawn qualitative envelope of the best candidates is shown as a guide for the eyes.

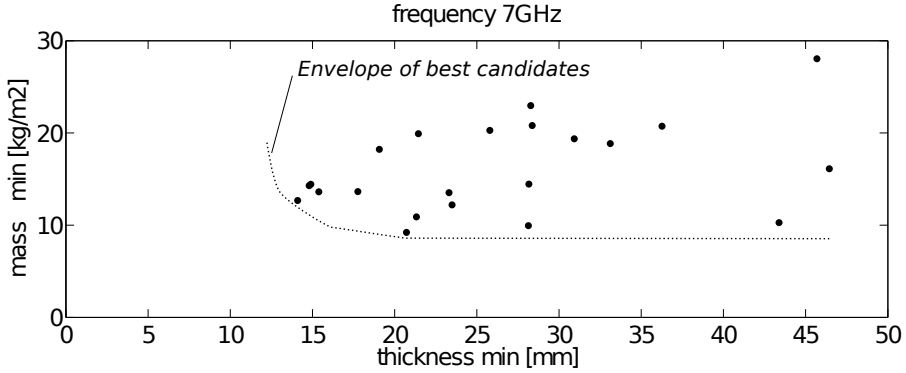

Figure 7.13: *Trade off between thin or light panels that absorb 95% of the EM signal at 7 GHz with a stiffness higher than* 1×10^{10} $N{\cdot}m^2$.

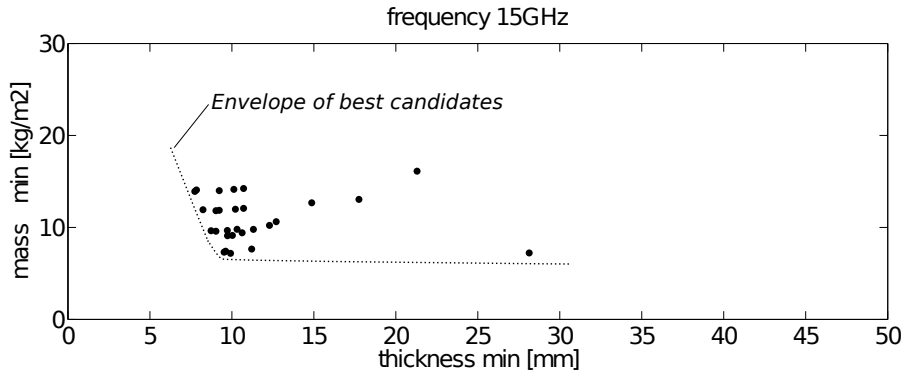

Figure 7.14: *Trade off between thin or light panels that absorb 95% of the EM signal at 15 GHz with a stiffness higher than* 1×10^{10} $N{\cdot}m^2$.

At 7 GHz, in Figure 7.13, the candidates are spread out, even if the sensitivity of the absorption to the design parameter is low (except for the honeycomb size). Indeed, at this frequency, reducing the reflection

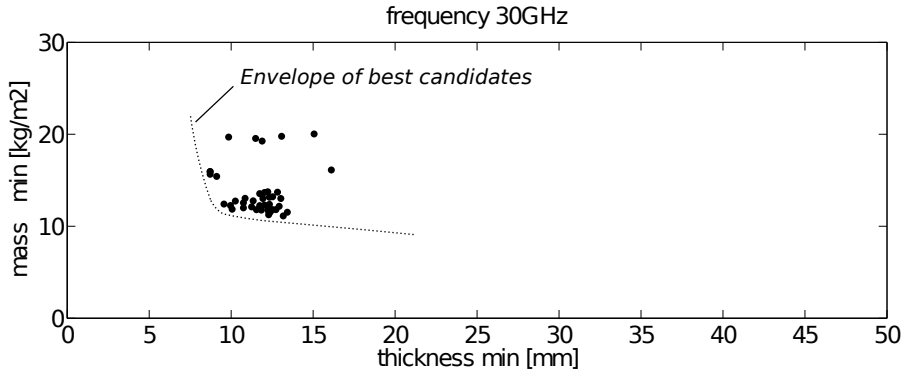

Figure 7.15: *Trade off between thin or light panels that absorb 95% of the EM signal at 30 GHz with a stiffness higher than* $1 \times 10^{10}\ N{\cdot}m^2$.

below 5% is not easily achieved so the transmission needs to be close to zero to compensate the reflection. This can be done by increasing the thickness of the core. But to absorb the very last fraction of EM radiation in the material, the thickness must be exponentially increased as the attenuation is an negative exponential function. So a small increase of the reflection translates into a large increase of the core thickness to compensate.

At higher frequencies, the attenuation factor, $\gamma = j\omega\sqrt{\mu\epsilon}$ (see equation (2.43)), is larger meaning that the energy is absorbed more rapidly as the wave travels into the material. Also, the sensitivity when the honeycomb cell size is large is low. As a result, candidates which differ only by the honeycomb cell size posses similar thickness and mass.

7.5.2 Maximization of bandwidth

The two key parameters analysed here are the width and the position of the centre of the bandwidth. Figure 7.16, 7.17, and 7.18 show on the *x-axis* the shift of the bandwidth centre with respect to f^* and on the *y-axis* the inverse of the bandwidth. The best candidate will be as close as possible to the origin of the graph.

Because the analysed frequencies are comprised between 5 and 40 GHz, combining a very wide band centered on 7 GHz is impossible. This explains why wideband candidates are off-centre in Figure 7.16.

At higher frequencies, it is possible to extend a little the bandwidth toward low frequencies by increasing the core thickness. If the low end of the bandwidth is limited by the transmission, the increase of t_c will compensate for the lower attenuation factor.

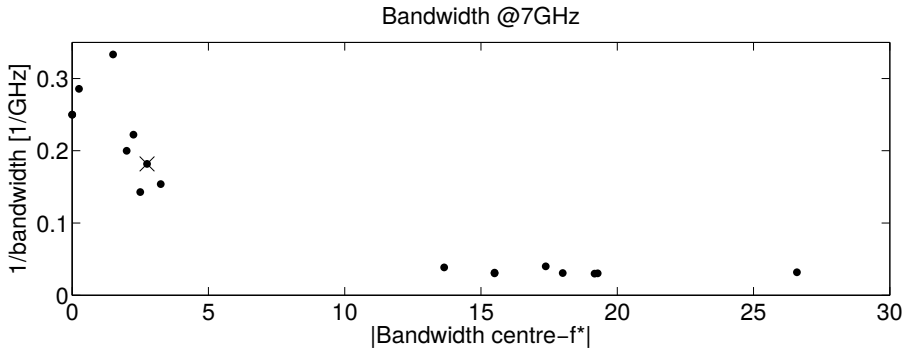

Figure 7.16: *x-axis is the shift of the bandwidth centre with respect to f^* and y-axis is the inverse of the bandwidth for candidates at 7 GHz*

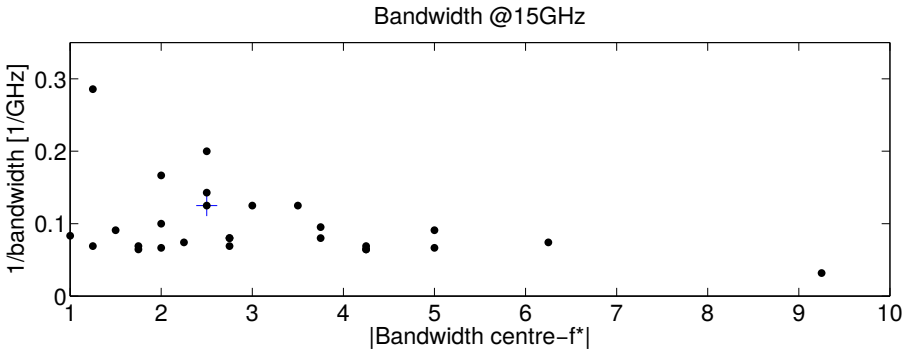

Figure 7.17: *x-axis is the shift of the bandwidth centre with respect to f^* and y-axis is the inverse of the bandwidth for candidates at 15 GHz*

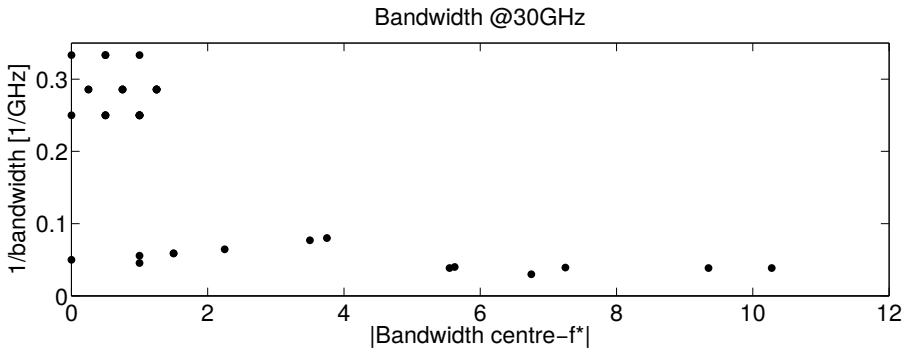

Figure 7.18: *x-axis is the shift of the bandwidth centre with respect to f^* and y-axis is the inverse of the bandwidth for candidates at 30 GHz*

7.6 Conclusion

A design tool has been proposed to select the best sandwich configuration of a sandwich that meet constraints both on the EM absorption level over a specified bandwidth and on the bending stiffness. The sensitivity analysis has revealed that the minimization of the mass of the panel is not trivial. With the EM absorption constraint, the best solution is to avoid non-absorbing elements like face sheets and honeycomb. While the best solution for enhancing the stiffness involves the presence of face sheets and of the honeycomb. The final compromise must be made based on the application. The minimization of the panel thickness is on the contrary more trivial as both the face sheets and honeycomb reduce the reflection of the EM signal by providing a better matching between the air and the panel. The lower reflection drastically reduces the thickness needed to attain the required absorption. The different panel designs are robust to variation of the parameters. As a consequence, the specified absorption level is achieved over a wideband of frequencies.

Thanks to the use of FE simulations, this designing tool can directly be extended to other types of mechanical constraints, for example maximum load bearing, or impact resistance provided that the proper constitutive relationships are used.

Chapter 8

Applications

This chapter is divided in two parts. In the first part, applications where the hybrid panel might be of interest are presented. In the second part, some of these applications have been assessed with our new material.

8.1 Potential applications

8.1.1 Cost per square metre of the hybrid

Because all the constituents used to manufacture the hybrid are already available at industrial scale, the material price of the hybrid is relatively low. Typical prices are 3 €/kg for polycarbonate, 100 €/kg for carbon nanotubes and 40 €/m^2 for aluminium honeycomb. The composite foaming cost can be approximate as equal to 4 €/kg and includes the foaming agent and energy. In order to absorb radiation in the X-band (8-12 GHz), the hybrid configuration is 10 mm thick with a foam density of 0.6 g·cm^{-3} and 1 wt% of CNT. The raw material cost per square meter is 48 € of composite foam and 40 € of honeycomb.

8.1.2 Stealth wind turbine

Renewable source of energy are in the front line to get rid of fossil energy. One of them is the wind energy which is transformed into electrical energy thanks to wind turbines. One issue with wind turbines is their reflectivity that can perturb radar detection of airplane nearby airport. For this reason a security perimeter is set up around airport where no wind turbine might be build. In some countries, this reduces drastically the ground surface available. Stealthy wind turbine will simplify their introduction into the existing radar detection network. For such an application, Radar Absorbing Material (RAM) must operate in harsh environment induced by bad weather conditions, including temperature and humidity variation, as well as shocks induced by the impact of various objects under wind storm. These requirements are met by our hybrid solution. Its technical integration into the fabrication process of the wings of the turbine will be the next key challenge to meet. Another concern is the resistance of the hybrid to lightning strike. The conductive path provided by the metallic honeycomb should prevent the total perforation of the sandwich panel [65]. But, the outer skin can be damaged as it has to be non conductive to allow the absorption of the radiation by the core of the sandwich.

8.1.3 EM interference shielding and EM pollution reduction

Electromagnetic interferences (EMI) are nowadays a major concern to preserve the operation of sensitive electronic devices and systems. EMI protection can be achieved by using a Faraday cage to shield the device against external radiations or to confine unwanted radiations. Confinement may lead to internal interferences which can be avoided by the use of EM absorbers. They can also be used to reduce EM pollution. For example, in today's typical military ship [66], the topside environment is a complex electromagnetic conglomeration of radar, navigation, communications, fire control, and electronic warfare systems all trying to operate simultaneously in an extremely small area. Due to high output power requirements, overlapping operating frequencies, and sensitive receiver requirements, numerous interoperability problems can occur

among shipboard systems. RAM can be deploy on ship structures such as masts, yardarms, and bulkheads, see Figure 8.1, to provide isolation between source and victim equipment, to increase antenna-to-antenna decoupling, and to reduce false targets.

Figure 8.1: *From [66], X-Band RAM Installation on USS Ronald Reagan (CVN 76) Stubmast Showing New (Black) Tile*

One of the biggest requirements is, in the case of this application, the easy maintainability and high durability. Indeed, RAM might be placed on structures difficult to access during ship operation. The hybrid presents some advantages over the available RAM on the market, they are lightweight, broadband, durable, water resistant and it can be paint to match the ship colour.

8.1.4 Bird strike shield for airplane

For safety reason, every airplane posses a radar operating in the X-band (8-12 GHz) for weather, collision avoidance and ground proximity

among other. This radar is located in the nose cone of the airplane and is protected by a radome as shown in Figure 8.2. The radome which is not as strong as the hull of the plane, is exposed to bird strike. In this event, probability of radome breakage is high. Critical devices and cockpit are then protected by a shield situated behind the radar. The shield also isolates pilots and critical devices from the high power radiation of the radar.

Figure 8.2: *Nose cone configuration of a plane*

Today's solution for this shield in civil airplane is an 118 mm thick full aluminium sandwich panel which is pictured in Figure 8.3. The front face sheet is 2.4 mm thick, the rear face sheet is 0.8 mm thick and the core is made of aluminium honeycomb.

The use of the multifunctionnal sandwich panel developed in this thesis might improve the solution is several aspects: room saving thanks to thinner shield, weight saving and reduction of radar interferences due to the absorption of the multi-reflection inside the radome. The resistance of the sandwich to lightning strike has to be investigated such as the wind turbine application.

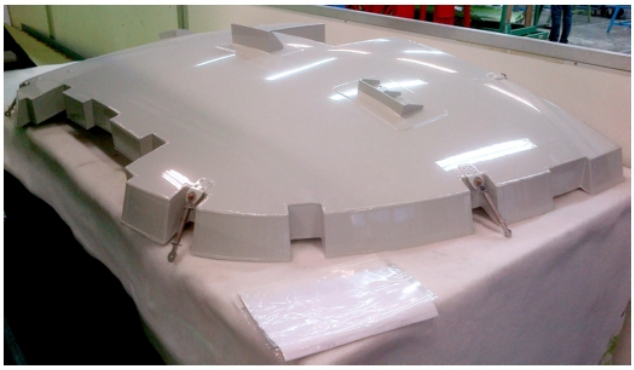

Figure 8.3: *Full aluminium shield of a civil plane.*

8.2 Exploration of some applications

8.2.1 WiFi shielding Box

Six 7 mm thick hybrid panels have been assembled by bounding to form

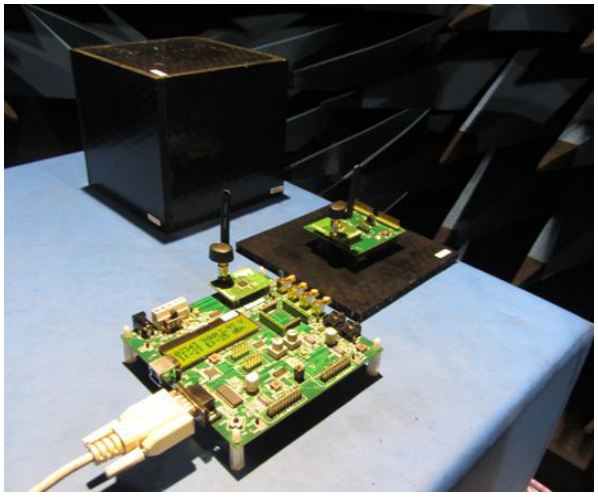

Figure 8.4: *Shielding box assembly from hybrid panel and the transmitter/receiver pair using the Zigbee protocol for the measurement of the shielding effectiveness of the box.*

the cube in Figure 8.4. The panels are made of honeycomb with 6 mm cell size filled with polycarbonate reinforced with 1wt% of CNT foamed to a density equal to 0.55 $g \cdot cm^{-3}$.

The shielding effectiveness (SE) of this box has been measured thanks to a transmitter-receiver, shown in Figure 8.4, using the Zigbee protocol. This protocol is based on the norm IEEE 802.15.04. The band of frequencies used is comprised between 2.4 and 2.48 GHz which is well below the cutoff frequency of the hybrid situated around 10 GHz. The shielding of the box is thus achieved by a reflection mechanism.

Measurements have been performed inside an anechoic chamber. The measurement set-up is shown in Figure 8.5. The distance between the transmitter and the receiver varies from 20 to 300 cm.

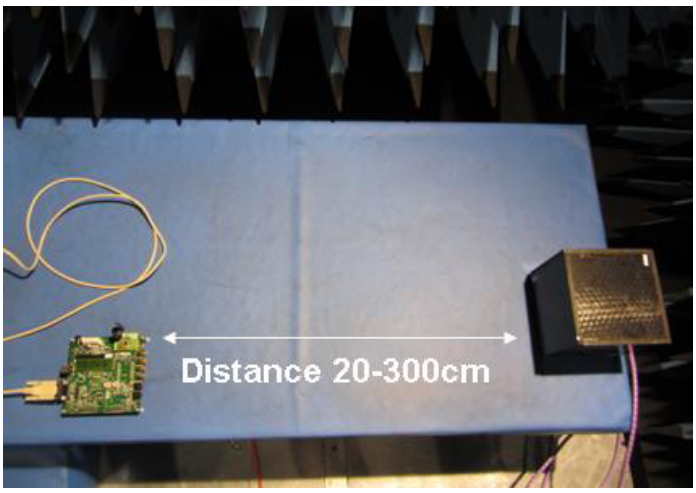

Figure 8.5: *Measurement set up in anechoic chamber.*

The antenna of the independent module is placed at the centre of the box. The shielding performances of the box have been measured for two orientations, see Figure 8.6, respectively with one face placed perpendicularly to line formed between the two module, or rotated of 45° to place an edge of the box between the two module. Because the edges are potential source of leakage, measurement with and without metallic tape on the edge have been realized.

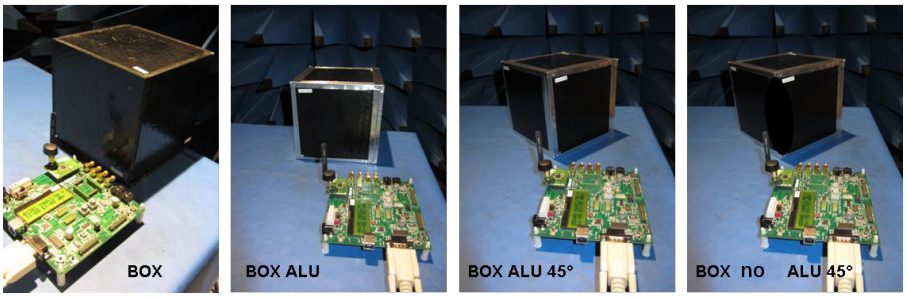

Figure 8.6: *Configurations of the box for the measurement of the shielding effectiveness.*

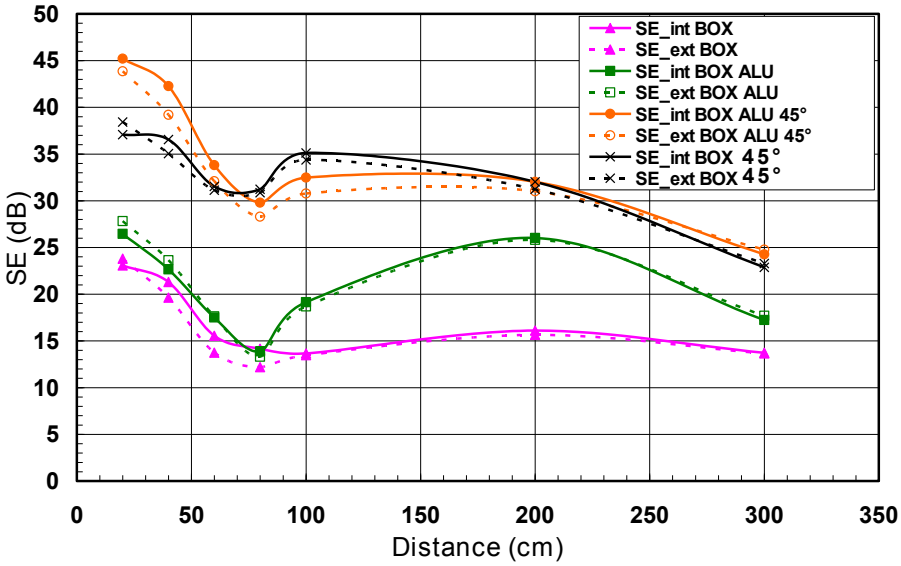

Figure 8.7: *SE for the different configurations of Figure 8.4 as function of the transmitter-receiver distance.*

Figure 8.7 shows the shielding effectiveness for the different configurations of Figure 8.6 as function of the transmitter-receiver distance. SE is defined as the ratio of power transmitted between the two modules, respectively measured in absence or in presence of the box. As each module can be used either as the transmitter or the receiver, the shield-

ing effectiveness with the receiver inside the box is called SE_{int} and SE_{ext} when outside.

The first general observation is that SE_{int} and SE_{ext} are close to each other. The second observation is that for each measurement configuration, the SE behave differently above or below a distance of 70 cm which corresponds to the wavelength. This behaviour might come from the near-field and far-field limit. The distance of Fraunhofer is equal to 20 cm in this case. The first measurement points are maybe subject to near-field interferences.

In the far field region, the SE of the box without tape is around 15 dB. The tape increases the SE. This reveals some leakage at the edges. The analytical model predicts a SE situated around 30 dB for the hybrid which is 10 dB above the measurements. The reason remains unexplained at the moment.

The SE of the edge of the box (45° orientation) is higher than the SE of the face no matter if there is a metallic tape. The better SE of the edge is confirmed by FEM and is presented in Figure 8.8. The angle of incidence of the antenna radiation incoming at the edge of the box, is greater than at the panel centre, resulting in a higher internal reflection in this region. The high reflection prevents the transmission of the radiation outside de box.

8.2.2 Stealth wind turbine

A small wind turbine dedicated to supply electricity of pleasure boat has been selected in order to test the stealth potential of the hybrid material. The turbine model is the *Rutland 913*. The blade and the housing of the turbine are made of polymer so in order to increase the detectability, metallic plates have been placed on the wing and nose of the turbine, Figure 8.9(a). The hybrid placed on the metallic plate to stealth the wind turbine is made of honeycomb with 6 mm cell size filled with polycarbonate reinforced with 1wt% of CNT foamed to a density equal to $0.55\,\mathrm{g{\cdot}cm^{-3}}$, Figure 8.9(b). Horn antenna has been used to emit the signal.

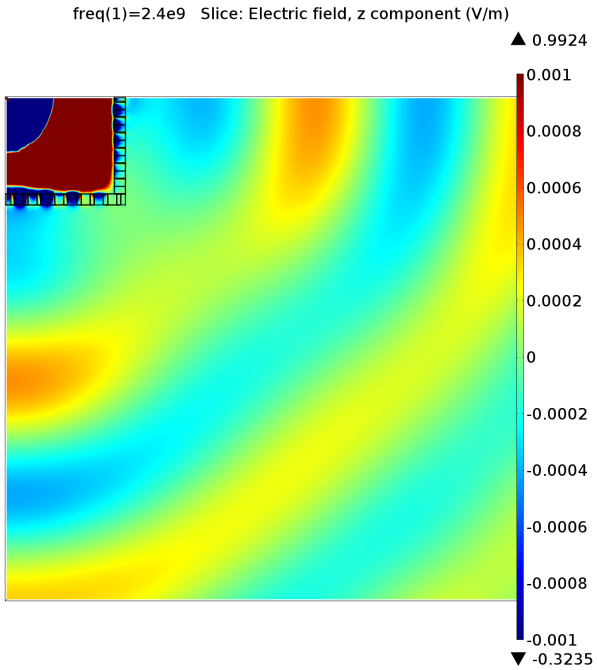

Figure 8.8: *3D FE simulation of the box with an edge antenna at its centre. Cartography of electric field intensity at 2.4 GHz in the plane normal to the antenna.*

Reflectivity measurements of the metallized wind turbine, stealth wind turbine and background in the 8-12 GHz and 18-26 GHz frequencies band is shown in Figure 8.10(a) and (b), respectively. Thanks to the hybrid, the reflectivity of the wind turbine is 4 to 5 dB lower in the 8-12 GHz band. This corresponds to an absorption of roughly 50% at 8 GHz to 70% at 12 GHz. The absorption level correspond to the measurements performed with the modified Line-Line method of this hybrid configuration (see figure4.18). In the 18-26 GHz frequencies band, the background reflectivity is abnormally high in between 20 and 23 GHz so that there is no more distinction with the metallized wind turbine reflectivity. But outside the problematic band, the stealth wind turbine is almost undetectable with an absorption level of $\approx$ 85% which is again close to the measurement performed with the modified Line-Line method.

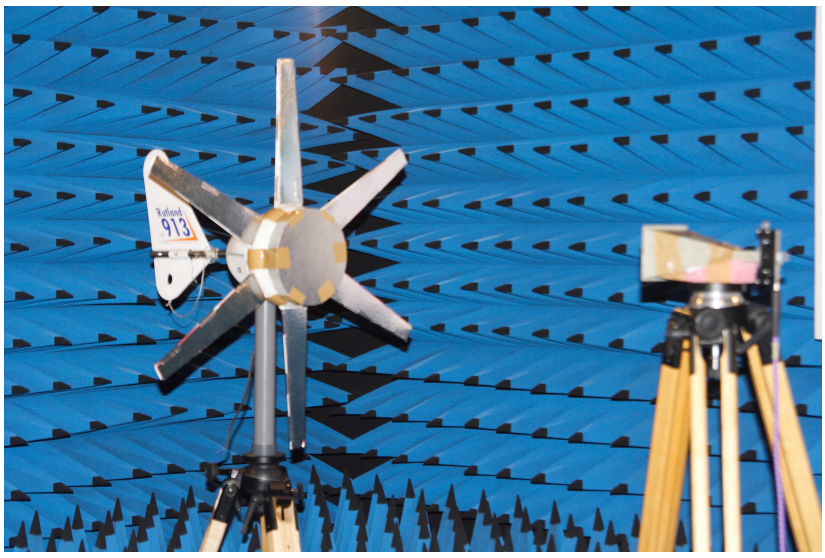

(a) Metallized wind turbine.

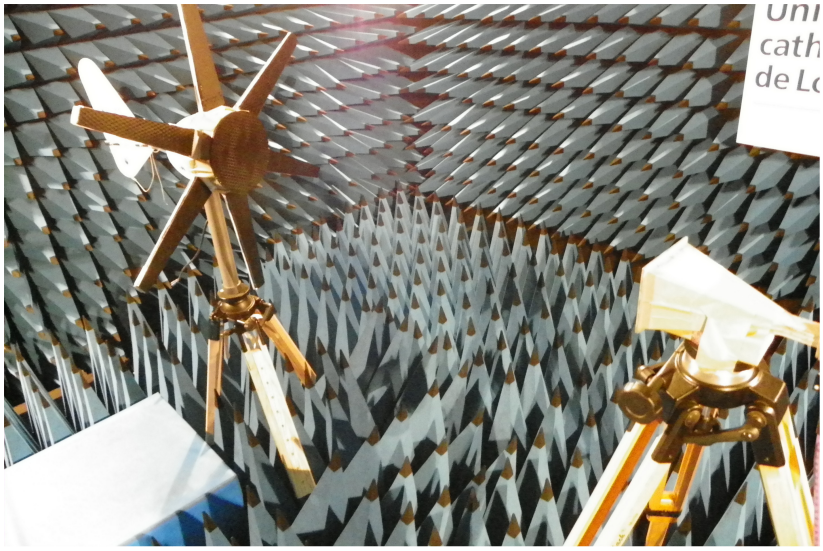

(b) Stealth wind turbine.

Figure 8.9: *Set-up measurement of a metallized (a) and stealth (b) wind turbine in an anechoic chamber*

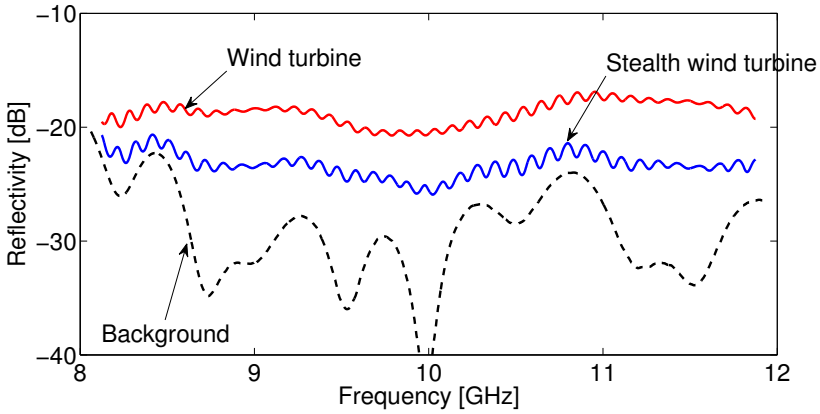

(a) 8-12 GHz frequencies band.

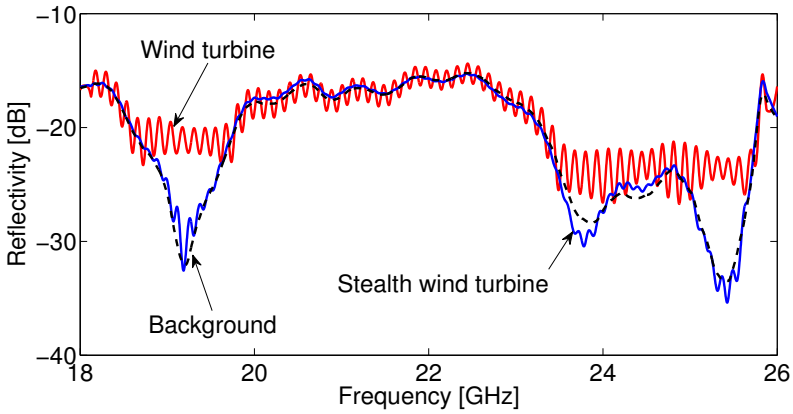

(b) 18-26 GHz frequencies band.

Figure 8.10: *Reflectivity measurements of the metallized wind turbine (red line), stealth wind turbine (blue line) and background (dashed black line). The distance between the antenna and the turbine is equal to 1.2 m for both measurements.*

8.3 Conclusion

Several fields of applications exist for the multifunctional material thanks to its unique set of properties. The most promising applications are those combining harsh environment and/or structural function with far-field EM absorption over a wideband of frequencies comprised between 5 and 40 GHz. The WiFi shielding box has shown that shielding below the cutoff of near-field radiation is not as high than expected. The free space measurements performed inside the anechoic chamber on the hybrid agree with the measurements performed with the modified Line-Line method.

Chapter 9

Conclusion

A new class of multifunctional hybrid materials has been developed based on a multiscale architectured material approach towards combined optimization of mechanical and electromagnetic (EM) absorption performances. The material consists of a sandwich panel made of EM transparent face sheets and an hybrid core made of honeycomb filled with a carbon nanotube reinforced polymer foam.

Many aspects of hybrid materials engineering have been covered in the course of this thesis.

In Chapter 3, several processing routes have been followed to manufacture the foam filled honeycomb. It turns out that processing defects do not severely degrade the EM absorption capabilities of the hybrid. The choice of the processing route has thus to be made as a function of the application and of the upscaling characteristics. The easiest processing route is the *in-situ* foaming with a chemical foaming agent method because the finishing of the panel is excellent and the operation can be achieved in a single step. But, in order to produce large panels with a semi-continuous process, the mechanical insertion of foamed nanocomposite with scCO_2 could be more suitable. In term of material quality, scCO_2 foaming gives a finer microstructure and a more efficient carbon nanotube network than chemical foaming.

In Chapter 4, we have shown that the foam filled honeycomb cells act

like waveguides by influencing the real part of the effective permittivity. This creates a cutoff frequency below which the reflection of the hybrid is increased and above which the impedance matching of the hybrid with respect to air is improved, reducing therefore the reflection. The addition of EM transparent sheets, for the sandwich structure, leads to a reduction of the mismatch between the hybrid and air but only in a specific range of frequencies. An analytical model has been developed to predict the level of absorption of an hybrid slab or of a sandwich panel with an hybrid core.

A proof of concept to extend the absorption below the cutoff of the hybrid has been presented in Chapter 5. The sub cutoff absorption is created thanks to left handed propagation inside the hybrid. The left handed propagation has been made possible by placing one split ring resonator in each cell of the honeycomb. But split ring resonators are sensitive to the polarization of the incident EM radiation and due to the resonance nature of split ring resonator, the left-handed propagation is narrowband. Using different sizes of split ring resonators can however enlarge the bandwidth.

The mechanical tests conducted in Chapter 6 have shown that the hybrid has several advantages over a simple foam system. The bending and shear modulus is increased owing to the presence of the honeycomb. In case of crushing, the honeycomb has a positive role. The presence of the honeycomb increases the energy needed to crush the core, and the presence of the foam leads to a small wavelength buckling mode in the honeycomb wall (compared to a honeycomb without foam), by increasing even more the energy needed to crush the core. When hybrid panels are impacted, the honeycomb segments the panel and prevents the propagation of long cracks. Compared to sandwich with foam core, the hybrid core prevents the cracking of the back face, by dissipating the energy through core crushing and through back face debonding.

The parametric study performed in chapter 7 has highlighted that, in order to minimize the mass of the panel for EM absorption, the best solution is to avoid non-absorbing elements like faces sheets and honeycomb. On the contrary, the best solution for the stiffness involves the presence of the face sheet and honeycomb. Compared to a slab of

foam, the sandwich structure with an hybrid core presents a high level of absorption over narrower band of frequency. In chapter 7, a tool has also been developed in order to support the choice of the sandwich configuration as a function of the application constraints.

In chapter 8, some fields of application needing the specific set of properties of the hybrid have been presented. The most promising applications are those combining harsh environment and/or structural function with far-field EM absorption over a wideband of frequencies comprised between 5 and 40 GHz. The free space measurements performed inside the anechoic chamber on the hybrid agree with the measurements performed with the modified Line-Line method.

Nevertheless some limitations and challenges remain before a potential industrialisation of the hybrid material can be expected.

Some process limitations are still needed to be solved. As shown in Chapter 7, applications may require a thick hybrid cores in order to fulfil the stiffness constraint. Foaming thick plate is not a straightforward process. Also, the size of the hot-press, for chemical foaming, or the size of the reactor, for the supercritical CO_2 foaming, defines the size of the hybrid panel that can be produced. High internal phase emulsion constitute an suitable process approach to overcome these two limitations.

In order to further increase the ratio of the bending stiffness over the weight of sandwich panels, lower foam densities must be selected, as explained in Chapter 7. Lowering the density leads a drop of the dielectric constant and the conductivity if the same nanocomposite foam is used. In order to keep the conductivity at efficient values, more carbon nanotubes have to be dispersed into the matrix, arising several processing issues. During foaming, the viscosity of the nanocomposite is a key parameter to control in order to achieve low densities. If it is too low, the foam collapses or if it is too high, foam expansion is limited. When the foaming is triggered with a chemical foaming agent, expansion of the foam occurs in melt phase. The viscosity of the melt is related to the carbon nanotubes content and increases with the latter [39]. Our tests have shown that 1.5wt% of carbon nanotubes into a polycarbonate hosting matrix is already a limit to trigger the chemical foaming. When

foaming is triggered with scCO_2 , Monnereau [39] has shown that high crystallinity in polycarbonate limits the foam expansion. Unfortunately, crystallinity is induced by supercritical CO_2 , and this behaviour is amplified by the presence of carbon nanotubes that act as nucleating agents for crystals birth. Vacuum assisted foaming might be a solution to deal the high viscosity of the nanocomposite.

A model predicting the EM properties of the foam as a function of the carbon nanotubes content, the hosting matrix, and the foam density will be an usefull tool in order to further optimize the hybrid system.

Failure strength and impact resistance also need to be integrated to the design tool. In order to obtain accurate prediction of the impact resistance, the visco-elastic-visco-plastic properties of the foam and face sheets have to be incorporated to the finite element model. Nevertheless, an analytical model of the elastic properties of the hybrid reduces the time and computer resources for early design step.

A major concern regarding the strength and impact performances of the hybrid is the low adherence between the foam and the honeycomb walls. An improvement of the cohesion can be achieved using several strategies. The surface of the honeycomb can be treated in order to increase the adhesion with the foam. Other polymer matrix can be used. Or the honeycomb walls can be perforated to allow foam junction. Holes smaller than the operating wavelength should not impact the EM behaviour but may localize mechanical stress when crushed.

Concerning EM performances, ferromagnetic nanoparticules showing negative permeability around the ferromagnetic resonance could be used instead of split ring resonators to achieve left-handed propagation. Such particles can be integrated in the processing of the hybrid during the dispersion step of the CNT into the hosting matrix.

Finally, the absorption of the hybrid can be improved by structuring the surface. Depending of the target frequency, the process defects have shown that a layer of foam outside the honeycomb or an array of hemispheric foam cell improved the efficiency (see Figure 3.8). This array may be very effective to absorb radiations coming from different incidence angles if the sphere diameter matches the wavelength.

Appendix A

Thermal degradation of foam during mechanical insertion

During the mechanical insertion of the foam inside the honeycomb both the expansion of the foam cells and the formation of solid layer occur. An example of a combination of both mechanisms described above is shown in Figure A.1, where, in the same cell near the wall, a solid thick layer and an increase of the pore diameter are present. A thick layer forms where the foam is in contact with the wall, and the coalescence occurs if there is a space, Figure A.2(b). Indeed, when the foam is inserted, it does not lay flat on the honeycomb but it is curved, see Figure A.2(a). The curved shape is either due to deformation during foaming or due to heat coming from the heating plate which allows the foam plate to creep.

A proper selection of the temperature and speed of insertion avoids any gap between the foam and the cell, and the degradation of the foam can be reduced.

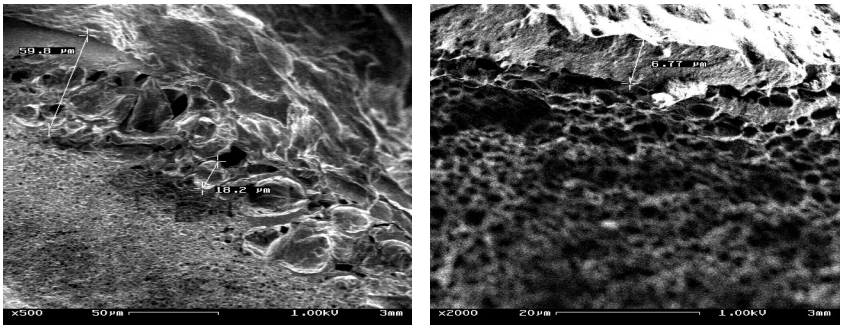

(a) (b)

Figure A.1: *Sem micrography near the honeycomb cell wall of CO_2 foam inserted at 150°C and 10 mm·min^{-1}*

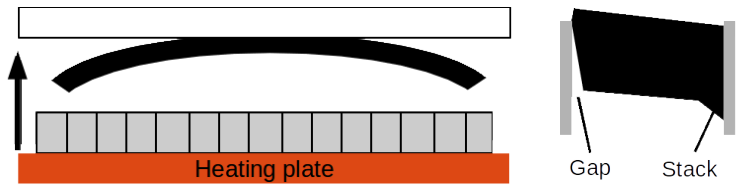

(a) Schematic view of the curvature of the foam before the insertion

(b) Zoom on the gap between the wall and foam and the stacking

Figure A.2: *Schematic view of the insertion step*

Appendix B

List of references

Journal papers

1. Molenberg I., Bernal M. M., **Bollen P.**, Spote D., Verdejo R., Pardoen T., Bailly C., Huynen I., *Simple, convenient, and nondestructive electromagnetic characterization technique for composite and multiscale hybrid samples at microwave frequencies.* In: Microwave & Optical Technology Letters, Vol. 56, no.2, p. 504-509 (February 2014).

2. **Bollen P.**, Quiévy N., Huynen I., Bailly C., Detrembleur C., Thomassin J.-M., Pardoen T., *Multifunctional architectured materials for electromagnetic absorption.* In: Scripta Materialia, Vol. 68, no.1, p. 50-54 (janvier 2013).

3. Quiévy N., **Bollen P.**, Thomassin J.-M., Detrembleur C., Pardoen T., Bailly C., Huynen I., *Electromagnetic absorption properties of carbon nanotube nanocomposite foam filling honeycomb waveguide structures.* In: IEEE Transactions on Electromagnetic Compatibility (special issue on Nanotechnology), Vol. 54, no. 1, p. 47-53 (February 2012).

4. Huynen I., Quiévy N., Bailly C., **Bollen P.**, Detrembleur C., Eggermont S., Molenberg I., Thomassin J.-M., Urbanczyk L., Par-

doen T., *Multifunctional hybrids for electromagnetic absorption.* In: Acta Materialia, Vol. 59, no. 8, p. 3255-3266 (May 2011).

Oral communications

1. **Bollen P.**, Quiévy N., Bailly C., Huynen I., Pardoen T., *Multifunctional sandwich structure for electromagnetic absorption and mechanical performances. 16th European Conference on Composite Materials (ECCM16) (Sevilla, Spain, du 22/06/2014 au 26/06/2014).* In: Proceedings of the 16th European Conference on Composite Materials (ECCM16). (2014).

2. **Bollen P.**, Pardoen T., Bailly C., Huynen I., *Multifunctional Metamaterial Absorber Based on Honeycomb Filled with Epoxy-Carbon Nanotube Nanocomposite and Split Ring Resonator.* 7th International Congress on Advanced Electromagnetic Materials in Microwaves and Optics - Metamaterials 2013 (Bordeaux, France, du 16/09/2013 au 21/09/2013), p. 4 p.

3. **P. Bollen**, Quievy N., Huynen I., Bailly C., Detrembleur C., Thomassin J.-M., Pardoen T., *Hybrid and Hierarchical Composite Materials* , TMS 2013 Annual Meeting and Exhibition (San Antonio, Texas, USA, 03/03/2013 au 07/03/2013).

4. **Bollen P.**, Quiévy N., Detrembleur C., Thomassin J.-M., Bailly C., Pardoen T., Huynen I., *Electromagnetic absorption of sandwich panel made of glass fiber reinforced polymer and nanocomposite foam filled honeycomb.* EMC Europe 2012 Conference September 17-21, 2012, paper D6.1 (6 pages) (Roma, Italy, du 17/09/2012 au 21/09/2012). In: Proceedings of the EMC Europe 2012 Conference. p. paper D6.1 (6 pages).

5. Huynen I., Quiévy N., **Bollen P.**, Danlée Y., Bailly C., Pardoen T., *Multi-hierarchical metamaterials combining conductive inclusions and polymer matrices for Electromagnetic Interference Shielding.* META 2012 Conference (Paris, France, du 19/04/2012 au 22/04/2012). p. 3 p.

6. Monnereau L., Thomassin J.-M., Quiévy N., **Bollen P.**, Eggermont S., Pardoen T., Bailly C., Huynen I., Jérôme C., Detrembleur C., *Foaming in CO2sc medium as an efficient way to produce Electromagnetic Interference Shielding Materials.* European Polymer Congress EPF 2011 (Grenada, Espagne, du 26/06/2011 au 01/07/2011). p. 1 p.

7. Eggermont S., **Bollen P.**, Quiévy N., Bailly C., Detrembleur C., Molenberg I., Thomassin J.-M., Monnereau L., Urbanczyk L., Pardoen T., Huynen I.,*Novel frequency selective electromagnetic absorber combining honeycomb waveguide and carbon nanotube composites.* European Conference on Antennas and Propagation (Rome, du 11/04/2011 au 15/04/2011). In: Proceedings of the European Conference on Antennas and Propagation: Rome, 2011, 2335-2338.

8. Quiévy N., Huynen I., Bailly C., Detrembleur C., Eggermont S., **Bollen P.**, Molenberg I., Thomassin J.-M., Monnerau L., Urbanczyk L., Pardoen T., *Multifunctional Hybrids for Electromagnetic Absorption.* 2nd Int. Conference on Multifunctional, Hybrid and Nanomaterials (Strasbourg, France, du 06/03/2011 au 10/03/2011). In: Book of abstracts, 2011.

Bibliography

[1] A Saib, L. Bednarz, R. Daussin, C. Bailly, Xudong Lou, J. Thomassin, C. Pagnoulle, C. Detrembleur, R. Jérôme, and I Huynen. Carbon nanotube composites for broadband microwave absorbing materials. *Microwave Theory and Techniques, IEEE Transactions on*, 54(6):2745–2754, June 2006.

[2] A. Alavi Nia and M.Z. Sadeghi. The effects of foam filling on compressive response of hexagonal cell aluminum honeycombs under axial loading experimental study. *Materials and Design*, 31(3):1216 – 1230, 2010.

[3] M.F. Ashby. *Materials selection in mechanical design*. Elsevier Butterworth Heinemann, 2005.

[4] Lorna J Gibson and Michael F Ashby. *Cellular solids: structure and properties*. Cambridge university press, 1999.

[5] Lorna J Gibson. Biomechanics of cellular solids. *Journal of biomechanics*, 38(3):377–399, 2005.

[6] DH Chen. Bending deformation of honeycomb consisting of regular hexagonal cells. *Composite structures*, 93(2):736–746, 2011.

[7] D. Zenkert and Nordic Industrial Fund. *The handbook of sandwich construction*. North European Engineering and Science Conference series. Engineering Materials Advisory Services, 1997.

[8] Laurent Laszczyk. *Homogénéisation et optimisation topologique de panneaux architecturés*. PhD thesis, Université de Grenoble, 2011.

[9] S. J. Orfanidis. Electromagnetic waves and antennas, 2010.

[10] D.M. Pozar. *Microwave Engineering, 4th Edition.* Wiley Global Education, 2011.

[11] Ari H Sihvola. *Electromagnetic mixing formulas and applications.* Number 47 in Electromagnetic waves. Institution of Electrical Engineers, 1999.

[12] Xingcun Colin Tong. *Advanced materials and design for electromagnetic interference shielding.* CRC Press, 2008.

[13] Paul Saville. Review of radar absorbing materials. Technical report, DTIC Document, 2005.

[14] William B. Weir. Automatic measurement of complex dielectric constant and permeability at microwave frequencies. *Proceedings of the IEEE*, 62(1):33–36, Jan 1974.

[15] Won-Ho Choi, Jin-Bong Kim, Jae-Hwan Shin, Tae-Hoon Song, Won-Jun Lee, Young-Sik Joo, and Chun-Gon Kim. Circuit-analog (ca) type of radar absorbing composite leading-edge for wing-shaped structure in x-band: Practical approach from design to fabrication. *Composites Science and Technology*, 2014.

[16] LiangKui Sun, HaiFeng Cheng, YongJiang Zhou, and Jun Wang. Broadband metamaterial absorber based on coupling resistive frequency selective surface. *Opt. Express*, 20(4):4675–4680, Feb 2012.

[17] Jeffrey A Reed. *Dissertation proposal: Frequency selective surfaces with multiple periodic elements.* PhD thesis, University of Texas at Dallas, 1997.

[18] Yann Danlée, Christian Bailly, and Isabelle Huynen. Thin and flexible multilayer polymer composite structures for effective control of microwave electromagnetic absorption. *Composites Science and Technology*, 100:182–188, 2014.

[19] HL Fan, Wei Yang, and ZM Chao. Microwave absorbing composite lattice grids. *Composites Science and Technology*, 67(15):3472–3479, 2007.

[20] Ehsan Bafekrpour, Andrey Molotnikov, James C Weaver, Yves Bréchet, and Yuri Estrin. Responsive materials: A novel design for enhanced machine-augmented composites. *Scientific reports*, 4, 2014.

[21] O. Bouaziz, Y. Bréchet, and J. D. Embury. Heterogeneous and architectured materials: A possible strategy for design of structural materials. *Advanced Engineering Materials*, 10(1-2):24–36, 2008.

[22] Jean-Michel Thomassin, Christine Jérôme, Thomas Pardoen, Christian Bailly, Isabelle Huynen, and Christophe Detrembleur. Polymer/carbon based composites as electromagnetic interference (emi) shielding materials. *Materials Science and Engineering: R: Reports*, 74(7):211 – 232, 2013.

[23] I. Huynen, N. Quiévy, C. Bailly, P. Bollen, C. Detrembleur, S. Eggermont, I. Molenberg, J.M. Thomassin, L. Urbanczyk, and T. Pardoen. Multifunctional hybrids for electromagnetic absorption. *Acta Materialia*, 2011.

[24] P Bollen, N Quievy, C Detrembleur, JM Thomassin, C Bailly, T Pardoen, and I Huynen. Electromagnetic absorption of sandwich panel made of glass fiber reinforced polymer and nanocomposite foam filled honeycomb. In *Electromagnetic Compatibility (EMC EUROPE), 2012 International Symposium on*, pages 1–6. IEEE, 2012.

[25] Wolfgang Bauhofer and Josef Z. Kovacs. A review and analysis of electrical percolation in carbon nanotube polymer composites. *Composites Science and Technology*, 69(10):1486 – 1498, 2009. CNT-NET 07 Special Issue with regular papers.

[26] Sven Pegel, Petra Potschke, Gudrun Petzold, Ingo Alig, Sergej M. Dudkin, and Dirk Lellinger. Dispersion, agglomeration, and net-

work formation of multiwalled carbon nanotubes in polycarbonate melts. *Polymer*, 49(4):974 – 984, 2008.

[27] Petra Potschke, Arup R Bhattacharyya, and Andreas Janke. Melt mixing of polycarbonate with multiwalled carbon nanotubes: microscopic studies on the state of dispersion. *European Polymer Journal*, 40(1):137 – 148, 2004.

[28] Rui Zhang, Alice Dowden, Hua Deng, Mark Baxendale, and Ton Peijs. Conductive network formation in the melt of carbon nanotube/thermoplastic polyurethane composite. *Composites Science and Technology*, 69(10):1499 – 1504, 2009. CNT-NET 07 Special Issue with regular papers.

[29] Mercedes Fernandez, Maite Landa, Maria Eugenia Munoz, and Anton Santamaria. Electrical conductivity of pur/mwcnt nanocomposites in the molten state, during crystallization and in the solid state. *European Polymer Journal*, 47(11):2078 – 2086, 2011.

[30] Superb K. Misra, Tahera I. Ansari, Sabeel P. Valappil, Dirk Mohn, Sheryl E. Philip, Wendelin J. Stark, Ipsita Roy, Jonathan C. Knowles, Vehid Salih, and Aldo R. Boccaccini. Poly(3-hydroxybutyrate) multifunctional composite scaffolds for tissue engineering applications. *Biomaterials*, 31(10):2806 – 2815, 2010.

[31] Gavin Jell, Raquel Verdejo, Laleh Safinia, Milo S. P. Shaffer, Molly M. Stevens, and Alexander Bismarck. Carbon nanotube-enhanced polyurethane scaffolds fabricated by thermally induced phase separation. *J. Mater. Chem.*, 18:1865–1872, 2008.

[32] Marie Claire Hermant, Maarten Verhulst, Andriy V. Kyrylyuk, Bert Klumperman, and Cor E. Koning. The incorporation of single walled carbon nanotubes into polymerized high internal phase emulsions to create conductive foams with a low percolation threshold. *Composites Science and Technology*, 69(5):656 – 662, 2009.

[33] M.Mar Bernal, Isabel Molenberg, Sergio Estravis, MiguelAngel Rodriguez-Perez, Isabelle Huynen, MiguelAngel Lopez-Manchado,

and Raquel Verdejo. Comparing the effect of carbon-based nanofillers on the physical properties of flexible polyurethane foams. *Journal of Materials Science*, 47(15):5673–5679, 2012.

[34] Rhomie L. Heck. A review of commercially used chemical foaming agents for thermoplastic foams. *Journal of Vinyl and Additive Technology*, 4(2):113–116, 1998.

[35] Lin Yang, Hualin Fan, Jun Liu, Yao Ma, and Qing Zheng. Hybrid lattice-core sandwich composites designed for microwave absorption. *Materials and Design*, 50(0):863 – 871, 2013.

[36] U. K. Vaidya, C. Ulven, S. Pillay, and H. Ricks. Impact damage of partially foam-filled co injected honeycomb core sandwich composites. *Journal of Composite Materials*, 37(7):611–626, 2003.

[37] Y.S. Wang, F. Lee, C.C. Kuo, and K. Baron. Open-ended cells filled with polycyanurate foam; compressive strength, August 16 1994. US Patent 5,338,594.

[38] J.E. Campbell, F. Forte, G.D. Hibbard, and H.E. Naguib. Periodic cellular metal/polyurethane foam hybrid materials. *Journal of Composite Materials*, 43(3):207–216, 2009.

[39] Laure Monnereau, Laetitia Urbanczyk, Jean-Michel Thomassin, Michael Alexandre, Christine Jérôme, Isabelle Huynen, Christian Bailly, and Christophe Detrembleur. Supercritical {CO2} and polycarbonate based nanocomposites: A critical issue for foaming. *Polymer*, 55(10):2422 – 2431, 2014.

[40] Jean-Michel Thomassin, Christophe Pagnoulle, Lukasz Bednarz, Isabelle Huynen, Robert Jérôme, and Christophe Detrembleur. Foams of polycaprolactone/mwnt nanocomposites for efficient emi reduction. *J. Mater. Chem.*, 18:–, 2008.

[41] N. Quiévy, P. Bollen, J.M. Thomassin, C. Detrembleur, T. Pardoen, C. Bailly, and I. Huynen. Electromagnetic absorption properties of carbon nanotube nanocomposite foam filling honeycomb waveguide

structures. *IEEE Transactions on Electromagnetic Compatibility (special issue on Nanotechnology)*, pages February–2012, 2012.

[42] Isabel Molenberg, Isabelle Huynen, Anne-Christine Baudouin, Christian Bailly, Jean-Michel Thomassin, Christophe Detrembleur, et al. Foamed nanocomposites for emi shielding applications. *Advanced Microwave and Millimeter Wave Technologies: Semiconductor Devices, Circuits and Systems*, pages 453–470, 2010.

[43] R. F. Harrington. *Time-Harmonic Electromagnetic Fields*. Ed. McGraw-Hill Book Company, 1961.

[44] Isabel Molenberg, Maria M Bernal, Pierre Bollen, David Spote, Raquel Verdejo, Thomas Pardoen, Christian Bailly, and Isabelle Huynen. Simple, convenient, and nondestructive electromagnetic characterization technique for composite and multiscale hybrid samples at microwave frequencies. *Microwave and Optical Technology Letters*, 56(2):504–509, 2014.

[45] Davide Micheli, Carmelo Apollo, Roberto Pastore, Ramon Bueno Morles, Mario Marchetti, and Gabriele Gradoni. Electromagnetic characterization of composite materials and microwave absorbing modeling. *Advances in Nanocomposites-Synthesis, Characterization and Industrial Applications, edited by B. Reddy*, 2011.

[46] Isabelle Huynen, Catherine Steukers, and Fabienne Duhamel. A wideband line-line dielectrometric method for liquids, soils, and planar substrates. *Instrumentation and Measurement, IEEE Transactions on*, 50(5):1343–1348, 2001.

[47] Michael D Janezic and Jeffrey A Jargon. Complex permittivity determination from propagation constant measurements. *IEEE Microwave and Guided Wave Letters*, 9(2):76–78, 1999.

[48] G Gradoni, D Micheli, V Mariani Primiani, F Moglie, and M Marchetti. Determination of the electrical conductivity of carbon/carbon at high microwave frequencies. *Carbon*, 54:76–85, 2013.

[49] AM Nicolson and GF Ross. Measurement of the intrinsic properties of materials by time-domain techniques. *Instrumentation and Measurement, IEEE Transactions on*, 19(4):377–382, 1970.

[50] DDL Chung. Electromagnetic interference shielding effectiveness of carbon materials. *carbon*, 39(2):279–285, 2001.

[51] James Baker-Jarvis, Eric J Vanzura, and William A Kissick. Improved technique for determining complex permittivity with the transmission/reflection method. *Microwave Theory and Techniques, IEEE Transactions on*, 38(8):1096–1103, 1990.

[52] Jae-Hwang Lee, Jonathan P Singer, and Edwin L Thomas. Micro-/nanostructured mechanical metamaterials. *Advanced Materials*, 24(36):4782–4810, 2012.

[53] Jesse L. Silverberg, Arthur A. Evans, Lauren McLeod, Ryan C. Hayward, Thomas Hull, Christian D. Santangelo, and Itai Cohen. Using origami design principles to fold reprogrammable mechanical metamaterials. *Science*, 345(6197):647–650, 2014.

[54] Sahab Babaee, Jongmin Shim, James C Weaver, Elizabeth R Chen, Nikita Patel, and Katia Bertoldi. 3d soft metamaterials with negative poisson's ratio. *Advanced Materials*, 25(36):5044–5049, 2013.

[55] Sébastien Guenneau, Alexander Movchan, Gunnar Pétursson, and S Anantha Ramakrishna. Acoustic metamaterials for sound focusing and confinement. *New Journal of physics*, 9(11):399, 2007.

[56] DR Smith, JB Pendry, and MCK Wiltshire. Metamaterials and negative refractive index. *Science*, 305(5685):788–792, 2004.

[57] DR Smith, S Schultz, P Markoš, and CM Soukoulis. Determination of effective permittivity and permeability of metamaterials from reflection and transmission coefficients. *Physical Review B*, 65(19):195104, 2002.

[58] Alexandre Sellier, Tatiana V Teperik, Shah Nawaz Burokur, Guy Sabanowski, Gérard-Pascal Piau, and André de Lustrac. Design

and model of wideband absorber made of ultrathin metamaterial structures. *Applied Physics A*, 117(2):739–746, 2014.

[59] Silvio Hrabar, Juraj Bartolic, and Zvonimir Sipus. Waveguide miniaturization using uniaxial negative permeability metamaterial. *Antennas and Propagation, IEEE Transactions on*, 53(1):110–119, 2005.

[60] Koray Aydin, Kaan Guven, Costas M Soukoulis, and Ekmel Ozbay. Observation of negative refraction and negative phase velocity in left-handed metamaterials. *Applied Physics Letters*, 86(12):124102, 2005.

[61] Chiharu Mitsumata and Satoshi Tomita. Negative permeability of magnetic nanocomposite films for designing left-handed metamaterials. *Applied Physics Letters*, 91(22):223104, 2007.

[62] S. Chui and Liangbin Hu. Theoretical investigation on the possibility of preparing left-handed materials in metallic magnetic granular composites. *Phys. Rev. B*, 65:144407, Mar 2002.

[63] M. Zarei Mahmoudabadi and M. Sadighi. A study on the static and dynamic loading of the foam filled metal hexagonal honeycomb : Theoretical and experimental. *Materials Science and Engineering: A*, 530(0):333 – 343, 2011.

[64] Instron, impact testing. `http://www.instron.us/wa/applications/test_types/impact/default.aspx`. Accessed: 2014-12-17.

[65] Martin Gagné and Daniel Therriault. Lightning strike protection of composites. *Progress in Aerospace Sciences*, 64:1–16, 2014.

[66] Bill Marker. Use of radar-absorbing material to resolve us navy electromagnetic interference problems. *Challenges & Solutions for the 21st Century*, page 56, 2014.